

Research

---

**DECOVALEX III PROJECT**

**Thermal-Hydrological Modeling of the  
Yucca Mountain Project Drift Scale Test**

Task 2A Final Report

Compiled by:  
Robin N. Datta

February 2005

With contributions from:

Sebastia Olivella  
Claudia Gonzalez  
Antonio Gens  
Miguel Luna  
Ronald T. Green  
Scott L. Painter



## Research

---

# DECOVALEX III PROJECT

## Thermal-Hydrological Modeling of the Yucca Mountain Project Drift Scale Test

Task 2A Final Report

Compiled by:  
Robin N. Datta

Bechtel SAIC Company, Las Vegas, USA

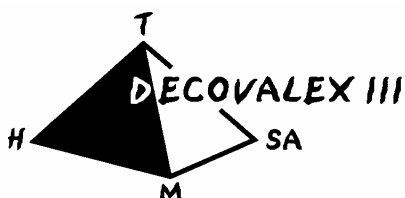
February 2005

With contributions from:

Sebastia Olivella<sup>1</sup>  
Claudia Gonzalez<sup>1</sup>  
Antonio Gens<sup>1</sup>  
Miguel Luna<sup>1</sup>  
Ronald T. Green<sup>2</sup>  
Scott L. Painter<sup>2</sup>

<sup>1</sup>University Polytechnique of Catalina, Spain

<sup>2</sup>Southwest Research Institute, San Antonio, Texas, USA



**SKi**

This report concerns a study which has been conducted for the DECOVALEX III Project. The conclusions and viewpoints presented in the report are those of the author/authors and do not necessarily coincide with those of the SKI.

## Foreword

DECOVALEX is an international consortium of governmental agencies associated with the disposal of high-level nuclear waste in a number of countries. The consortium's mission is the DEvelopment of COupled models and their VALidation against EXperiments. Hence the acronym/name DECOVALEX. Currently, agencies from Canada, Finland, France, Germany, Japan, Spain, Switzerland, Sweden, United Kingdom, and the United States are in DECOVALEX. Emplacement of nuclear waste in a repository in geologic media causes a number of physical processes to be intensified in the surrounding rock mass due to the decay heat from the waste. The four main processes of concern are thermal, hydrological, mechanical and chemical. Interactions or coupling between these heat-driven processes must be taken into account in modeling the performance of the repository for such modeling to be meaningful and reliable.

The first DECOVALEX project, begun in 1992 and completed in 1996 was aimed at modeling benchmark problems and validation by laboratory experiments. DECOVALEX II, started in 1996, built on the experience gained in DECOVALEX I by modeling larger tests conducted in the field. DECOVALEX III, started in 1999 following the completion of DECOVALEX II, is organized around four tasks. The FEBEX (Full-scale Engineered Barriers EXperiment) in situ experiment being conducted at the Grimsel site in Switzerland is to be simulated and analyzed in Task 1. Task 2, centered around the Drift Scale Test (DST) at Yucca Mountain in Nevada, USA, has several sub-tasks (Task 2A, Task 2B, Task 2C and Task 2D) to investigate a number of the coupled processes in the DST. Task 3 studies three benchmark problems: a) the effects of thermal-hydrologic-mechanical (THM) coupling on the performance of the near-field of a nuclear waste repository; b) the effect of upscaling THM processes on the results of performance assessment; and c) the effect of glaciation on rock mass behavior. Task 4 is on the direct application of THM coupled process modeling in the performance assessment of nuclear waste repositories in geologic media.

Task 2A of DECOVALEX III entails modeling the thermal-hydrologic (TH) response of the DST during the heating and cooling phases of the test to predict the temperature distributions and the movement of rock moisture in the test block at various times. The predictions are subsequently compared with the measurements of temperatures and saturation and are analyzed. The insights/understandings gained allow refinements/adjustments to be made to the conceptual model. This process is expected to eventually result in the development of a robust, validated TH model, which can be the basis for assessing the performance of a repository.

This Task 2A Final Report largely subsumes the Interim Report of February 2002 as well as documents the modeling and comparative analyses done by the research teams subsequently.

Lanru Jing  
Fritz Kautsky  
Juan-Carlos Mayor  
Ove Stephansson  
Chin-Fu Tsang

January 2005, Stockholm, Sweden

## Summary

Task 2A concerns coupled TH modeling of the DST test at Yucca mountain, with given results for geologic, thermal, mechanical, hydrologic, and mineralogic and petrologic characterization, as-built configuration of the test block of DST, including locations of various sensors and measuring instruments and the plans for heating and cooling, including expected heater powers at various times, and requiring predictions for distributions and evolutions of the temperature and saturation fields. Three teams of ENRESA (Spain), DOE (USA), and NRC (USA) teams participated the task with different approaches, using FEM code Bright with a double porosity structure (ENRESA), a FDM code MULTIFLO with a dual continuum approach and an active fracture model (NRC) and a FDM code TOUGH 2 with a dual permeability approach (DOE), respectively.

Based on the results of the temperature and moisture distributions and temperature histories, it can be concluded that in general, the three models capture the TH response of the DST fairly well, although there are some differences between the teams' results. Conduction is the dominant heat-transfer mechanism in the fractured unsaturated rock in the DST, especially in the sub-boiling regime. However, the pore water plays an important role near the boiling point as it goes through cycles of vaporization and condensation causing the so called heat-pipe effect. A characteristic signature of heat-pipes – a short lull in the rise of temperature– was captured by all three teams.

The 2D modeling of the DST carried out by the ENRESA team initially was characterized by very little diffusion of vapor because the tortuosity factor was set at a low value of 0.05 and is referred to as the ND (No Diffusion) case. The recent 3D model with a tortuosity factor set at 1 and a vapor diffusion enhancement coefficient allows maximum vapor diffusion and is referred to as the MD (maximum diffusion) case. Comparative analyses of the modeling results for ND and MD cases lead to the conclusion that diffusion of vapor play an important role in flow and transport in the dry-out zone, since vapor mass fraction reaches its maximum in that region. Vapor flows by advection and by vapor diffusion/dispersion. Advection is very efficient in the high permeability fractured rock; however, diffusion is also a very efficient transport mechanism due to the high diffusivity of vapor in air.

The NRC research team examined two grid block sizes of 04 m and 5.0 m as well as two infiltration rates and the dual permeability model (DKM) with and without the active fracture model (AFM). An increase in model block size allowed relatively large infiltration rates (3.0 mm/yr) while maintaining a moderate ambient matrix saturation of 0.90. There was significant difference in the predicted matrix saturations between the small block model and the large block model as indicated by the larger dry-out zone in the small block model especially at four years after the start of heating.

The sensors in borehole 160, located between two wing heaters, display a wide variety of responses depending on their location with respect to the heaters. The ones located directly above the wing heaters exhibit strong thermal perturbation. Both measured and simulated temperature results have relatively short heat-pipe signals, suggesting that pore water is boiled off in a relatively short time period because of close proximity to the heaters.

# Content

Foreword		Page
1	Yucca Mountain Project Drift Scale Test	1
	1.1 Yucca Mountain Project Drift Scale Test	1
	1.2 Test setting and test facility	2
	1.3 Measurements made	3
2	Task 2A – thermal hydrologic simulation	5
	2.1 Task definition	5
	2.2 Task 2A research teams	5
3	Modeling of Drift Scale Test thermal-hydrologic (TH) response	6
	3.1 ENRESA research team’s TH modeling	6
	3.2 NRC research team’s TH modeling	32
	3.3 DOE research team’s TH modeling by using code TOUGH	52
4	Discussion and conclusions	72
	References	74
	Appendix	76



# 1. Yucca Mountain Project Drift Scale Test

## 1.1 Yucca Mountain Project Drift Scale Test

The DST in Yucca Mountain in Nevada, USA is a large scale, long term field thermal test being conducted for the U.S. DOE. In the DST a ~5 m diameter drift, ~ 50 m long is being heated by electrical heaters to study the response of the surrounding rock mass to the heating and subsequent cooling. The test is an integral part of DOE's program of site characterization at Yucca Mountain to assess whether the mountain is suitable site for a repository for the disposal of high level nuclear waste and spent nuclear fuel. In Task 2 of DECOVALEX III project the DST is a test case in the process of developing and validating coupled process models.

### 1.1.1 Purpose and test objective

In the broadest sense the primary purpose of the DST is to develop a thorough understanding of the coupled thermal (T), mechanical (M), hydrologic (H), and chemical (C) processes in the rock mass immediately surrounding the proposed repository because of the decay heat from the nuclear waste. To achieve this primary purpose a series specific sub-tier test objectives are established, categorized around the four principal processes of concern. These test objectives are:

#### Thermal

- ❑ Measure the temporal and spatial distributions of temperature
- ❑ Evaluate influence of heat transfer modes
- ❑ Investigate possible formation of heat pipes
- ❑ Determine rock mass thermal properties

#### Mechanical

- ❑ Measure rock mass mechanical properties
- ❑ Evaluate ground support response under controlled conditions
- ❑ Measure drift convergence at elevated temperatures
- ❑ Observe effect of thermal loading on prototypical ground support systems and overall room stability

#### Hydrological

- ❑ Measure changes in rock saturation
- ❑ Monitor the propagation of drying and subsequent re-wetting, if any, including potential condensate cap and drainage
- ❑ Measure changes in bulk-permeability (pneumatic)
- ❑ Measure drift-air humidity, temperature, and pressure

#### Chemical

- ❑ Collect and analyze samples of water and gas
- ❑ Analyze changes in typical waste package material left in the heated drift
- ❑ Observe changes in water and mineral chemistry from drying and reflux conditions

## 1.2 Test setting and test facility

A description of the setting of the DST and the test facility can be found in Datta et al, 1999 which is the basis of the following paragraphs.

Yucca Mountain, approximately 135 kilometers northwest of Las Vegas, Nevada is part of a series of north-trending ridges in the Great Basin physiographic province of North America. The mountain is underlain by 1000 to 1500 meters of Tertiary volcanic tuffs, formed from the ash of eruptions occurring between 8 and 16 million years ago. The volcanic tuffs are generally bedded, separated in beds that are generally non-welded to densely welded, and in addition, some are devitrified and others are vitric. The proposed repository horizon is within a sequence of beds, up to 350 meters thick, of moderately to densely welded devitrified tuff known as the Topopah Spring Tuff of the Paintbrush Group. The sub-units of the Topopah Spring Tuff are based primarily on the abundance of lithophysae which are cavities with dimensions on the order of millimeters to hundreds of millimeters, formed due to the presence of gases in the cooling ash flows. The presence or absence of lithophysae can have a pronounced effect on the mechanical and hydrologic properties of the rocks.

Topopah Spring Tuff is divided into four sub-units: the upper and lower lithophysal and the middle and lower non-lithophysal. The geologic symbols for the upper and lower lithophysal sub-units are Ttpul and Ttpll respectively while those for the middle and lower non-lithophysal sub-units are Ttpmn and Ttpln respectively. The lower non-lithophysal sub-unit (Ttpln) is stratigraphically the lower most, overlain by Ttpll, Ttpmn, and Ttpul in that order. The bulk of the proposed repository will be located in the lower lithophysal (Ttpll) sub-unit, with small portions in the middle and lower non-lithophysal sub-units. In the hydrologic stratigraphy of the Yucca Mountain area, the symbols for these sub-units of Topopah Spring Tuff are tsw33, tsw34, tsw35, and tsw36 with tsw36 being the lower most and tsw33 being the upper-most, corresponding to Ttpln and Ttpul respectively.

The DST is located entirely in the middle non-lithophysal sub-unit of Topopah Spring Tuff which is represented by Ttpmn or tsw34. These geologic or hydrologic symbols are frequently employed in this report to specify the beds.

The DST consists of a 47.5m long, 5m diameter drift heated by nine canister heaters, each 1.7m diameter, 4.6m long, placed on the floor of the drift. Additional heat is supplied by 50 rod heaters, referred to as "wing heaters" inserted into horizontal boreholes drilled into each sidewall. (Figure 1-1). The drift cross-section and the canister heaters are approximately the sizes of drifts and waste packages, respectively, being currently considered for the potential repository. The wing heaters are used to simulate the heat that would come from adjacent drifts in a repository, and thus provide better test boundary conditions. Each canister heater can generate a maximum of 15kW. The wing heaters are each 10 meters long, and have inner and outer segments that can generate 1145W and 1719W, respectively. Rockbolts and wire-mesh are installed as ground support along the entire length of the Heated Drift. In addition, the final 12.5m length of the drift is supported by a cast-in-place concrete liner to observe the performance of a concrete-lined drift at elevated temperatures. An Access/Observation Drift excavated parallel to the Heated Drift, and a perpendicular Connecting Drift are constructed around the periphery of the test block (Figure 1-1). The heated length of the drift is isolated from the Connecting Drift by an insulated thermal bulkhead. The bulkhead is not a pressure bulkhead. This means that some heat exchange by convection through the bulkhead will occur. Approximately 3300meters of boreholes are drilled from the Heated Drift, the Connecting Drift and the Access/Observation Drift

into the test block (Figures 1-1, 1-2, and 1-3) to house the wing heaters and approximately 3500 sensors of various types. By the end of the heating phase of the test extending over four years, approximately 15,000 m<sup>3</sup> of rock will be heated above 100 degree Celcius. For complete and full descriptions of the DST, refer to the reports, “Drift Scale Test Design and Forecast Results” (CRWMS M&O, 1997) and “Drift Scale Test As-Built Report” (CRWMS M&O, 1998).

## 1.3 Measurements made

The following measurements are being made or were planned to be made in the DST:

1. Heater Power
2. Rock temperature by thermocouples and resistance temperature devices
3. Displacement in rock by multiple borehole extensometers
4. Deformation of concrete lining by convergence monitors
5. Strain in concrete by strain gages
6. Moisture content of the rock by neutron logging
7. Moisture content of the rock by electric resistivity tomography (ERT)
8. Moisture content of the rock by ground penetrating radar (GPR)
9. Acoustic or microseismic emissions
10. Relative humidity, temperature, and air pressure in sections of boreholes isolated by packers
11. Relative humidity, temperature, and air pressure in the Heated Drift and outside
12. Changes in fracture permeability (k) by pneumatic methods (air permeability) and gas tracer tests
13. Analyses of gas and water samples collected from the test block
14. Thermal conductivity and diffusivity by REKA (rapid evaluation of K and alpha) probe
15. Periodic video and infrared images of the inside of the Heated Drift
16. Rock mass modulus of deformation by the plate-loading test
17. Temperature on non-rock surfaces such as heaters, bulkhead, cable-trays, etc. using thermocouples
18. Mineralogic-petrologic characteristics of the rock before and after the test
19. Thermal, mechanical, and hydrologic properties of intact rock samples measured in the laboratory, before and after the test

In addition to the above, coupons of candidate materials for the waste container, cylindrical samples of concrete used for the cast-in-place liner, and native microbes have either been left in the Heated Drift or injected into the test block to study the effects of prolonged heating and cooling on them.

An approximately 6000 channel, automated data collection system (DCS) records measurements on an hourly basis. The DCS scans and records the readings of temperature, humidity, air pressure, MPBXs, strain gages, convergence monitors, and current and voltage for heater power. Other measurements, referred to as active testing, such as air-K measurements, neutron logging, ERT, acoustic emission, GPR, and REKA probe measurements are recorded periodically using independent data acquisition systems.

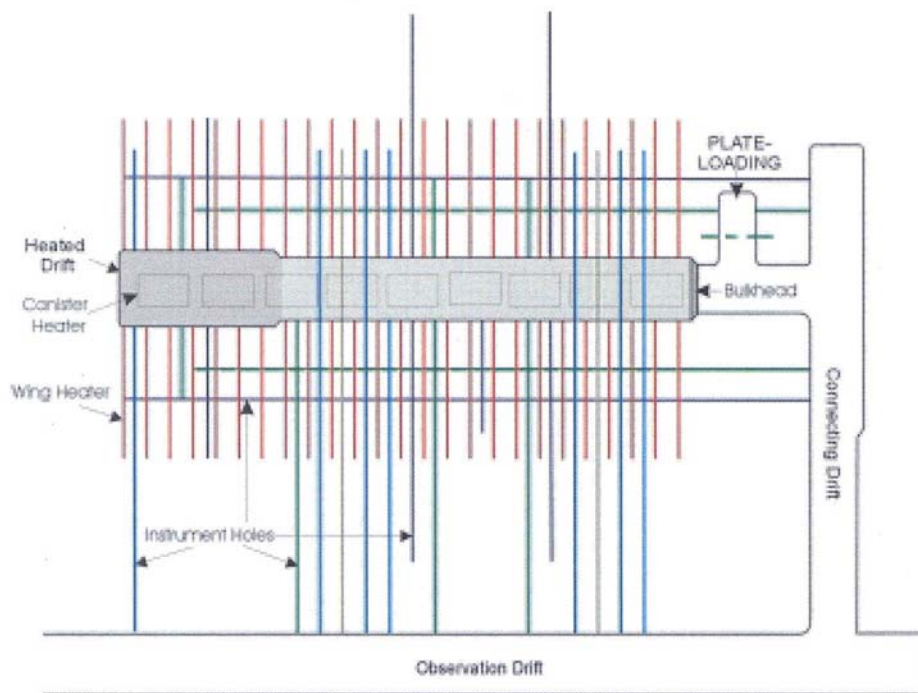


Figure 1-1. Location of the Wing Heaters, Canister Heaters and Instrument Holes in the Drift Scale Test

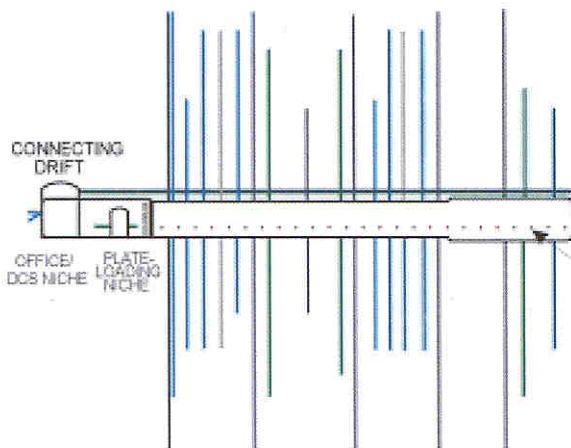


Figure 1-2. Cross-Section parallel to the Heated Drift

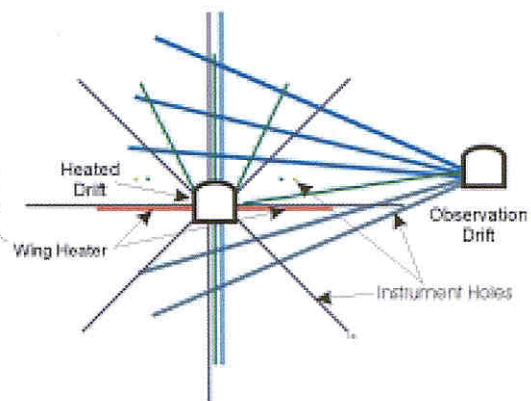


Figure 1-3. Cross-Section Orthogonal to the Heated Drift

## **2. Task 2A – Thermal hydrologic simulation**

Task 2 of the DECOVALEX III project is centered around the DST. There are four sub-tasks in Task 2 to study the three heat-driven coupled processes of interest. Task 2A is to study the TH response of the test block, while 2B/2C and 2D are to study the THM/TM and THC responses respectively.

### **2.1 Task definition**

The definition of Task 2A is quoted below from the Task 2 Plan of DECOVALEX III.

#### **Given:**

- a. Results of geologic, thermal, mechanical, hydrologic, and mineralogic and petrologic characterization of the test block of the DST
- b. As-built configuration of the test block, including locations of various sensors and measuring instruments
- c. Plans of heating and cooling, including expected heater powers at various times

#### **Tasks:**

1. Predict the time-evolution of temperature distribution in the test block; a suitable time Interval such as 10, 30, 50, or 100 days may be used
2. Predict the time-evolution of the changes in the saturation of the rock; a time interval of 10,30, 50, or 100 days may be used. Changes in the saturation can be predicted relative to the initial ambient saturation
3. Prepare Interim report documenting the results of the initial predictive analyses
4. Compare predicted temperatures and saturations with measured values. Perform comparative/interpretive analyses and refine conceptual and mathematical models, if necessary
5. Perform Phase II thermal-hydrologic modeling using refined model and actual heating i.e. measured heater outputs
6. Perform final comparative/interpretive analyses using Phase II modeling results and measured temperatures and saturations
7. Prepare Task 2A Report

### **2.2 Task 2A research teams**

Besides the U.S. DOE's Office of Repository Development (ORD) formerly known as Yucca Mountain Site Characterization Office (YMSCO), the participants in Task 2A are ENRESA of Spain and the NRC of the United States. The research team of ENRESA is led by Prof. Sebastia Olivella of the UPC in Barcelona, Spain. Ronald Green of the Center for Nuclear Waste Regulatory Analyses of the Southwest Research Institute in San Antonio, Texas leads the NRC's Task 2A research team. The DOE's research teams are led by Robin N. Datta.

## **3. Modeling of Drift Scale Test thermal - hydrologic (TH) response**

The heating phase of the DST was started on December 3, 1997. Prior to that, the DOE's research teams at the Lawrence Livermore National Laboratory (LLNL) and the Lawrence Berkeley National Laboratory (LBNL) performed predictive modeling of the TH response of the DST and documented the same in pre-test reports in June 1997. These pre-test predictive modeling by LLNL and LBNL constitute the first phase of Task 2A activities by DOE's research teams. Later, as the DECOVALEX III project started, Task 2A participants performed predictive modeling of the TH response of the DST per the task definition, Section 2.1. All the predictive TH modeling was documented in a DECOVALEX III Task 2A Interim Report in February 2002.

### **3.1 ENRESA research team's TH modeling**

The ENRESA research team's TH modeling of the DST is documented in the report, "Progress in THM Modeling of DST In Situ Test at Yucca Mountain", authored by Professors Sebastia Olivella, Antonio Gens, Claudia Gonzalez, and Miguel Luna of UPC in Barcelona, Spain.

#### **3.1.1 Introduction**

Initial Task 2A modeling of the DST in-situ test is described here. The modeling is performed at the UPC by the software CODE\_BRIGHT which is a finite element program developed to study a variety of problems, especially in unsaturated soils. The program is based on solving coupled equations representing mass (water and gas/air) and energy (heat) flow and mechanical equilibrium.

Preliminary THM calculations in 2-D are described. The primary objectives of these analyses are:

- understand the heating history, boundary conditions, and material properties in the DST.
- evaluate the capabilities of CODE\_BRIGHT to handle problems with temperatures well above 100°C.
- quantify the numerical effort in solving the problem in 2-D with the available computing resources at the center in UPC.
- investigate the intensity of the coupling between the mechanical processes and thermal and hydrological processes

To model THM mechanical problems in soils the CODE\_BRIGHT software has been developed to handle several features typical of these problems. The three assumptions on which the CODE\_BRIGHT software is based are:

- degree of saturation is always calculated from capillary pressure (retention curve)

- capillary effects in phase change follow psychrometric law
- liquid pressure, gas pressure, and temperature are state variables in thermal-hydrological problems

This section includes TH modelling of DST in situ test performed at Yucca Mountain performed at UPC using CODE\_BRIGHT. This is a finite element program developed to study a variety of problems, among them those involving unsaturated soils and rocks. The program solves the coupled equations of mechanical equilibrium, water flow, air flow, and energy flow. CODE\_BRIGHT has been used to model THM problems in soils so it has been developed with several features typical of the analyses of that type of problems.

This section contains the description of TH 2-D calculations of the in situ test DST. TH calculations were complemented by THM calculations that are not described in this report. Here two approaches are investigated. The first one consists in using a single structure approach that requires special treatment of some functions (e.g. relative permeability). A second part is devoted to investigate the way to perform double structure calculations.

### 3.1.2. Formulation

#### 3.1.2.1 General balance equations

In order to model the DST test the following set of equations is solved:

- a) Balance of water, which includes liquid water and vapor. Vapor concentration depends on temperature and capillary pressure according to psychrometric law and phase diagram of water.
- b) Balance of air, which includes air in the gas phase and also dissolved air. Henry's law is used for calculating the amount of dissolved air.
- c) Balance of energy, which includes enthalpy stored in the solid, liquid and gas phases.
- d) Stress equilibrium, which expresses balance of momentum for the medium as a whole. This equation is solved coupled to the balance equations.

Each balance equation has an associated unknown. For the equations considered here the unknowns are the following:

Liquid pressure:	$P_l$	Note
Gas pressure:	$P_g = P_v + P_a$	Due to the high permeability of the medium gas pressure remains almost at atmospheric pressure
Temperature:	$T$	
Displacements:	$[\mathbf{u}, \delta\phi = (1-\phi)\nabla\cdot\delta\mathbf{u}]$	Porosity changes as a function of volumetric strain changes $\nabla\cdot\delta\mathbf{u}$

### 3.1.2.2 Constitutive equations

The complete set of equations is obtained after incorporation of constitutive equations in the balance equations. The constitutive equations that are necessary for the THM modeling of the DST in situ test are:

Table 3.1-1 Constitutive equations

Retention curve/Saturation-capillary pressure:	van Genuchten, with $P_o(=1/\alpha)$ and $\lambda (=m)$
Intrinsic Permeability/Darcy's law:	Variable with $\phi$
Relative Permeability/Darcy's law:	van Genuchten, $m'$ . In principle $m=m'$ but non-equal coefficients can be considered in order to represent a double structure medium
Vapor diffusion/Fick's law:	depends on temperature and pressure
Thermal conductivity/Fourier's law:	geometric mean including porosity and saturation dependences
Elasticity/Stress-strain law:	Mechanical and thermal effects with linear formulations

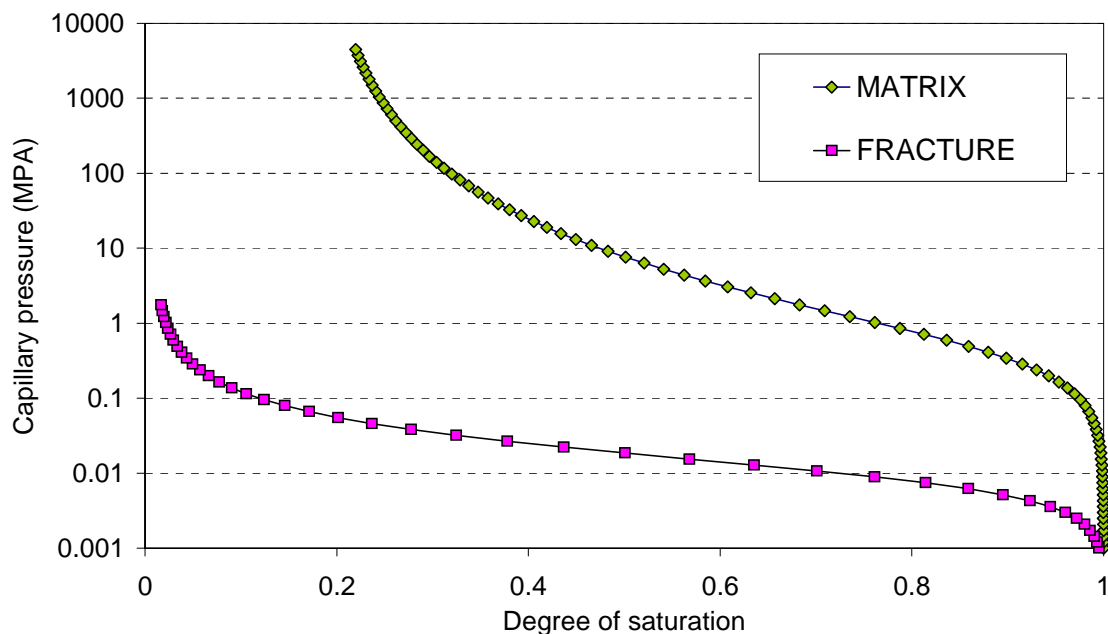


Figure 3.1-1. Retention curves for matrix and fractures.

Figure 3.1-1 shows representative retention curves that are considered by Birkholzer and Tsang (2000) for DST modelling. It can be observed that the matrix has a higher desaturation capillary pressure compared to the fractures, that desaturate at lower capillary pressures. Therefore, assuming equilibrium between fracture and matrix, desaturation in the rock will progress in the following way: first the fracture will desaturate and only when the fracture is practically desaturated (for instance at 0.1 MPa), the matrix is starting to desaturate.

The modified functions of relative permeability for the single structure analysis are shown in Figure 3.1-2 that consider  $m = 0.04$  for liquid and  $n = 0.8$  for gas. It must be

noted that  $m = 0.04$  is only considered for liquid relative permeabilities while the values of  $m$  for the retention curve of the matrix are maintained. In other words, the shape parameter is not the same in the retention curve and in the relative permeability functions because of the different importance of matrix and fracture. While matrix is important for storage of water, the fracture is important for the flow of water.

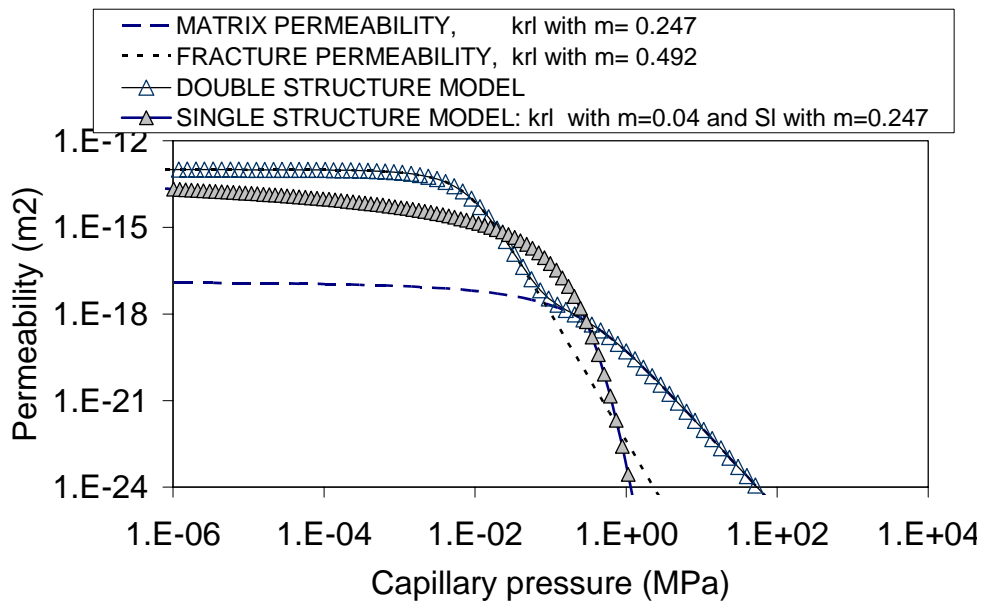
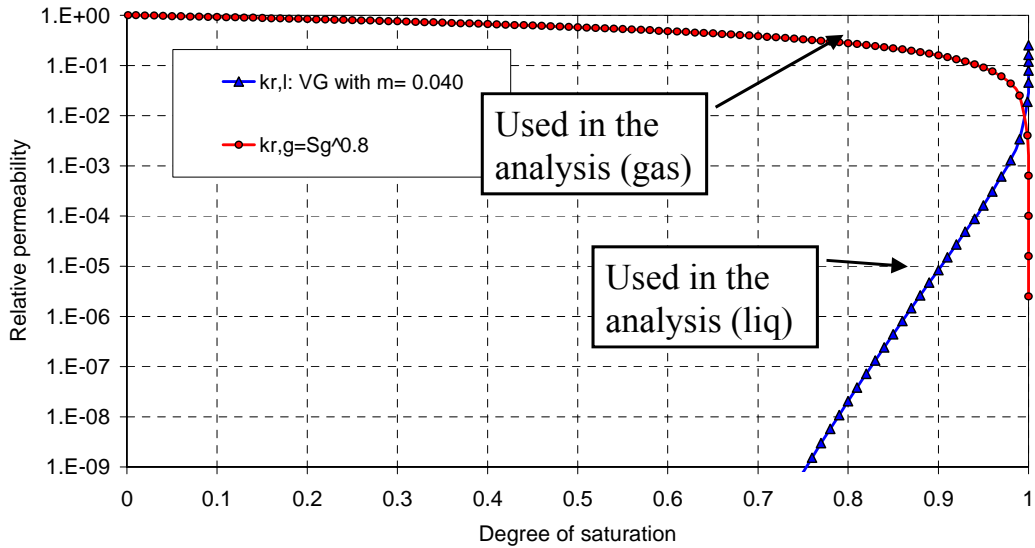


Figure 3.1-2. Relative permeability functions used in single structure analysis (above) and equivalent permeability as a function of capillary pressure (below).

### 3.1.2.3 Equilibrium restrictions

Psychrometric Law and Henry’s Law are equilibrium restrictions. They give the partitioning coefficients for calculating the species mass present in each phase.

### 3.1.2.4 Additional hypothesis

The present analysis ignores the concrete invert at the base of the drift. The heat power is applied to the canister and the wings with a 70 % reduction of the actual value in order to consider, in an approximate manner, 3D thermal dissipation effects since the analysis is performed in 2D. This power reduction is a simplification of the actual situation. The adopted power values in canister and wings are:

Canisters:  $36400\text{W}/\text{canister}/(9 \text{ canister} \times 4.7 \text{ m}) = 860 \text{ W/m}$   
 Inner wing heaters:  $37520 \text{ W}/\text{wings}/(50 \text{ wings} \times 1.87 \text{ m}) = 401 \text{ W/m}$   
 Outer wing heaters:  $55300 \text{ W}/\text{wings}/(50 \text{ wings} \times 1.87 \text{ m}) = 591 \text{ W/m}$

Figure 3.1-3 describe the power evolution in the time, a) canister and b) wings, according to experimental data, the line fit to actual power and the function considered. The application of a reduction of the power in the two-dimensional calculation is justified by thermal calculation of the three-dimensional problem (Appendix).

Liquid pressure at the bottom of the domain was calibrated in order to obtain a 92% degree of saturation in the initial phase taking into account the infiltration.

These parameters have been obtained from previously reported experimental data. Parameters are summarized in Table 3.1-2.

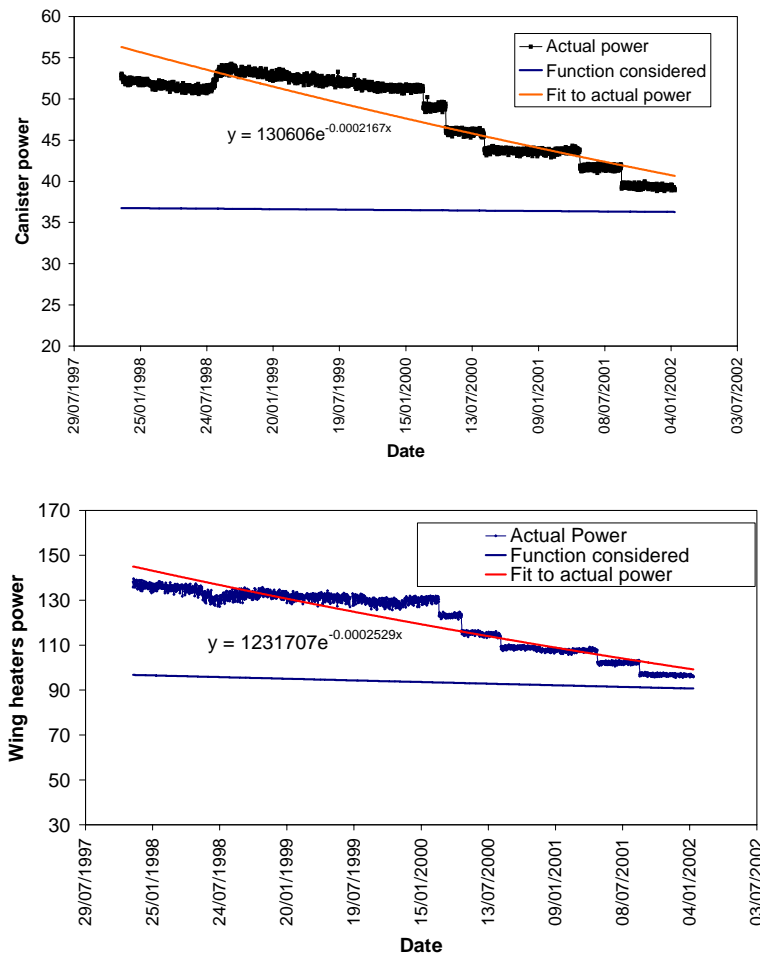


Figure 3.1-3 Power in the different elements: in canisters (above) and in wings (below). The function considered corresponds to a fit for 2 years and 70% reduction.

Table 3.1-2 Parameters used in the modelling

<i>Mechanical</i>			
Elastic parameters			
Young modulus, $E$	3.68E+04		
Poisson coeff. $\nu$	0.2		
Thermal expansion coef.	2.00E-05		
<i>Thermal</i>			
Thermal conductivity			
Dry	1.67		
Saturated	2.10		
Solid phase properties			
Specific heat	865		
Density	2510		
<i>Hydrological</i>			
	<i>Mat 3</i>	<i>Mat 2</i>	<i>Mat 1</i>
Porosity,	0.154	0.11	0.13
Retention curve			
$P_o (1/\alpha)$	0.0943	0.444	0.354
$\lambda=m$	0.243	0.247	0.207
Residual saturation	0.06	0.18	0.08
Maximum saturation	1		
Molecular Diffusion			
$D_m^{vapor} = \tau D \left( \frac{(273.15 + T)^n}{P_g} \right)$	$D=5.9 \cdot 10^{-6} \text{ m}^2/\text{s}/\text{K}^{-n}\text{Pa}$ $n=2.3$		
Dispersion			
$\alpha_l$	10 m		
$\alpha_t$	1 m		
Intrinsic permeability Initial $k_o$	<i>m1</i> (lower)	$0.187 \times 10^{-11}$	
	<i>m2</i> (intermediate)	$0.1 \times 10^{-12}$	
	<i>m3</i> (upper)	$0.635 \times 10^{-12}$	
Intrinsic permeability $k$	<i>m1</i> (lower)	Exponential law: Variable with porosity $k = k_o \exp(-b(\phi_o - \phi))$ $b = 500, 1000, 2000$ and $-1000$	
	<i>m2</i> (intermediate)		
	<i>m3</i> (upper)		
Liquid relative permeability: Van Genuch. model, value of $\lambda=m=0.04$ in VG model		$\lambda$ is the shape parameter in the VG retention curve. Also referred as $m$	
Gas relative permeability: $k_{rg} = A_g (1 - S_e)^{\lambda_g}$		$A_g = 1; \lambda_g = 0.8$	

### 3.1.3 Geometry, boundary conditions and mesh

We performed a two-dimensional (2-D) analysis on a rectangular model 180 m wide and 250 m high containing the 5 m diameter heated drift at the centre. The boundary conditions are shown in Figure 3.1-4. Initial conditions are obtained simply by calculating a steady state regime under isothermal conditions. This steady state was first obtained in a one-dimensional case. The negative water pressure imposed at the bottom boundary is selected in such a way that the initial degree of saturation in the vicinity of the drift is about 92%.

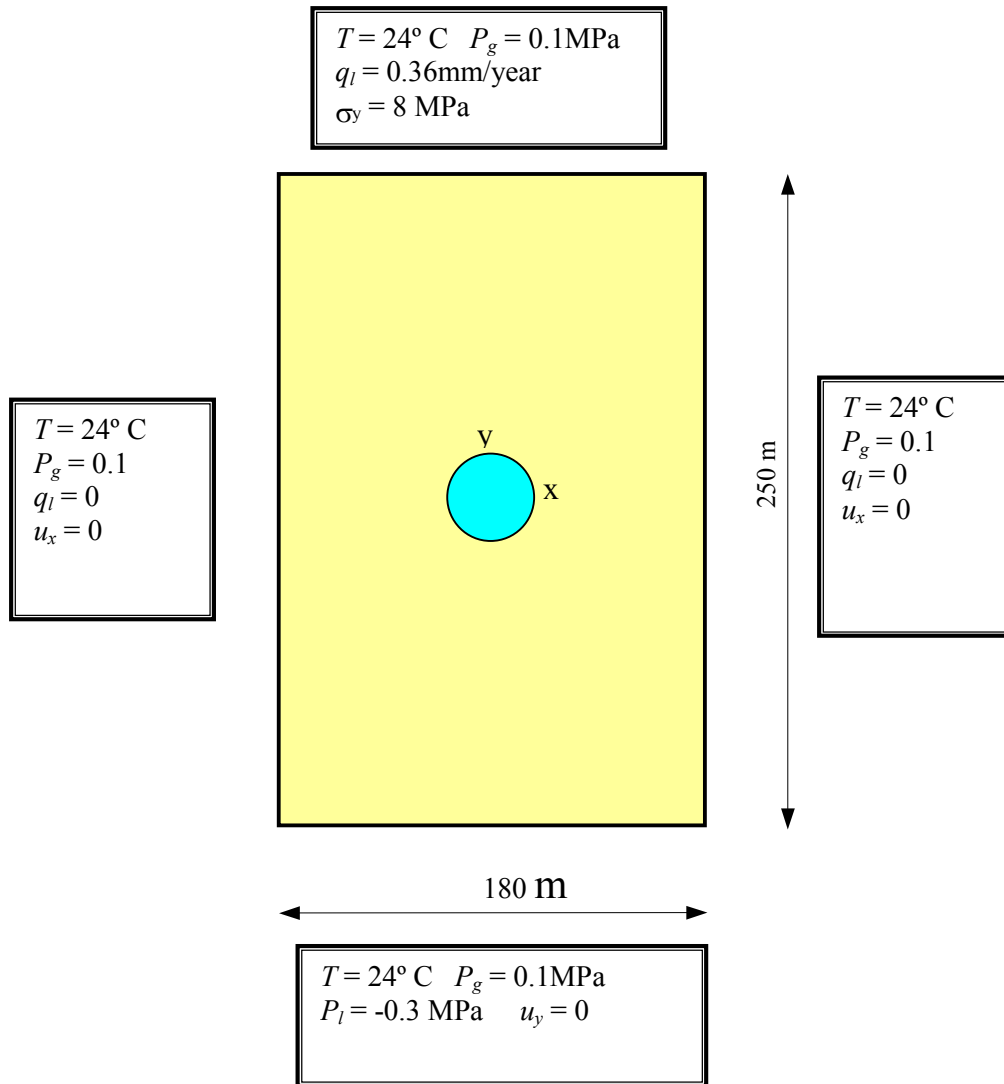


Figure 3.1-4. Geometry and boundary conditions for the THM problem.

This analysis has been performed with a mesh containing 2439 nodes and 4802 triangular elements, see Figure 3.1-5

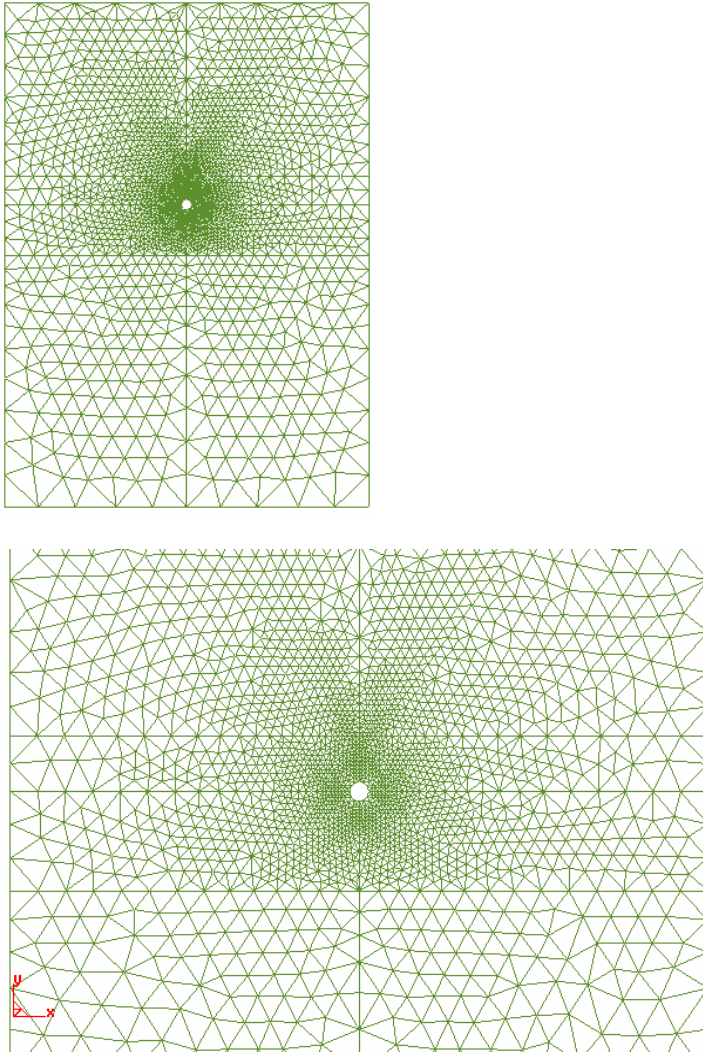


Figure 3.1-5. Finite element mesh used in THM calculations.

### 3.1.4. Results of temperature and water saturation

The distributions of temperature and degree of saturation after 90, 365 and 1460 days of heating are shown in Figure 3.1-7. It can be seen that the temperature distribution shows clearly the presence of the heaters. Degree of saturation is of the order of 0.92 at the level of the drift before heating started. Due to heating effects, drying takes place and degree of saturation decreases down to 0.25, which implies very high capillary pressures. After 365 days (1 year) of heating, the desaturated zone has a shape remarkably influenced by the wing heaters. After 1460 days (4 years) of heating, the desaturated zone is approximately elliptical.

Figures 3.1-8 and 3.1-9 show the temperature evolution at different nodes, which are indicated in Figure 3.1-6. Comparison with measurements (which are included in each plot) indicates that temperatures are quite good in some points and show some deviations in others. Also, for the first two years results are better than for the third and fourth year.

Measurements were available for only two years when the TH modelisation was set up. For the first and second year, constant power (with only a slow decay) was considered appropriate. The constant power corresponds to 70% of the nominal value

(see Appendix). Power after two years would probably require a higher decay factor. This is confirmed by the too high temperatures calculated at some points for the 3<sup>rd</sup> and 4<sup>th</sup> year. However, since this is a 2D model, and uses a modified power, it was considered that further attempts to use a more realistic power were not justified.

Finally, profiles of temperature are represented in Figures 3.1-10 and 3.1-11 for boreholes 158, 160 and 162. The effect of the wing heaters is clearly observed in borehole 160 (this borehole is indicated in Figure 3.1-6). Profiles for the first and second year show good accuracy, but for longer times, temperature is overpredicted due to the reasons explained before.

As additional information, Figure 3.1-12 shows gas pressure development. It can be observed that the shape is similar, however, the gas pressures in the model calculations presented here are higher than the ones obtained by Datta (2002). This is probably due to the gas relative permeability curve which, in this simple porosity model, depends on the averaged gas saturation.

In order to understand completely the process of water flux, both in the liquid and in the gas phase according to this model, Figures 3.1-13 and 3.1-14 are included. Figure 3.1-13 shows liquid fluxes around the heated area. It can be observed that at one year the heating process is very active and water fluxes show the combined effects of drying and gravity. At four years, the dried zone is developing very slowly and diverts the vertical fluxes of liquid water due to its very low conductivity. Figure 3.1-14 shows that, for gas fluxes, gravity is not important due to the low density of gas. In fact, the gas phase is dominated by vapor and, hence, as the drying progresses these gas fluxes decrease near the heaters, but they are significant in the drying front. The drying front corresponds well with the elliptical shape observed in Figure 3.1-7.

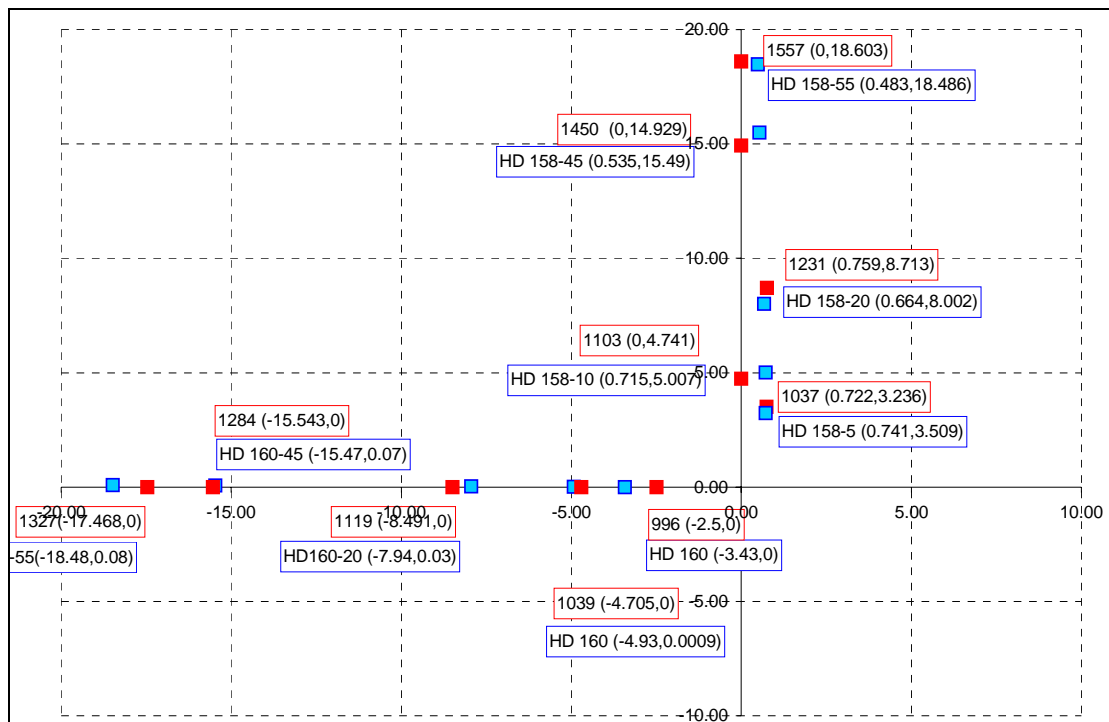


Figure 3.1-6 Points with measurements and calculations of temperatures ( $x = 0$  and  $y = 0$  is the center of the drift). Note: This plot shows the actual location of the measurement points in boreholes 158 and 160 and the corresponding nodes in the finite element mesh that were used for comparison.

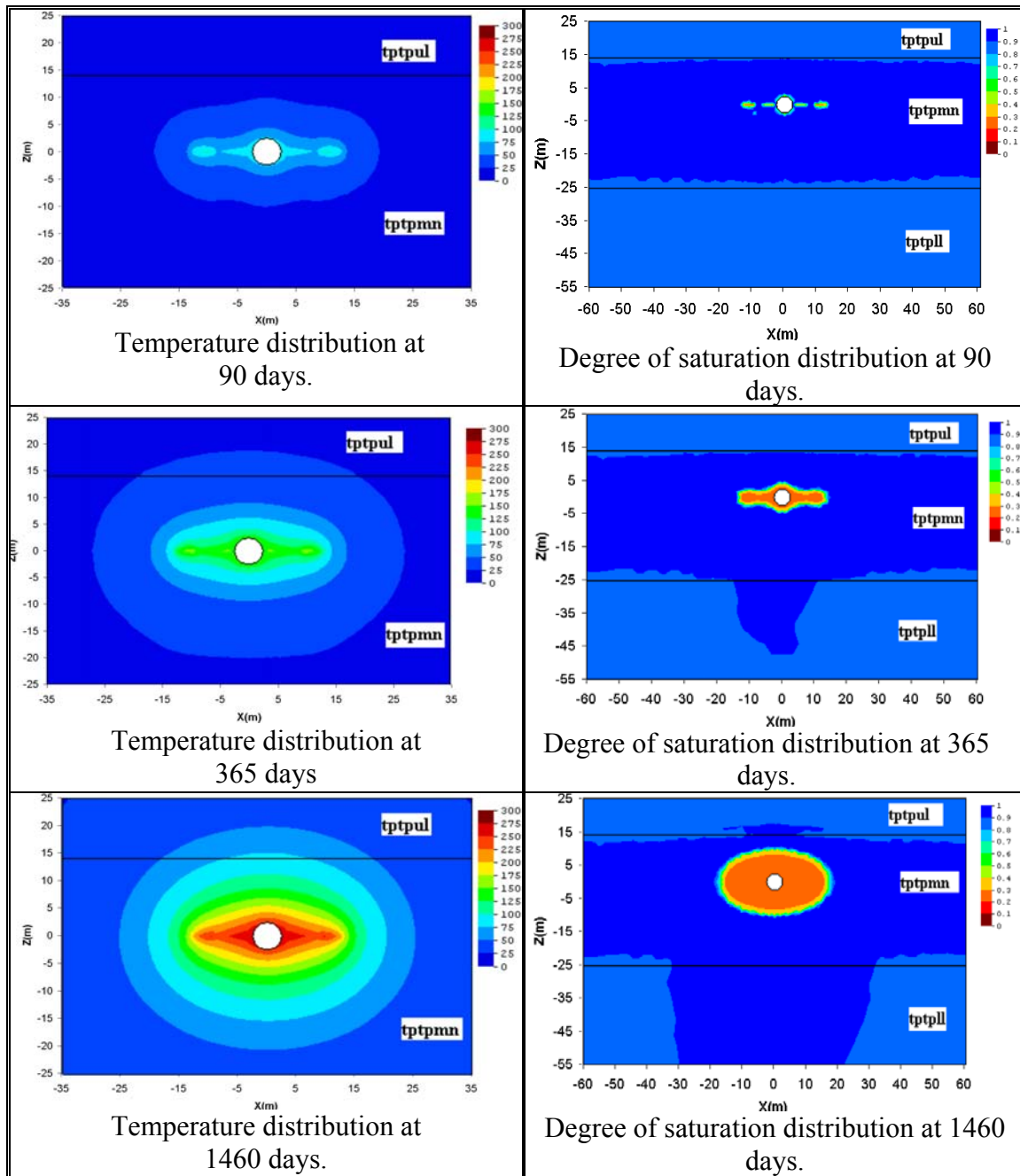


Figure 3.1-7 Temperatures and degree of saturation distributions

### 3.1.5. Double Porosity Structure modeling by using CODE\_BRIGHT

In the final phase of its Task 2 research the ENRESA team used a double porosity structure approach to perform THM modeling of the DST by the CODE\_BRIGHT software. The TH aspect of this double structure modeling is described below.

#### 3.1.5.1 Model description

The present model consists of a double structure approach to the problem of modelling the DST experiment at Yucca Mountain. The double structure approach is

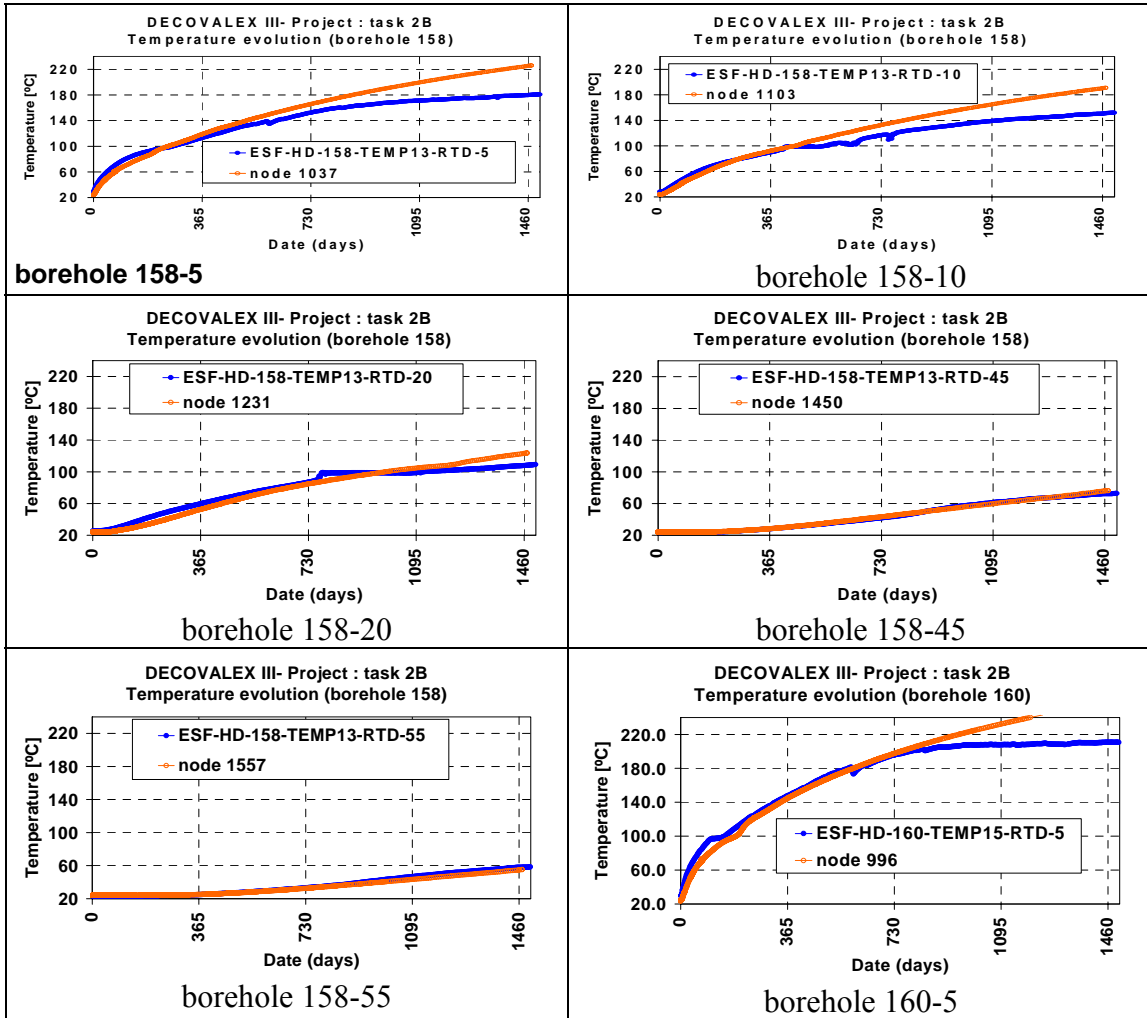


Figure 3.1-8. Time History of Temperature at selected points

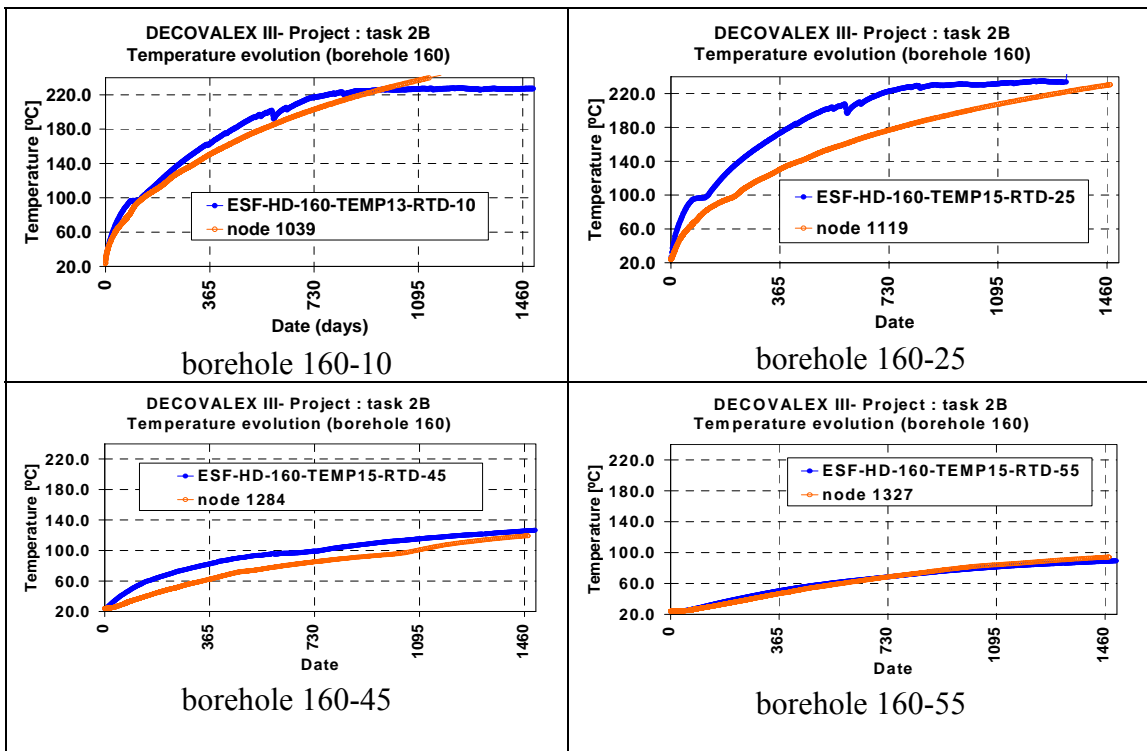


Figure 3.1-9. Time History of temperature at selected points (cont from 3.1-8)

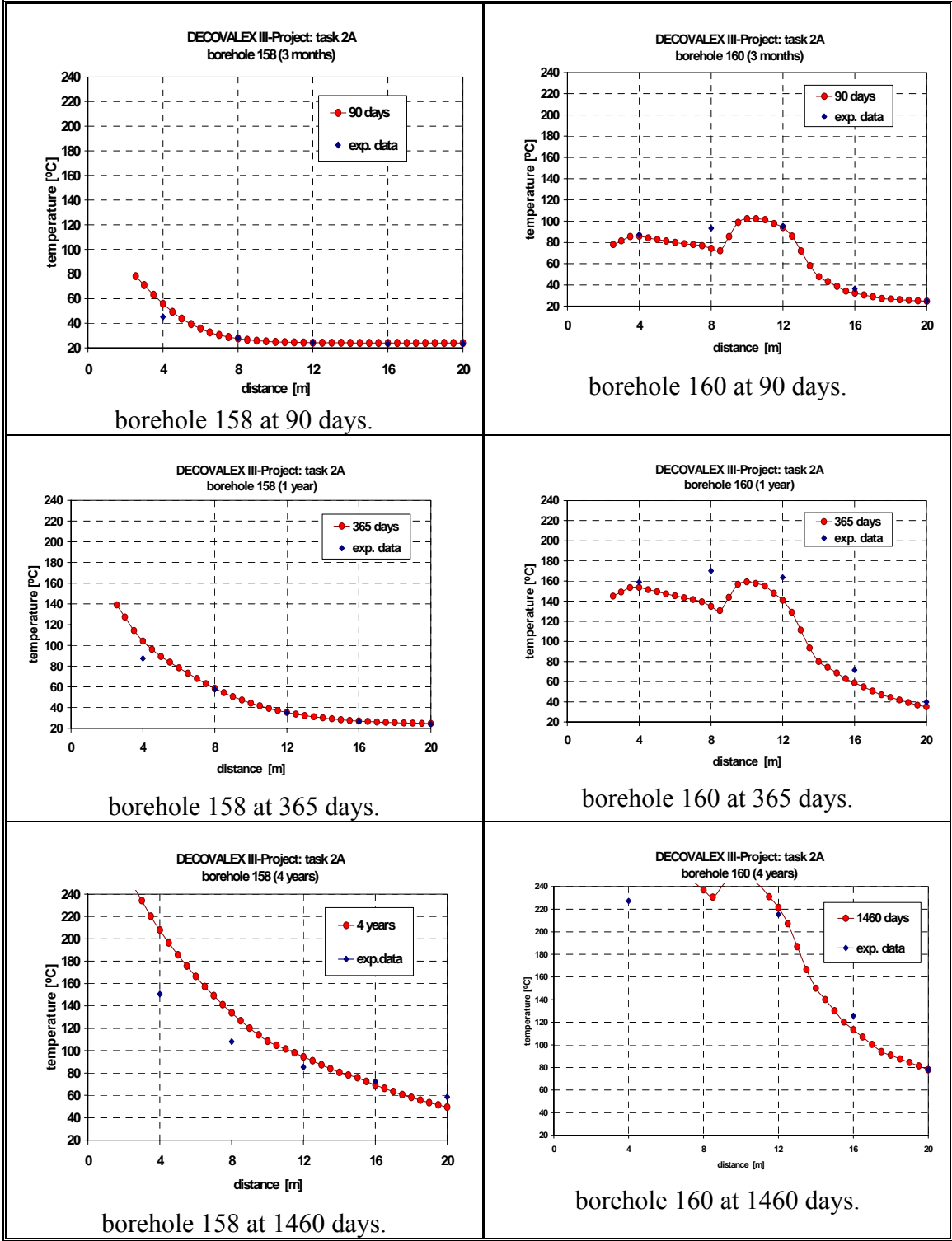


Figure 3.1-10. Profile of temperature at selected boreholes

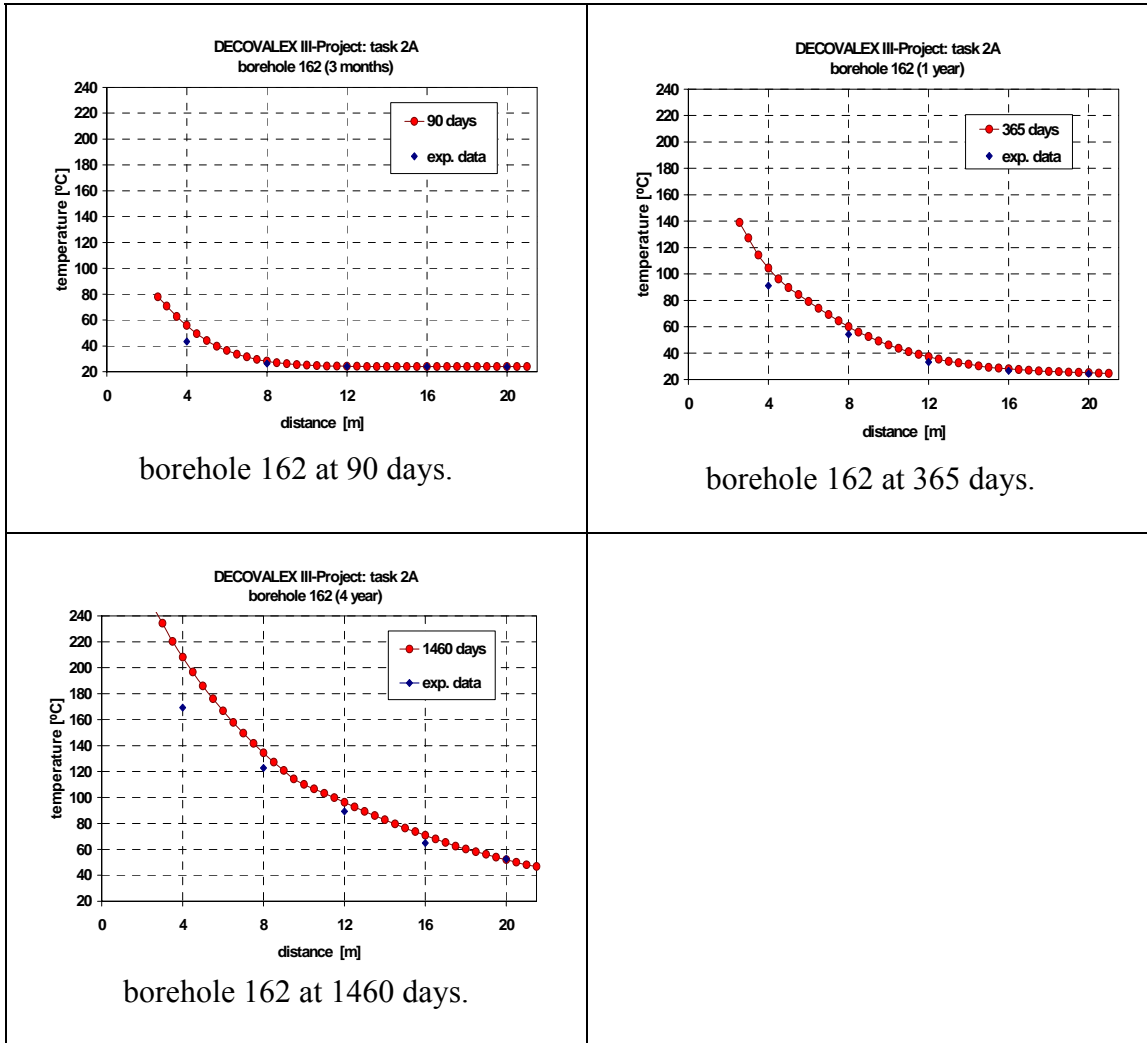


Figure 3.1-11. Profile of temperature at selected boreholes

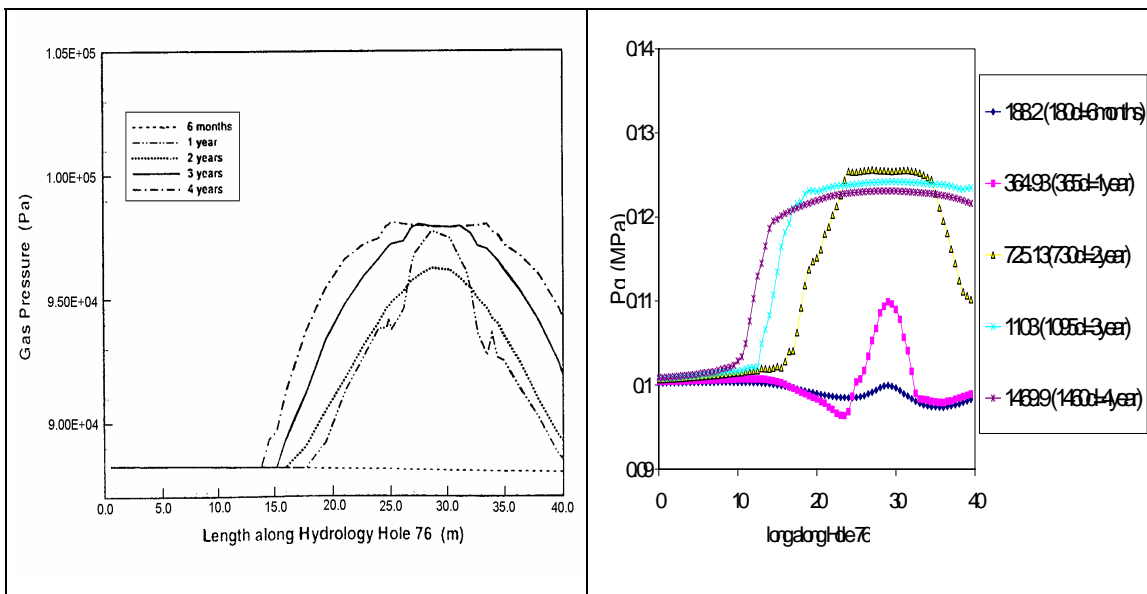
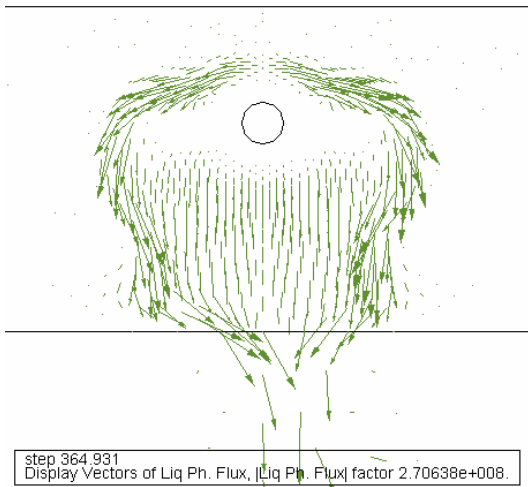
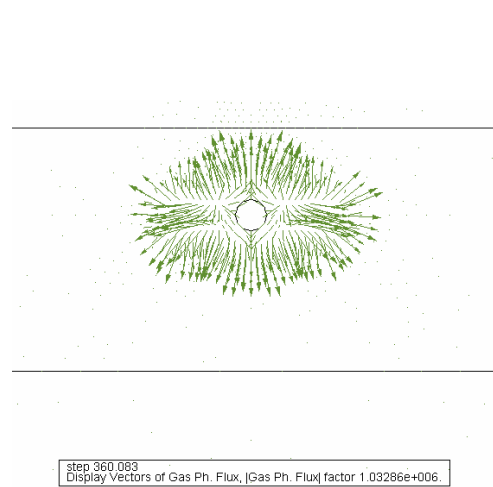


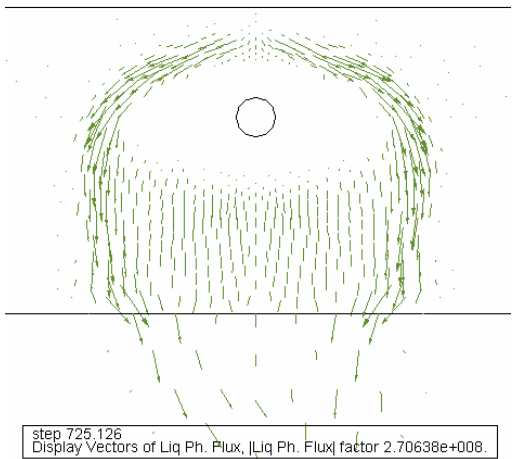
Figure 3.1-12. Profile of gas pressure (left: experimental, right: calculated)



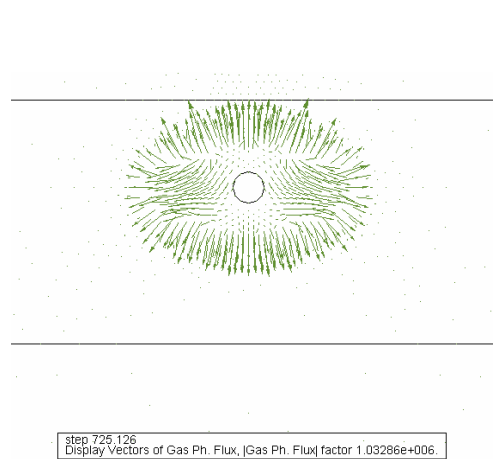
Liquid fluxes for 1 year.



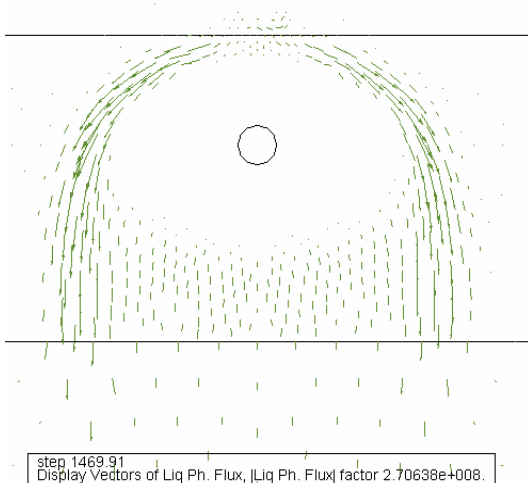
Gas fluxes for 1 year



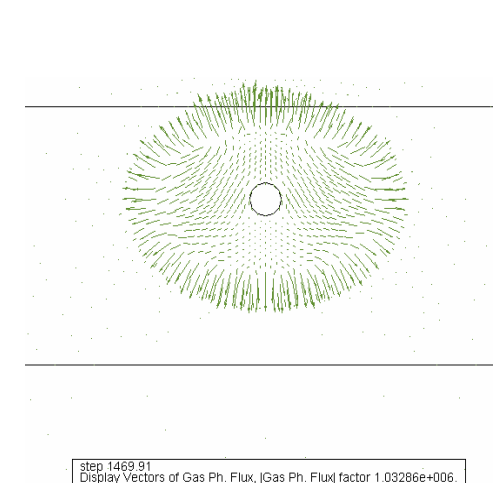
Liquid fluxes for 2 years.



Gas fluxes for 2 years



Liquid fluxes for 4 years.



Gas fluxes for 4 years

*Figure 3.1-13 Liquid fluxes for 1, 2 and 4 years. All flux vectors are represented with the same scale.*

*Figure 3.1-14 Gas fluxes for 1, 2 and 4 years. All flux vectors are represented with the same scale.*

achieved by means of a two meshes that are connected with one dimensional elements. Among other aspects, the present analysis takes into account the concrete invert at the base of the drift, which was not included in the single structure analysis considered previously. The heat power is applied to the canister and the wings using a reduced power of 70% of the nominal value. This reduction permits to obtain reasonable temperatures in the 2D case, even though it can not be considered a general rule. In fact, three dimensional effects are not negligible in this case and a simple way to improve the predictions of a 2D calculation is using a reduced power. A comparison of a simple thermal calculation i.e. only with heat flow is performed in 2D and 3D and has been included in an appendix in order to demonstrate the convenience of using a reduced power.

The model takes advantage of symmetry for the design of the mesh. Figure 3.1-15 shows a schematic representation of the way that the two meshes considered are connected. For each point in the domain, there is an element that belongs to the matrix and an element that belongs to the fracture. These elements are connected using 1-D elements between nodes of each medium. The length of the connexion between the matrix and fracture is a key parameter in the model. A reference value of the distance of connexion between the matrix and the fracture is 0.01 m (1cm).

As mentioned above, the concrete invert is taken into account, so there are eleven materials that can be seen in Figure 3.1-15. There are: 3 materials for the matrix, 3 materials for the fracture, 2 materials for the concrete invert, 1 material for the connexions and lineal elements that connect the heating nodes. This latter element is intended to get more homogeneous power distribution. The material parameters used in the modeling are summarized in Table 3.1-3.

The power applied to the heat sources is has been calculated on the basis of a 70% reduction from nominal power (see appendix). The actual heat power for the 2D model is calculated as:

- Canisters:  $0.7 \times 52000 \text{ W} / (9 \text{ canister} \times 4.7 \text{ m}) = 860 \text{ W/m}$
- Inner wing heaters:  $0.7 \times 53600 \text{ W} / (50 \text{ wings} \times 1.87 \text{ m}) = 401 \text{ W/m}$
- Outer wing heaters:  $0.7 \times 79000 \text{ W} / (50 \text{ wings} \times 1.87 \text{ m}) = 591 \text{ W/m}$

### **3.1.5.2 Domain considered and Finite Element mesh**

The ENRESA team performed a two-dimensional (2-D) analysis on a rectangular model 180 m wide and 250 m high containing half of the 5 m diameter heated drift and the wings corresponding to the half of the drift considered. The mesh contains 4932 nodes and 12051 triangular elements, and can be seen in Figure 3.1-16.

## **3.1.5 Results obtained**

The results corresponding to two calculations are presented in this section. The first calculation is characterized by very small diffusion of vapour since tortuosity coefficient was set to 0.05. This calculation only reached 2 years due to convergence problems related to the severe dry conditions occurring in the vicinity of the drift and wings. Since tortuosity coefficient was very small, vapour diffusion was also reduced and this case was referred as ND (No Diffusion) by comparison to another case that is described below which will be referred as MD (Maximum Diffusion). The MD case will incorporate a tortuosity coefficient equal to unity plus an enhancement factor in order to

increase the diffusivity in the low gas saturation zones. Firstly the results for the ND case are described. Afterwards, the MD case is explained and compared with the ND case.

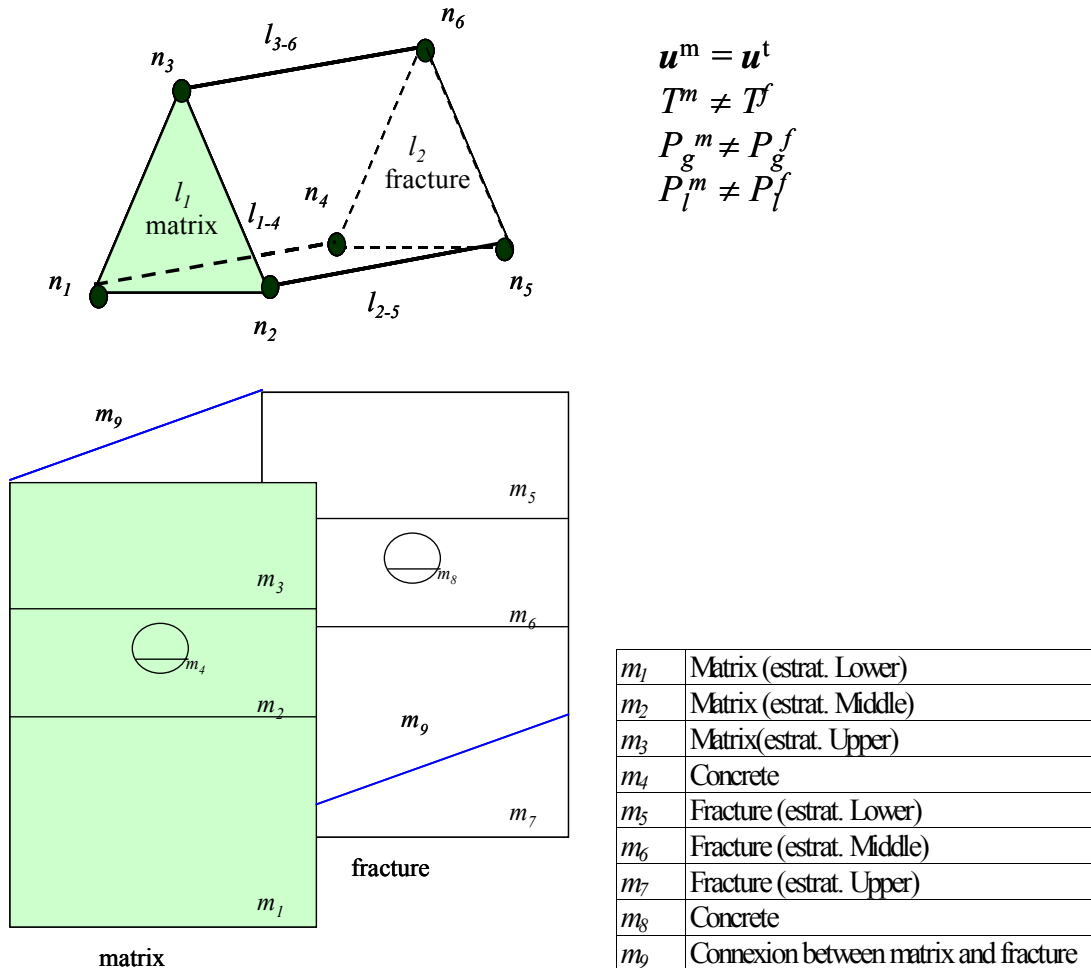


Figure 3.1-15. Schematic representation of the double structure approach

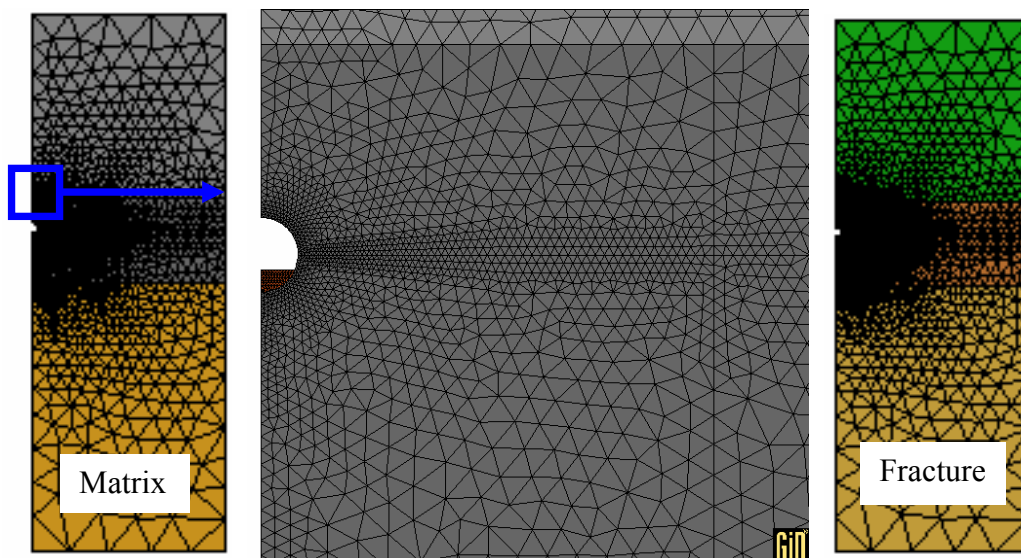


Figure 3.1-16. Finite element mesh used in THM calculations.

Table 3.1-3 Parameters for the different materials and constitutive laws.

Properties		Materials								
		Matrix			Fracture			Concrete inert		Connexion
		$m_1$	$m_2$	$m_3$	$m_5$	$m_6$	$m_7$	$m_4$	$m_8$	$m_9$
Mechanical	Elasticity	$0.368 \times 10^5$	$0.368 \times 10^5$	$0.368 \times 10^5$				$0.368 \times 10^6$	-	0
	Poisson Mod	0.2	0.2	0.2				0.2	-	-
Thermal	Coef. of thermal expansion	$0.2 \times 10^{-4}$	$0.2 \times 10^{-4}$	$0.2 \times 10^{-4}$				$0.2 \times 10^{-4}$	-	-
Retention curve	Press a tem	0.354	0.444	0.0943	0.0602	0.01027	0.006369	0.444	0.01027	0.1
	Lambda	0.207	0.247	0.243	0.492	0.492	0.492	0.247	0.492	0.2
	Residual	0.08	0.18	0.06	0.01	0.01	0.01	0.18	0.01	0.08
	Max. Saturac.	1	1	1	1	1	1	1	1	1
Relative permeability to gas: $k_{rg}$	Constant	1	1	1	1	1	1	1	1	
	Power	3	3	3	3	3	3	3	2.28	1-kr1
Perm to liq: $k_{rl}$	Lambda	0.207	0.247	0.243	0.492	0.492	0.492	0.247	0.492	0.2
Intrinsic permeability	$k_{xx}$ (m <sup>2</sup> )	$0.247 \times 10^{-15}$	$0.124 \times 10^{-16}$	$0.525 \times 10^{-17}$	$0.187 \times 10^{-11}$	$0.100 \times 10^{-12}$	$0.635 \times 10^{-12}$	$0.124 \times 10^{-16}$	$0.10 \times 10^{-12}$	
	$k_{yy}$ (m <sup>2</sup> )	$0.247 \times 10^{-15}$	$0.124 \times 10^{-16}$	$0.525 \times 10^{-17}$	$0.187 \times 10^{-11}$	$0.100 \times 10^{-12}$	$0.635 \times 10^{-12}$	$0.124 \times 10^{-16}$	$0.10 \times 10^{-12}$	
	$k_{zz}$ (m <sup>2</sup> )	-	-	-	-	-	-	-	-	$1 \times 10^{-15}$
	Porosity	0.13	0.11	0.154	0.00329	0.00263	0.00171	0.11	0.00263	$\cong 0$
Thermal Conductiv.	Dry	1.59	1.67	1.15	0	0	0	3.00	0	1.59
	Wet	2.29	2.10	1.70	0	0	0	3.00	0	
Solid Phase prop.	Specific heat	865	865	865	-	-	-	865	-	-
	Density	2540	2530	2510	-	-	-	2530	-	-
	Therm Exp.	$0.2 \times 10^{-4}$	$0.2 \times 10^{-4}$	$0.2 \times 10^{-4}$	-	-	-	$0.2 \times 10^{-4}$	-	-
Dispersion coeffs and energy	Sol Long	0.3	0.3	0.3	0.3	0.3	0.3	0.3	10	
	Sol. Transv.	0.03	0.03	0.03	0.03	0.03	0.03	0.03	1	
	Heat long	0.3	0.3	0.3	0.3	0.3	0.3	0.3	10	
	Heat transv.	0.03	0.03	0.03	0.03	0.03	0.03	0.03	1	
	Tortuosity	0.05	0.05	0.05				0.05		

### 3.1.5.1 Results for ND case

The distributions of temperature in the matrix after 1 year and 2 years are shown in Figure 3.1-17, degree of saturation after 1 and 2 years of heating for the matrix and the fracture are shown in Figures 3.1-18 and 3.1-19 respectively. As indicated, this analysis reached two years of heating, and Figure 3.1-20 shows several hydraulic variables at the end of this period. It can be seen, that due to the high vapour concentration and almost fully dry conditions, some instabilities appeared in some nodes.

Degree of saturation in the matrix and fracture are completely different due to the different retention curve in the matrix and in the fracture. The effect of gravity is clearly observed, especially for the fracture which shows a downward water flow.

Figure 3.1-21 shows other variables, such as the mechanical ones at 2 years of heating, that is displacements, horizontal stress, vertical stress and shear stress. Mechanical problem is considered elastic only and permeability is considered constant in this analysis.

The temperature evolution is shown in Figure 3.1-22, liquid pressure evolution in the matrix is shown in Figure 3.1-23, and finally, vapour pressure evolution in matrix is shown in Figure 3.1-24. It can be seen that an attempt to reduce the power in order to avoid higher temperatures is considered but the problems still persisted. The vapour pressure above the atmospheric pressure is an indication that the results are not sufficiently good and that convergence problems appeared due to insufficient vapour migration. Degree of saturation is of the order of 0.92 at the level of the drift before the heating starts. Due to heating effects, drying takes place and degree of saturation

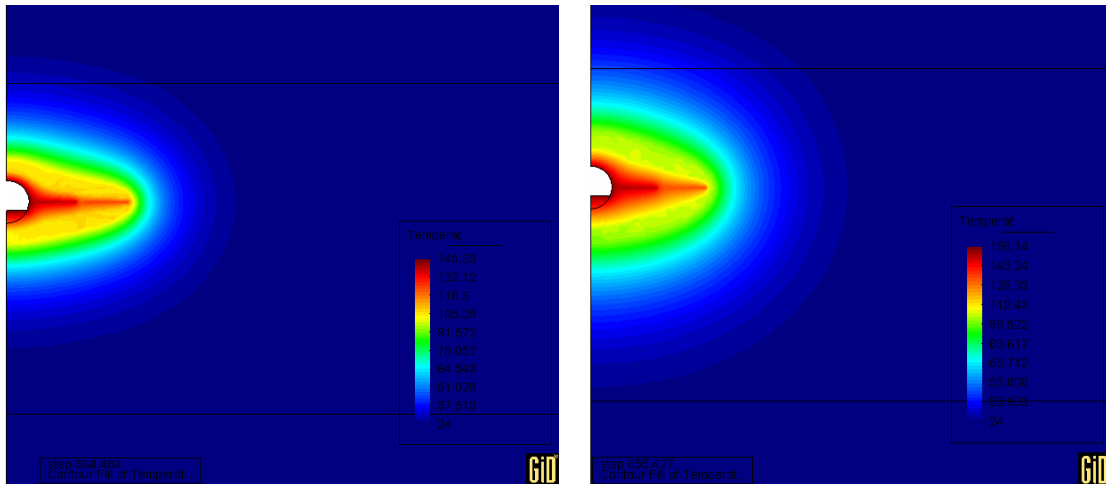


Figure 3.1-17. Temperature distribution at 1 year (left) and 2 years (right) of heating in matrix

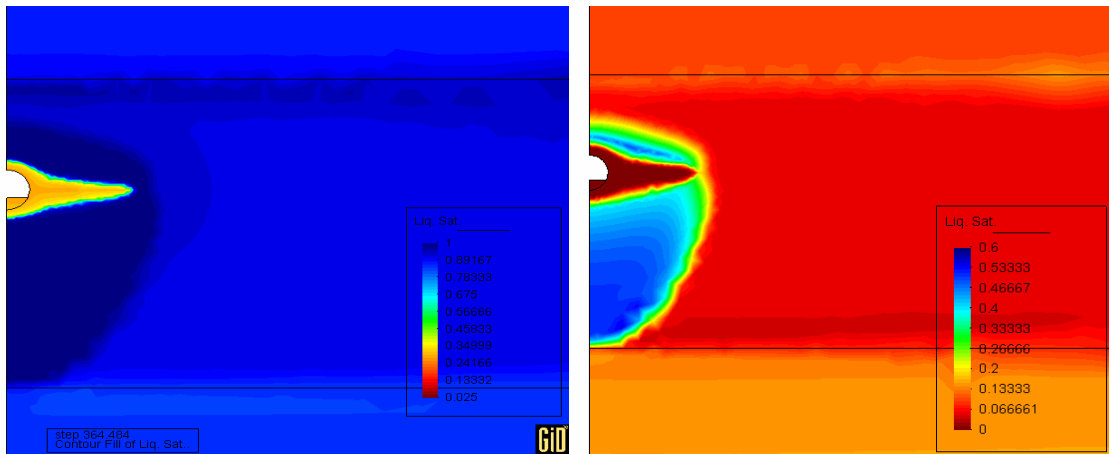


Figure 3.1-18. Degree of saturation distribution at 1 year of heating. Matrix on the left and fracture on the right

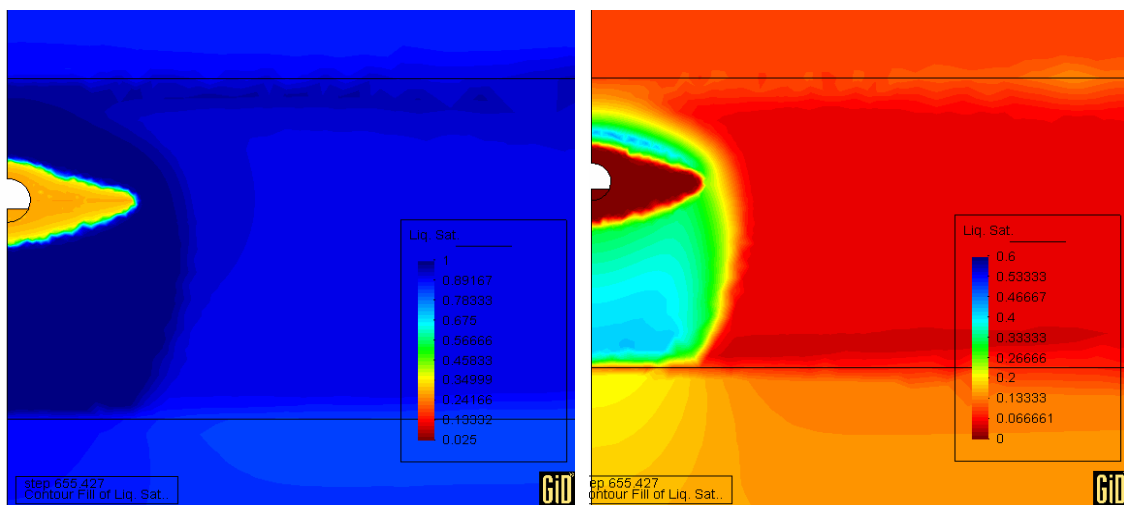


Figure 3.1-19. Degree of saturation distribution at 2 years of heating. Matrix on the left and fracture on the right

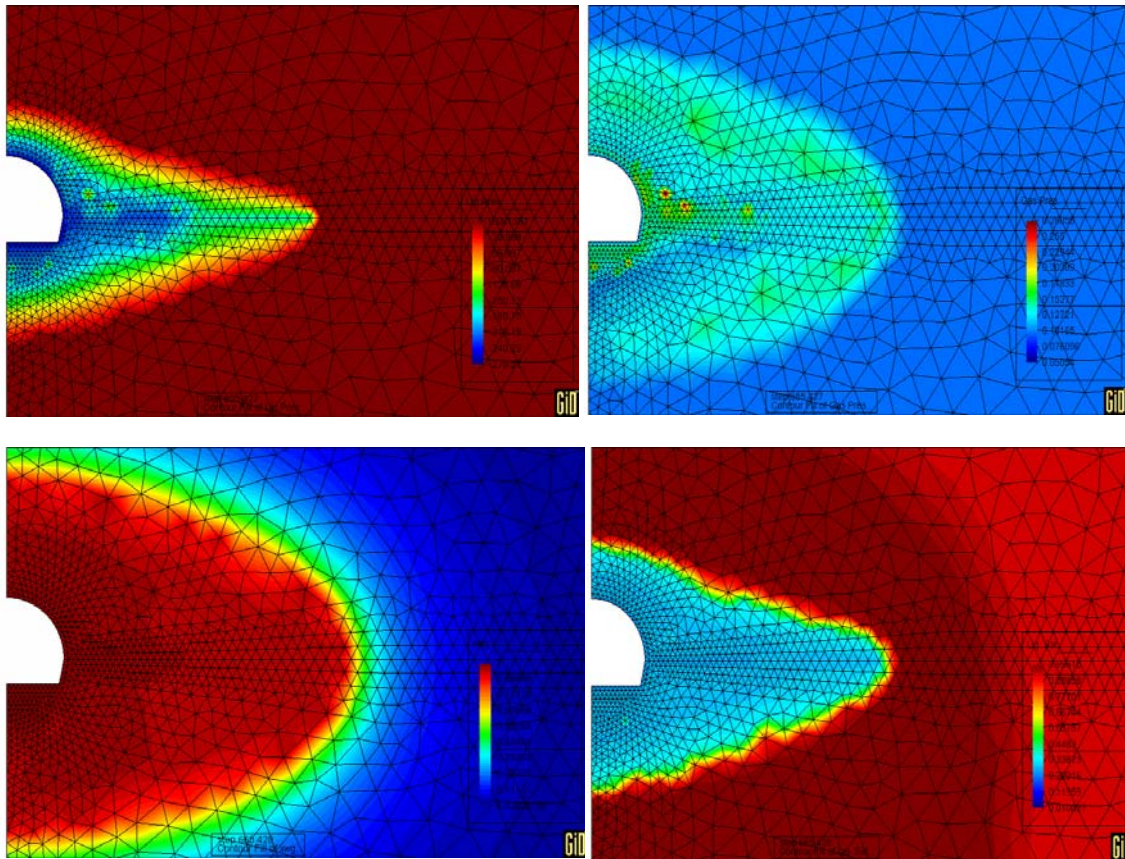


Figure 3.1-20. Hydraulic variables at 2 years. Liquid pressure (above left), gas pressure (above right), vapour mass fraction (below left) and liquid saturation (below right).

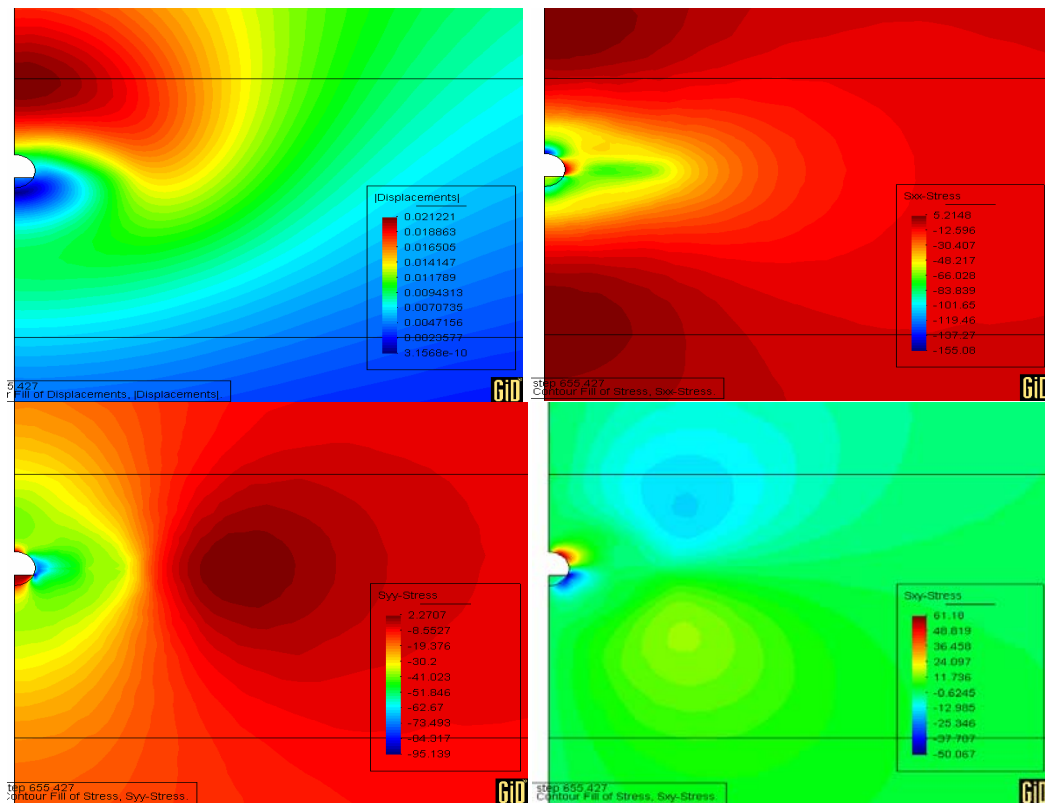


Figure 3.1-21 Mechanical variables at 2 years. Displacements (above left), horizontal stresses (above right), vertical stress (below left) and shear stress (below right)

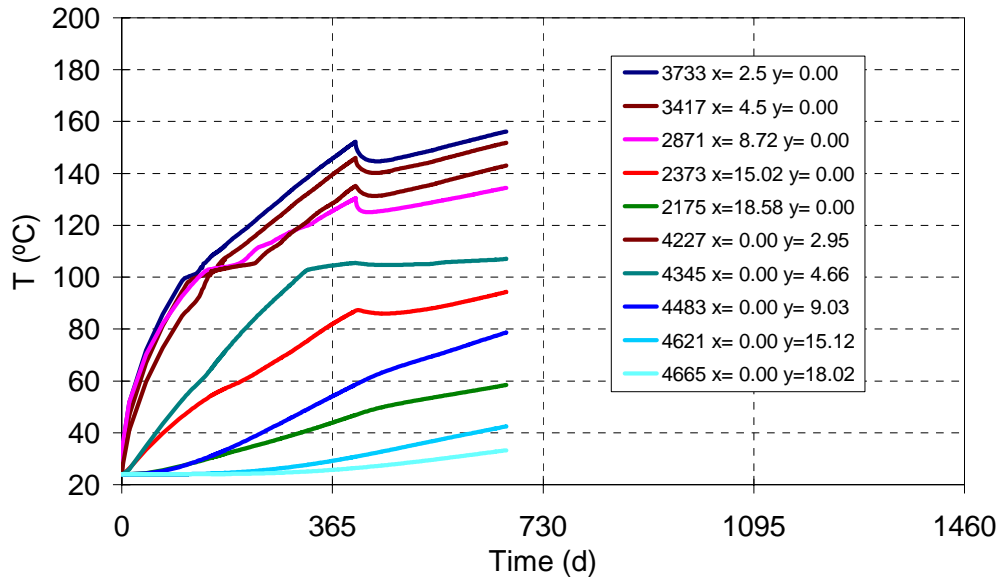


Figure 3.1-22. Evolution of temperature in matrix.

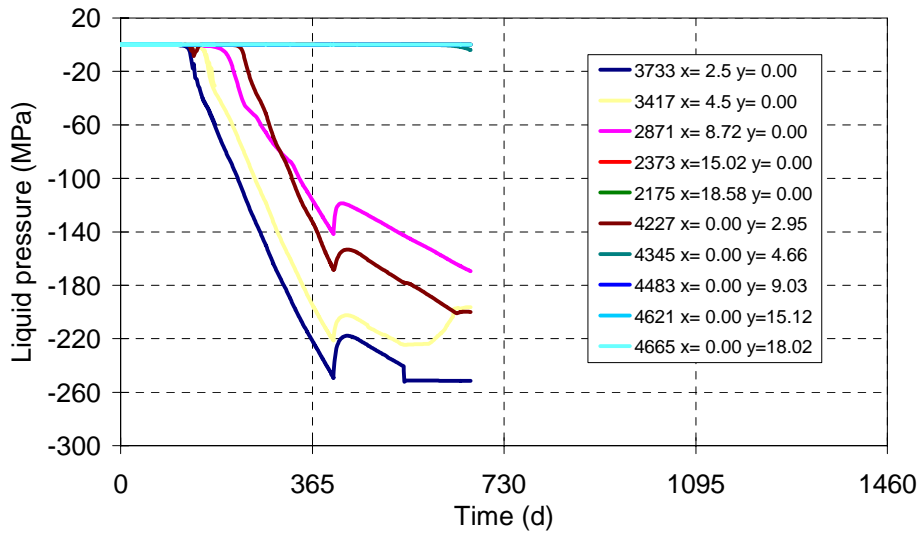


Figure 3.1-23 Liquid pressure evolution in matrix

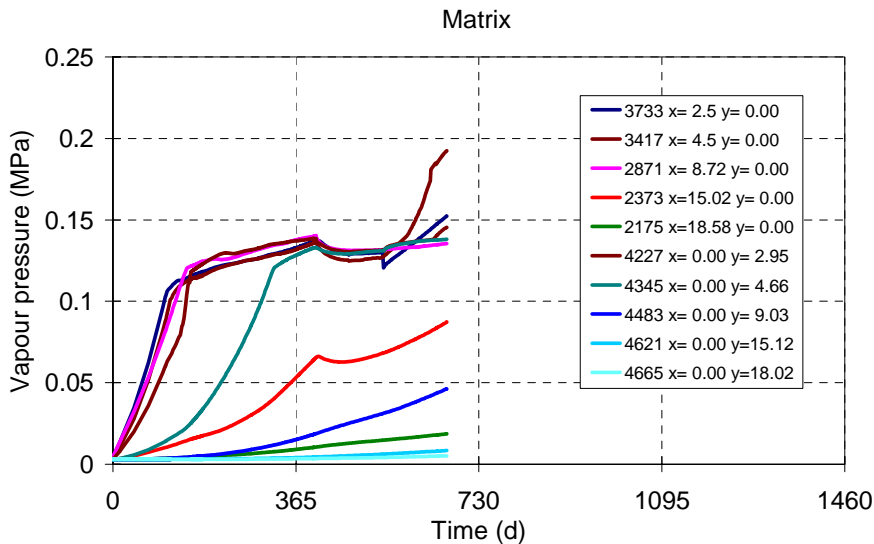


Figure 3.1-24. Vapour pressure evolution in matrix

decreases up to 0.25, which implies very high capillary pressures. These high capillary pressures are responsible, via psychrometric law, of maintaining the vapour pressure at atmospheric pressure. Otherwise, the vapor pressure at temperatures higher than 100°C is higher than atmospheric. The use of psychrometric law is not clear when the medium has been dried up strongly, with a sharp heating and capillary pressure increasing (liquid pressure decreases) up to values above 100 MPa, that are questionable. This probably requires a change in the state variable (for instance relative humidity or degree of saturation instead of liquid pressure).

### 3.1.5.2 Results for ND and MD cases

Since vapour mass fraction seems to reach a maximum value in the dry zone, it is possible that the diffusion of vapor play an important role in this problem. It is clear that vapor flows by advection and by diffusion/dispersion. Advection is very efficient due to the high permeability of the fractures. However, diffusion of vapor is also a very efficient transport term due to the high diffusivity of vapour in air. Therefore a second case that considers very efficient diffusion is further considered.

Vapour diffusion enhancement is considered. An enhancement coefficient, is taken into account in the vapour diffusion law:

$$\mathbf{i} = -\tau \varpi (\phi S_g) \rho_g D(T, P_g) \mathbf{I} \nabla \omega_g^w \quad (3.1-1)$$

where  $(\phi S_g)$  is the available area for diffusion,  $\varpi$  is a enhancement factor and  $\tau$  is a tortuosity factor, respectively.

The enhancement factor can be explained by different processes. For instance, the meniscus are short-cuts, or the temperature gradients are locally higher than the ones that are used in the averaged approach. The enhancement factor equal to  $1/S_g$  permits enhanced vapor diffusion in high saturation zones, and the vapor mass fraction gradients are less pronounced. A vapor diffusion more efficient implies that the liquid pressure decreases more rapidly because the vapor pressure is controlled by liquid pressure through psychrometric law.

The case that has been described above is referred here as ND (No Diffusion) because molecular diffusion of vapor was very low (tortuosity coefficient equal to 0.05). In contrast the new case is referred as MD (Maximum Diffusion) because the tortuosity is set to 1 and the enhancement factor has been included. A new FE mesh has been considered for the MD case with 6508 nodes and 15973 elements. Figure 3.1-25 shows this mesh and the zoom of centre part.

Figures 3.1-26 and 3.1-27 show a comparison between the two cases ND (already described above) and MD for degree of saturation in matrix and fracture at 1 year heating, respectively, and figures 3.1-28, 3.1-29 show the also degree of saturation but for 2 years of heating. From these plots, it can be seen that the dried zone is rather similar, but somewhat larger in the MD case. In contrast, the wetted zone, especially below the drift shows more development in the ND case than in the MD case. For the fracture, the maximum saturation reaches 0.6 while for the MD it hardly reaches 0.3. This wetted zone extends downwards for the ND case reaching practically the lower formation while in the MD case it is much smaller.

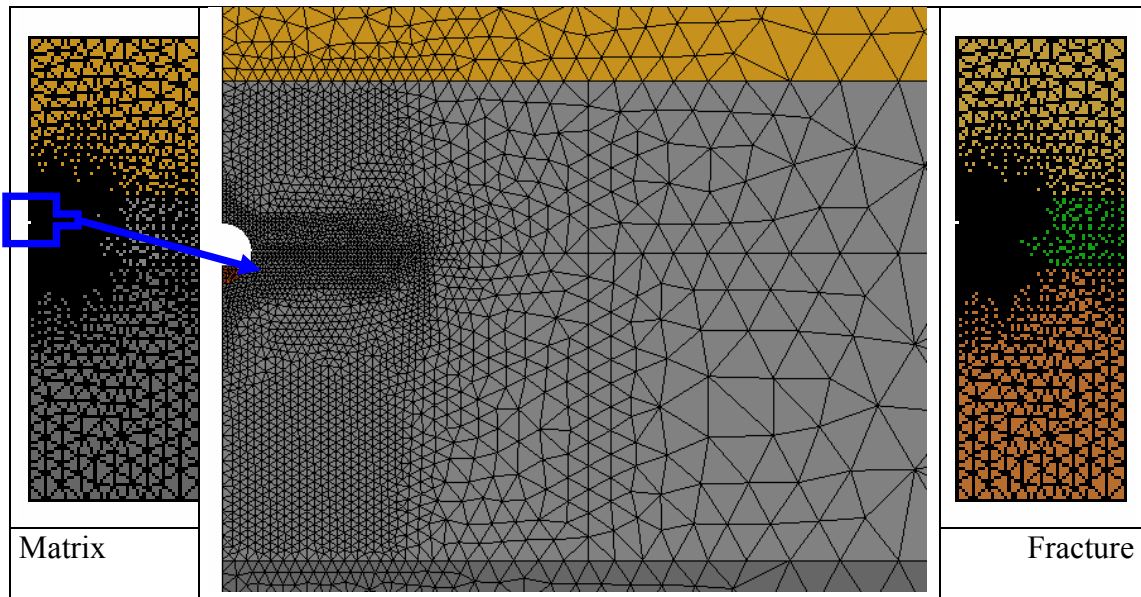


Figure 3.1-25. Finite element mesh used for the MD case

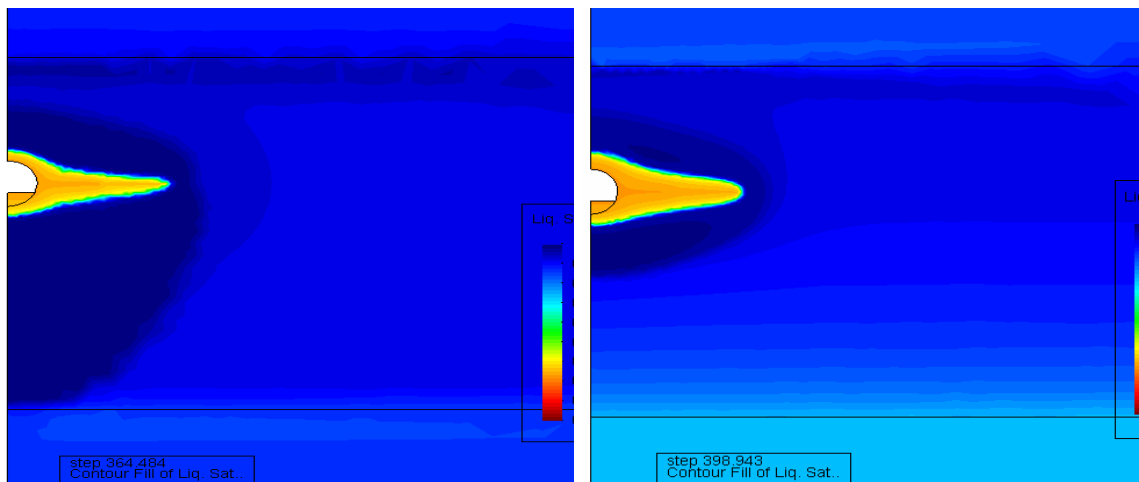


Figure 3.1-26. Matrix degree of saturation at 1 year. ND case on the left and MD case on the right

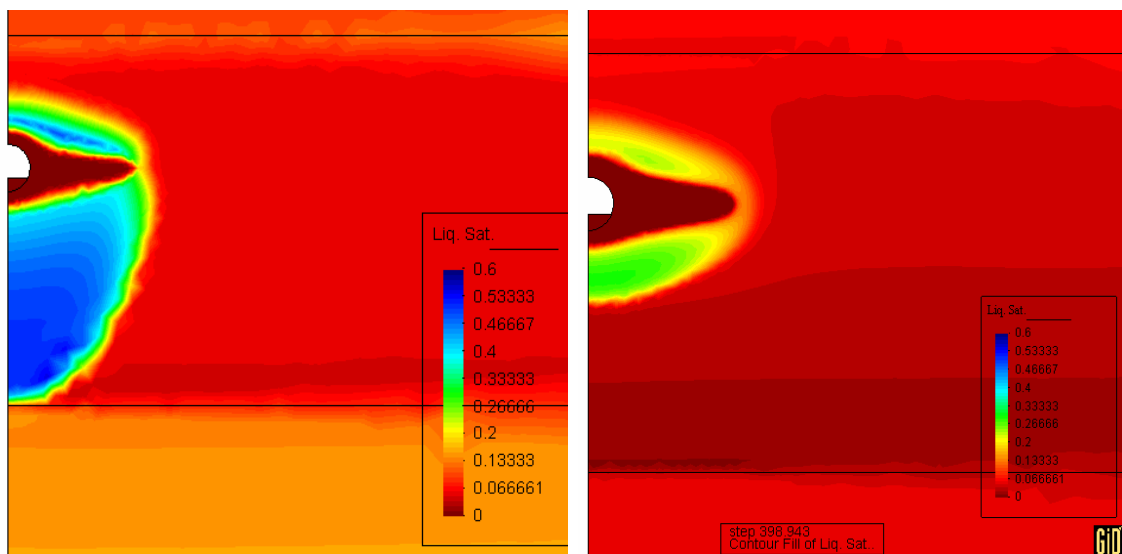


Figure 3.1-27. Fracture degree of saturation at 1 year, ND case on the left and MD case on the right.

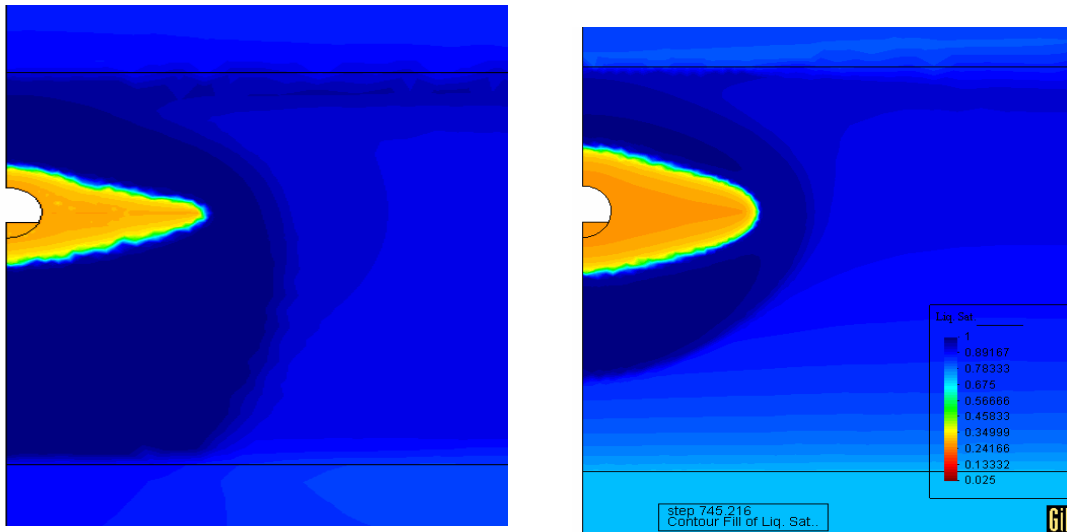


Figure 3.1-28. Matrix degree of saturation at 2 year. ND case on the left and MD case on the right.

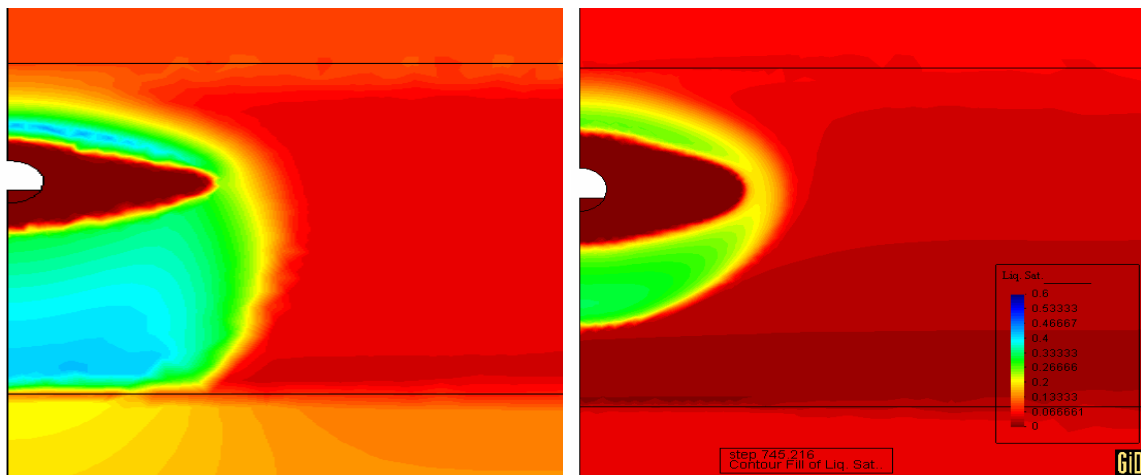


Figure 3.1-29. Fracture degree of saturation at 2 years. ND case on the left and MD case on the right.

### 3.1.5.3 Results for MD case at 4 years

Figure 3.1-30 shows for the MD case that at 4 years, the development of the wetted zone below the canister is larger and comparable to the one obtained for 1 or 2 years for the case ND.

Figures 3.1-31 and 3.1-32 show liquid and gas fluxes in the matrix and in the fracture for the MD case. It can be seen that liquid fluxes are important in both, matrix and fracture, while gas fluxes are only important for the fracture. Liquid flow is not important in the dried zone. Gas flow towards the drift and towards the heaters is motivated by the boundary condition of constant gas pressure in these boundaries.

Figures 3.1-33, 3.1-34, 3.1-35, 3.1-36, 3.1-37, and 3.1-38 show respectively the temperature, liquid pressure, vapour pressure, vapour mass fraction, degree of saturation for matrix and degree of saturation for fracture. Temperature evolution shows the effect of evaporation in points that are heated slowly. Liquid pressure shows that drying implies a large decrease to negative values with low physical meaning, except that this liquid pressure, once introduced in psychrometric law gives a relative humidity that is used for calculation of vapour pressure and vapour mass fraction. The physical meaning

is recovered. Therefore, such low liquid pressures may be considered only intermediate variables and impossible to measure directly.

It can be seen that vapour pressure is much more realistic (reaches atmospheric pressure but not much higher and remain more stable) for the MD analysis (Figure 3.1-35) than for the ND analysis (Figure 3.1-24).

Only for degree of saturation it is relevant to differentiate the matrix and the fracture. It is relevant to see the evolution of degree of saturation in points that undergo wetting and in points that undergo drying. After the drying front passes, degree of saturation in the matrix tends to a value in the range of 0.2 to 0.3 while the fracture reaches values practically zero. From these plots, it can be stated that steady state regime is not reached.

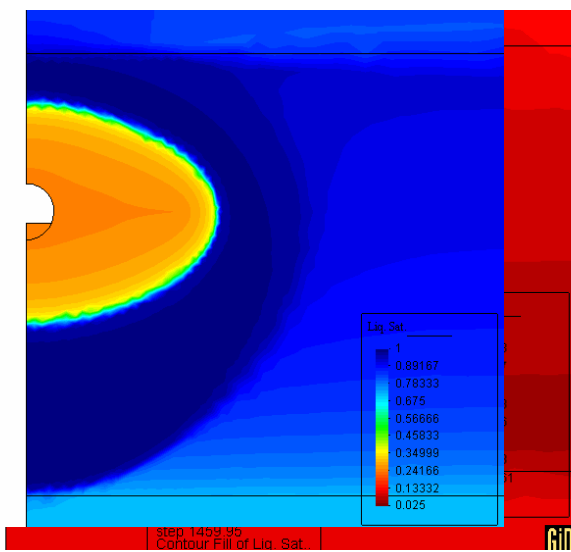


Figure 3.1-30. Matrix and Fracture degree of saturation at 4 years for case MD.

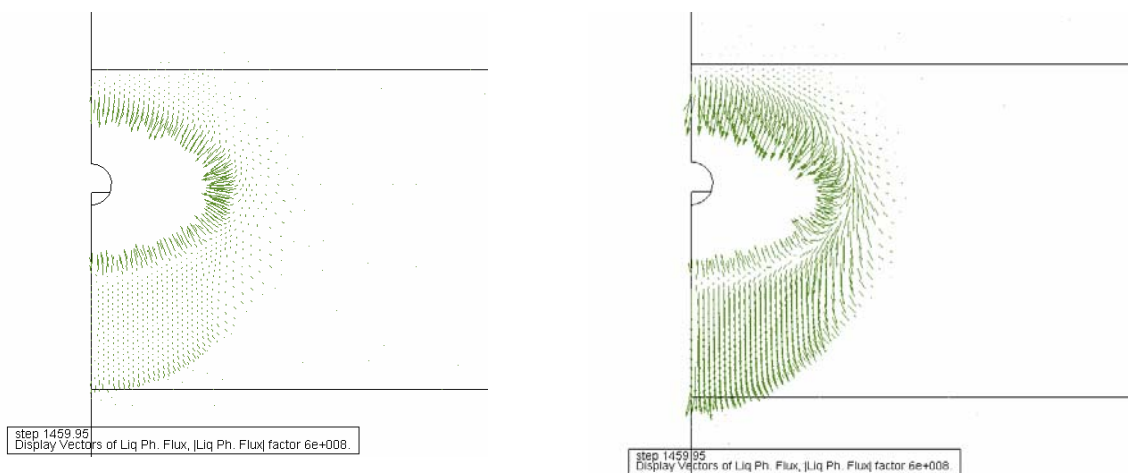


Figure 3.1-31. Matrix and Fracture liquid fluxes at 4 years for case MD

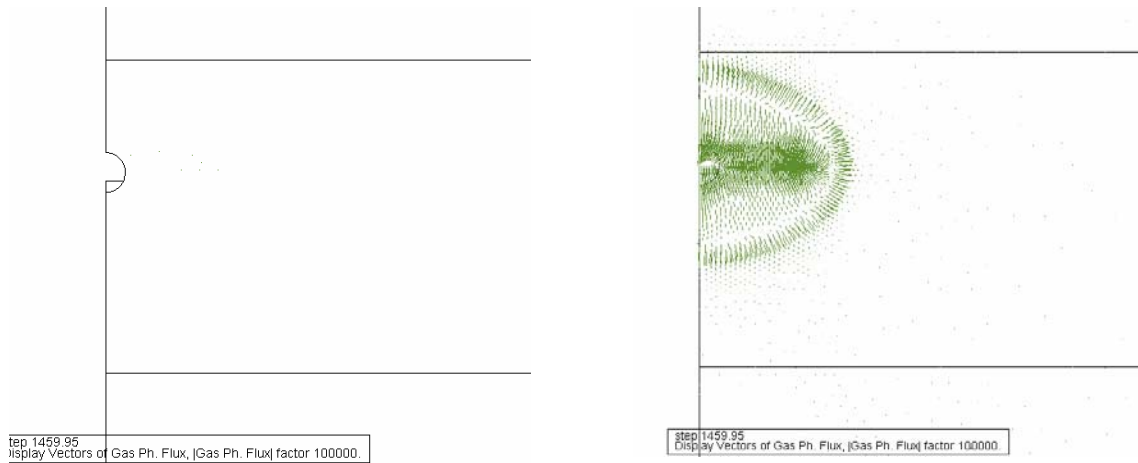


Figure 3.1-32. Matrix and Fracture gas fluxes at 4 years for case MD

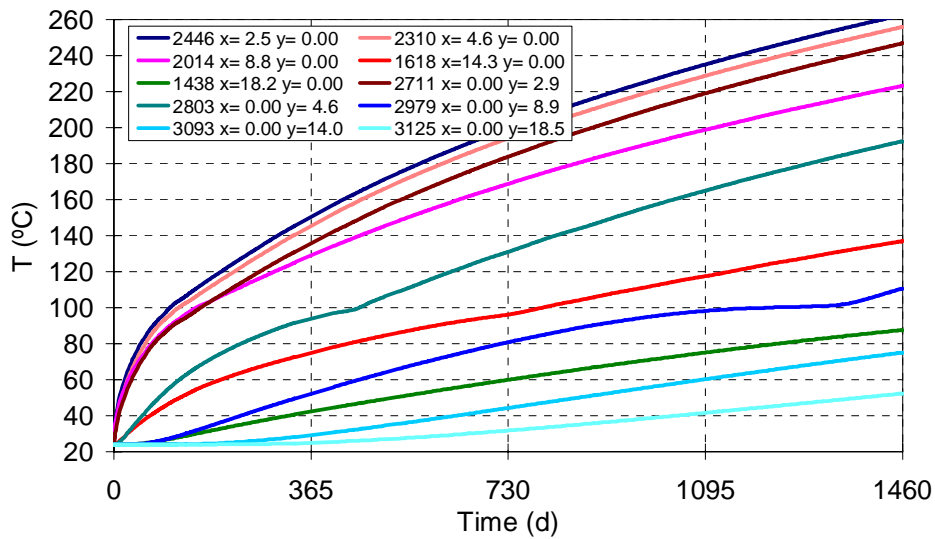


Figure 3.1-33. Temperature evolution at different points for case MD

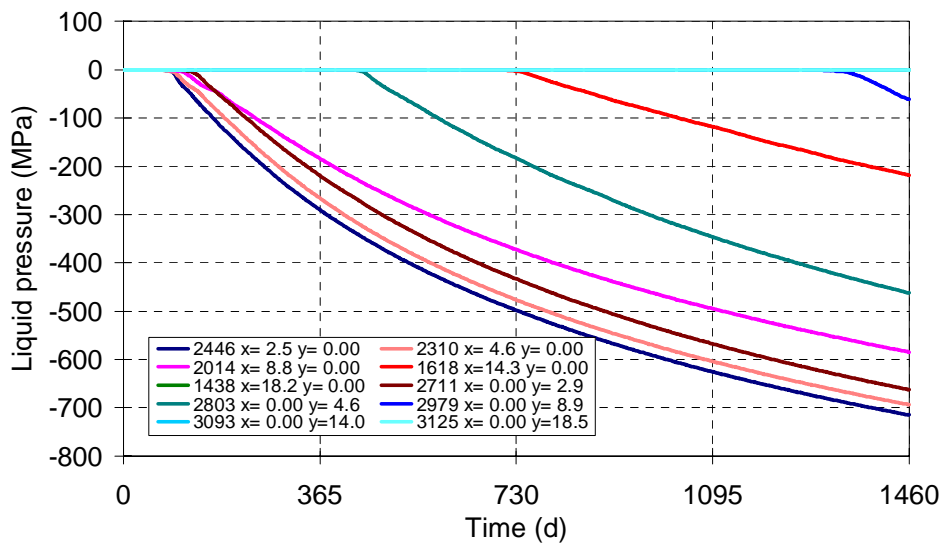


Figure 3.1-34. Liquid pressure for case MD

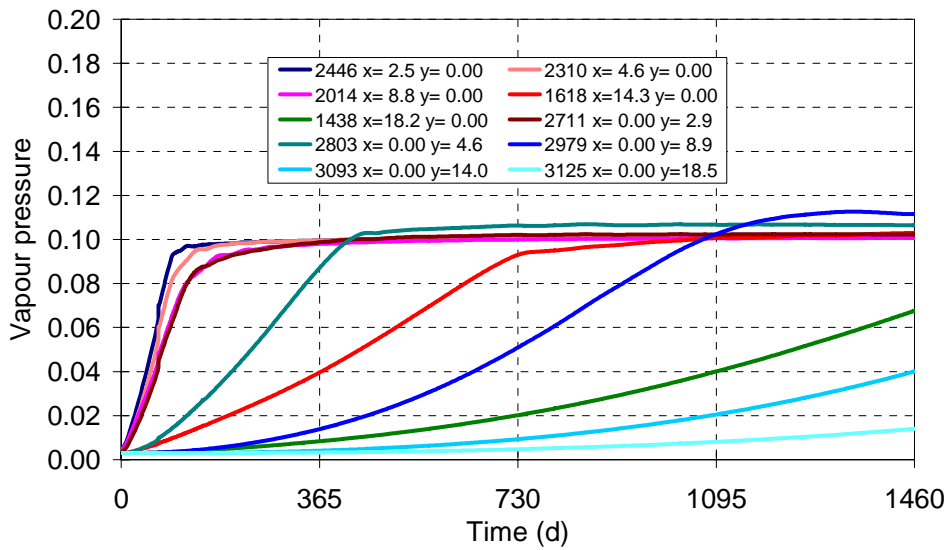


Figure 3.1-35. Mass fraction of vapour for the case MD

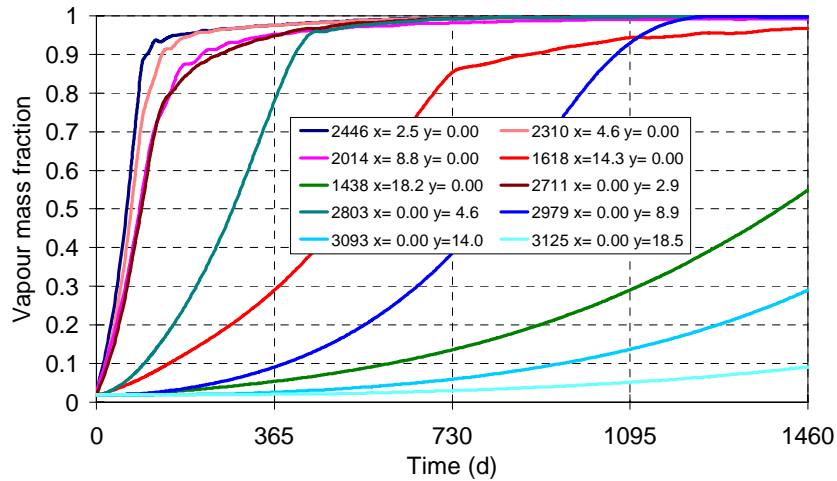


Figure 3.1-36. Mass fraction of vapour for the case MD

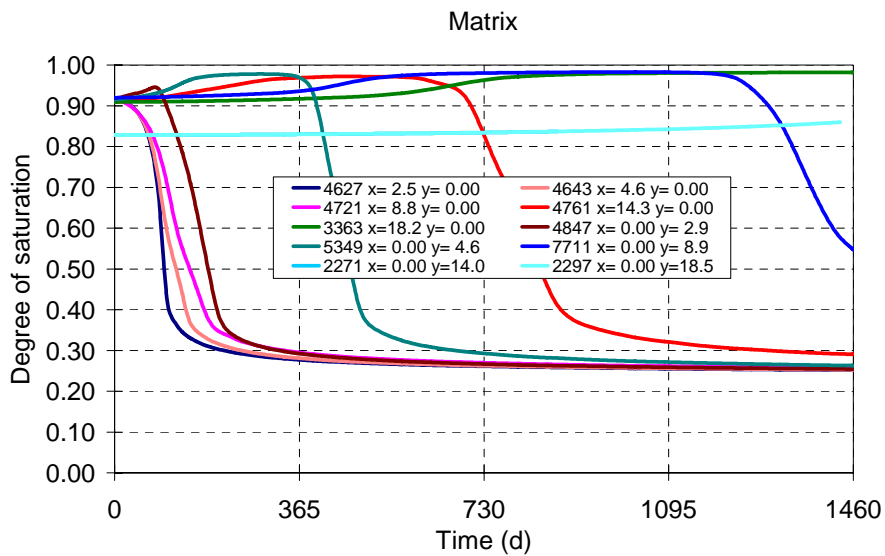


Figure 3.1-37. Matrix degree of saturation for the case MD

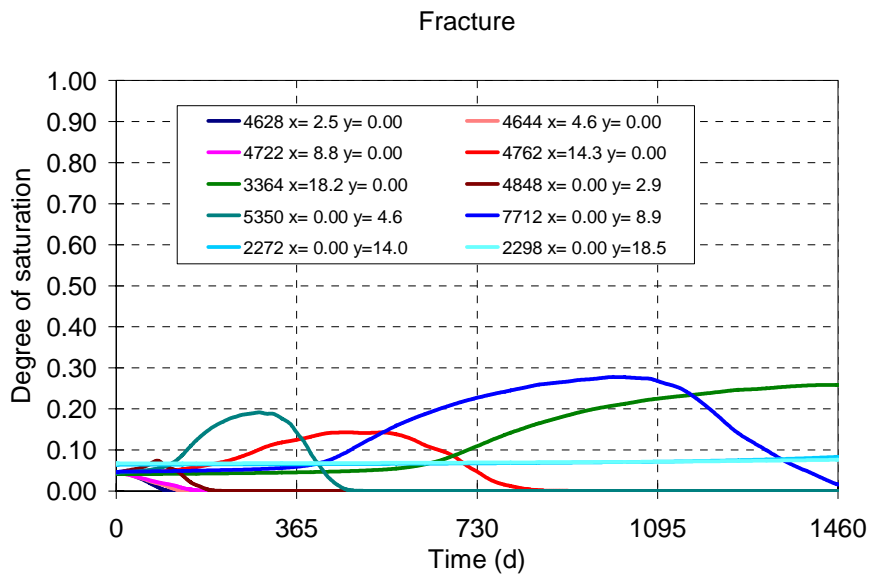


Figure 3.1-38. Fracture degree of saturation for the case MD

#### 3.1.5.4. Conclusions

The analyses presented here are the first attempt to use a finite element double structure approach to solve the THM problem simulating the DST test at Yucca Mountain. In this model, symmetry has been incorporated to allow mesh refinement. With this model the double structure formulation has been validated.

The tortuosity and enhancement coefficients are key parameters and vapour diffusion plays an important role as shown by the calculations. Liquid pressure controls vapour concentration via psychrometric law, vapour concentration tends to 1 in the dry zone, therefore air tends to disappear. Gas pressure gradients are not sufficient to dissipate vapour concentration if vapour diffusion is small.

On the other hand, liquid flow is driven by gravity, but this effect is more evident when vapour diffusion is smaller. Also the phase change signature is more evident when vapour diffusion is small.

## 3.2 NRC research team's TH modeling

The NRC research team's TH modeling of the DST for DECOVALEX III Task 2A is documented in this Section 3.2. The NRC team's initial predictive modeling was described in the Task 2A Interim Report prepared in February 2002. The NRC team later performed further refined modeling including comparative analyses with measurements and submitted its contribution for the Task 2A Final report in October 2002. This Section 3.2 of the present Task 2A Final Report is a composite, subsuming the NRC team's TH modeling and analyses relevant to Task 2A of DECOVALEX III project.

### 3.2.1 Introduction

The NRC research team modeled the thermal-hydrologic (TH) response of the DST employing the numerical modeling code MULTIFLO (Lichtner et al 2000). MULTIFLO is a general purpose code for modeling mass and energy transport processes in multiphase, non-isothermal systems with chemical reactions and reversible and irreversible phase changes in solids, liquids, and gases. The code consists of two sequentially coupled sub-modules: Mass and Energy Transport (METRA) and General Electromagnetic Migration (GEM). Only the transport of air, water, and heat in the DST was simulated for the Task 2A exercise using the METRA sub-module and reported in the Task 2A Interim report of February 2002. For subsequent refinement modeling MULTIFLO Version 1.5.1 (Painter et al 2001) was used to perform the simulations. Conceptual models for dual continua and the active fracture model (Liu, et al., 1998) were also evaluated. Temperatures measured during the 4-year heating phase of the Drift-Scale Heater Test were used as the basis for the evaluations.

### 3.2.2 Mathematical setting

In the MULTIFLO code METRA solves mass balance equations for water and air and an energy balance equation. Additional descriptions of flux terms between the matrix and fracture continua and of the active fracture model have been added here because of their importance in the analysis of the DST.

METRA represents multiphase flow through three dimensions, although zero, one, or two dimensions are also possible. Single-phase (i.e., all liquid or all gas) or two-phase systems can be simulated. The equation of state for water in METRA allows temperatures in the 1 to 800°C range and pressures below 165 bars. A description of the mathematical basis for METRA is presented below. A discussion of the balance equations is followed by the constitutive equations and the dual continuum model formulation.

#### 3.2.2.1 Conservation equations

The conservation equation for the water component (w) is given by

$$\frac{\partial}{\partial t} \left[ \phi \left( s_l n_l X_w^l + s_g n_g X_w^g \right) \right] + \nabla \cdot \left( q_l n_l X_w^l + q_g n_g X_w^g - D_g^{\text{eff}} n_g \nabla X_w^g \right) = Q_w \quad (3.2-1)$$

and for the air component (a) by

$$\frac{\partial}{\partial t} \left[ \phi \left( s_l n_l X_a^l + s_g n_g X_a^g \right) \right] + \nabla \cdot \left( q_l n_l X_a^l + q_g n_g X_a^g - D_g^{\text{eff}} n_g \nabla X_a^g \right) = Q_a \quad (3.2-2)$$

with source terms  $Q_w$  and  $Q_a$ , and where  $\nabla$  denotes gradient and  $\phi$  is porosity. Subscripts and superscripts  $g$  and  $l$  denote the gas and liquid phases. In these equations, mass transport,  $q_l$  and  $q_g$ , is represented by Darcy's Law (as modified by the relative permeability for multiphase flow), which includes capillarity, gravity, and viscous forces

$$q_l = -\frac{kk_{rl}}{\mu_l} \nabla (P_l - \rho_l g z) \quad (3.2-3)$$

and

$$q_g = -\frac{kk_{rg}}{\mu_g} \nabla (P_g - \rho_g g z) \quad (3.2-4)$$

where  $k$  denotes permeability,  $k_{r,l,rg}$  the relative permeability,  $P_{l,g}$  the fluid pressure,  $\mu_{l,g}$  the viscosity with mass densities  $\rho_{l,g}$ ,  $g$  is the acceleration of gravity, and  $z$  is the vertical dimension. The densities of the liquid and gas phases based on a molar representation are represented by  $n_{l,g}$ . Gas mixture properties are calculated assuming the ideal gas law. Gas viscosity is calculated using the kinetic theory of gases (Hirschfelder, et al., 1954). The mole fractions  $X_w^{l,g}$  and  $X_a^{l,g}$  satisfy the relations

$$X_w^l + X_a^l = 1 \quad (3.2-5)$$

and

$$X_w^g + X_a^g = 1 \quad (3.2-6)$$

Diffusion of water in the aqueous phase is neglected. The liquid and gas pressures are related through the capillary pressure

$$P_l = P_g - P_c \quad (3.2-7)$$

where  $P_c$  is typically defined as effective saturation.

Mass transfer in the gas phase may be enhanced by binary gas diffusion. The effective binary gas diffusion coefficient is defined using temperature, pressure, and material properties by

$$D_g^{\text{eff}} = \omega \tau \varphi s_g D_g^o \frac{P_o}{P_g} \left[ \frac{T + T_o}{T_o} \right]^\theta \quad (3.2-8)$$

where  $D_g^o$ ,  $T_o$  and  $P_o$  denote reference binary gas diffusion, temperature, and pressure.  $\tau$  is tortuosity,  $\theta$  is an empirical constant, and  $\omega$  is an enhancement factor (Walton and Lichtner, 1995). The enhancement factor is usually considered inversely proportional to the gas saturation,  $s_g$ , which cancels from the expression for the effective gas diffusion coefficient.

Adding Eqs. (3.2-1) and (3.2-2) eliminates the diffusive terms providing the total mass balance equation for air and water as

$$\frac{\partial}{\partial t} [\varphi (s_l n_l + s_g n_g)] + \nabla \cdot (q_l n_l + q_g n_g) = Q_w + Q_a \quad (3.2-9)$$

Energy transfer is by convection and conduction. The energy balance equation, assuming thermodynamic equilibrium between rock and fluid, is given by

$$\begin{aligned} & \frac{\partial}{\partial t} \left[ \phi \left( s_l n_l U_l + s_g n_g U_g \right) \right] + \nabla \cdot \left( q_l n_l H_l + q_g n_g H_g \right) \\ & + \frac{\partial}{\partial t} \left[ (1-j) C_P^{\text{rock}} r_{\text{rock}} T \right] - \nabla \cdot \kappa \nabla T = Q_e \end{aligned} \quad (3.2-10)$$

where  $U_{l,g}$  denotes the total internal energy,  $H_{l,g}$  the total enthalpy of the designated fluid phase,  $C_p^{\text{rock}}$  the heat capacity,  $\kappa$  the thermal conductivity, and  $Q_e$  a source term. Heat produced by chemical reaction is not included in the present version of the code. Energy transfer by radiation is only included at a boundary.

Vapor-pressure lowering of water-phase behavior resulting from capillary forces is defined by Kelvin's equation

$$P_v = P_{\text{sat}}(T) e^{-P_c / n_l R T} \quad (3.2-11)$$

where  $P_v$  represents vapor pressure,  $P_{\text{sat}}$  the saturation pressure of pure water,  $T$  the absolute temperature, and  $R$  the gas constant. Note that the density of the liquid phase,  $n_l$ , is represented on a molar basis.

### 3.2.2.2 Model parameters

Spatially variable values for porosity, absolute rock permeability (variable in three spatial directions), tortuosity, thermal conductivity, and media characteristic curves for relative permeability and capillary pressure can be specified. Capillary saturation relations provided in METRA are van Genuchten (1980), linear, and Brooks-Corey (Brooks and Corey, 1966) functions.

Liquid-phase relative permeability,  $k_{rl}$ , is calculated using the Mualem relationship (Mualem, 1976)

$$k_{rl} = \sqrt{s_l^{\text{eff}}} \left\{ 1 - \left[ 1 - \left( s_l^{\text{eff}} \right)^{1/m} \right]^m \right\}^2 \quad (3.2-12)$$

where capillary pressure,  $P_c$ , is related to saturation by the van Genuchten relationship (van Genuchten, 1980)

$$s_l^{\text{eff}} = \left[ 1 + \left( \alpha |P_c| \right)^n \right]^{-m} \quad (3.2-13)$$

where effective liquid saturation,  $s_l^{\text{eff}}$ , is defined by

$$s_l^{\text{eff}} = \frac{s_l - s_l^r}{s_l^o - s_l^r} \quad (3.2-14)$$

and where  $r$  and  $o$  denote residual and maximum saturations. The symbols  $\alpha$  and  $m$  are the van Genuchten parameters.  $m$  is related to  $n$  in Eq. (3.2-13) by  $m = 11/n$ .

The gas-phase relative permeability,  $k_{rg}$ , is defined in terms of  $k_{rl}$

$$k_{rg} = 1 - k_{rl} \quad (3.2-15)$$

The Brooks-Corey functions for liquid- and gas-phase relative permeabilities are defined by (Brooks and Corey, 1966)

$$k_{rl} = s_*^4 \quad (3.2-16)$$

and

$$k_{rg} = (1 - s_*^2)(1 - s_*)^2 \quad (3.2-17)$$

where saturation,  $s_*$ , is defined by

$$s_* = \frac{s_l - s_l^r}{1 - s_l^r - s_g^r} \quad (3.2-18)$$

Note that for the Brooks-Corey functions,  $k_{rl} + k_{rg} \neq 1$ , except for  $s_* = 0$ .

The linear relations for liquid- and gas-phase relative permeabilities are defined

$$k_{rl} = s_{lin} \quad (3.2-19)$$

and

$$k_{rg} = 1 - k_{rl} \quad (3.2-20)$$

where saturation,  $s_{lin}$ , is defined by

$$s_{lin} = \frac{s_l - s_l^r}{1 - s_l^r} \quad (3.2-21)$$

The thermal conductivity is also defined as a function of saturation (Somerton, et al., 1974)

$$\kappa = \kappa_{dry} + \sqrt{s_l^{eff}} \left\{ \kappa_{sat} - \kappa_{dry} \right\} \quad (3.2-22)$$

where  $\kappa_{sat}$  and  $\kappa_{dry}$  are the thermal conductivities for fully saturated and dry conditions.

### 3.2.2.3 Formulation of the active fracture model

An active fracture model for unsaturated flow through fractured rocks proposed by Liu, et al. (1998) is based on a hypothesis that only a portion of connected fractures is active in conducting water. The hypothesis stipulates that (i) all connected fractures are active if the system is fully saturated, (ii) all fractures are inactive if the system is at

residual saturation, and (iii) the fraction of fractures that are active is related to water flux through the fractures. Liu, et al. (1998) proposed that the fraction of active fractures be a power function of effective water saturation in connected fractures. The liquid-phase relative permeability function defined in Eq. (3.2-12) is modified to

$$k_{rl} = (s_l^{\text{eff}})^{\frac{1+\gamma}{2}} \left\{ 1 - \left[ 1 - (s_l^{\text{eff}})^{\frac{1+\gamma}{2}} \right]^m \right\}^2 \quad (3.2-23)$$

where the van Genuchten relationship between effective saturation and capillary pressure in Eq. (3.2-13) is modified to

$$s_l^{\text{eff}} = \left[ 1 + \left( \alpha |P_c| \right)^{\frac{n}{1-\gamma}} \right]^{-m} \quad (3.2-24)$$

where  $\gamma$  is a positive constant depending on the properties of the fracture network. The gas-phase relative permeability function is defined by the Brooks-Corey function in Eq 3.2-7). Values for  $k_{rg}$ ,  $k_{rl}$ , and  $P_c$  for the active fracture model are linearly interpolated from specified values of saturation included as a look-up table in MULTIFLO code Version 1.5.1

#### 3.2.2.4 Formulation of the dual continuum model

The dual continuum model formulation as defined by MULTIFLO is conceptually equivalent to the dual permeability model formulation used in recent U.S. Department of Energy numerical simulations (CRWMS M&O, 2000). The dual continuum model and dual permeability model conceptualization provides separate continua for the matrix and the fractures. The dual continua are coupled throughout the model domain by transfer functions for heat and mass transfer between the fractures and matrix. Use of a dual continuum model increases the complexity of the numerical model used in the simulations, but offers the potential to realistically partition flow between matrix and fractures. The following is a description of key components to the dual continuum model incorporated in MULTIFLO and used in the numerical analyses of the Drift-Scale Heater Test.

One of the critical parameters in a dual continuum model-based formulation is the model block size. The fracture-matrix distances (in each dimension) are related, but not equivalent, to model block dimensions. The model block dimension,  $d$ , is the distance between the center of the matrix block and the center of the fracture defining the edge of the model block. For the case where the element is a cube,  $d = l/2 + \delta/2$ , where  $l$  is the length of the matrix block, and  $\delta$  is the fracture aperture. Fracture aperture is calculated using model block size, matrix block size, and fracture porosity. Model block size directly affects two model properties: (i) the interfacial area between the matrix and fracture continua in a dual continuum model and (ii) the gradients that drive heat and mass between the two continua. In particular, increasing model block size reduces the area available for heat and mass transfer between the matrix and fracture continua and increases the distance over which changes in pressure and temperature occur, thereby reducing their respective gradients.

The interfacial area between the two continua,  $A_{fm}$ , is defined using matrix block dimensions,  $l_i$ , where  $i = x, y$ , and  $z$ . For two dimensions, the interfacial area is defined by

$$A_{fm} = 2(1 - \varphi_f) \left[ \frac{1}{l_x} + \frac{1}{l_z} \right] \quad (3.2-25)$$

which, for a cubic block geometry in two dimensions (i.e.,  $l_x = l_z$ ), becomes

$$A_{fm} = 4 \left( \frac{1 - \varphi_f}{l} \right) \quad (3.2-26)$$

where  $\varphi_f$  is fracture porosity.

Mass flow across the matrix/fracture interface,  $Q_{l-mass}$ , is directionally dependent. When  $P_{lm} > P_{lf}$ , liquid flow from the matrix to the fracture continuum is defined by

$$Q_{l-mass} = \frac{A_{fm} A_{mod}}{\mu_l} k_{harmonic,l} k_{rl,m} \frac{P_{lf} - P_{lm}}{d} \quad (3.2-27)$$

where the  $m, f, l$ , and  $r$  subscripts denote matrix, fracture, liquid, and relative.

$A_{mod}$  is a modifier term included to allow a reduction, but not an increase, in the interfacial area between the matrix and fracture continua. The liquid-phase relative permeability function for fracture to matrix flow,  $k_{rl,f \rightarrow m}$ , need not be the same, thereby providing additional flexibility to the model.

The harmonic mean for liquid permeability is expressed as

$$k_{harmonic,l} = \frac{k_f k_m}{k_f + k_m} \quad (3.2-28)$$

The liquid-phase relative permeability function for fracture-to-matrix flow,  $k_{rl,f \rightarrow m}$ , need not be the same as for the fracture continuum,  $k_{rl,f}$ . This additional flexibility introduced in MULTIFLO Version 1.5.1 permits additional reduction in flow consistent with the active fracture model. This additional reduction only applies to liquid flow from fractures to matrix. Heat and gas flow and flow from matrix-to-fracture are not affected. Within the active fracture model,  $k_{rl,f \rightarrow m}$ , is approximated as

$$k_{rl,f \rightarrow m} \cong (S_l^{eff})^{1+\gamma} k_{rl,f} \quad (3.2-29)$$

For  $P_{lf} > P_{lm}$  liquid flow from the fracture to the matrix is defined by

$$Q_{l-mass} = \frac{A_{fm} A_{mod}}{\mu_l} k_{harmonic,l} k_{rl,f \rightarrow m} \frac{P_{lf} - P_{lm}}{d} \quad (3.2-30)$$

An analogous form of Eq. (2-27) defines mass flow of gas between the matrix and fracture continua.

$$Q_{g\text{-mass}} = \frac{A_{fm} A_{\text{mod}}}{\mu_g} k_{\text{harmonic},g} k_{rg} \frac{P_{gf} - P_{gm}}{d} \quad (3.2-31)$$

Note that mass flow of gas between the matrix and fracture continua is not directional, that is, the  $A_{\text{mod}}$  for matrix to fracture gas flow is equal to the  $A_{\text{mod}}$  for fracture to matrix gas flow.

Analogous to mass flow are expressions and relationships for heat flow. Heat flow across the matrix fracture interface is defined as

$$Q_{\text{heat}} = A_{fm} A_{\text{mod}} \kappa_{\text{arithmetic}} \frac{T_f - T_m}{d} \quad (3.2-32)$$

Note that heat transfer and mass transfer across the matrix/fracture interface are coupled processes, but each responds to its respective driving forces calculated for the same distance,  $d$ . Gradients that drive mass and heat transfer are decreased when the block dimensions are increased (i.e., the differences in pressure or temperature between the two continua remain the same for each model element while the distance over which the difference occurs increases with an increased block size, thereby reducing the gradients).

Either time-dependent Neumann (constant flux), Dirichlet (constant field variables), or mixed boundary conditions may be specified in MULTIFLO. Time-varying heat and mass sources and sinks may be designated at specified nodal locations. Time-varying boundary conditions, sources, or sinks are specified in tabular form and are linearly interpolated corresponding to the midpoint of the timestep.

### 3.2.3 Numerical solution

METRA is based on a fully implicit formulation using a variable substitution approach. Space discretization is based on a block-centered grid using an integral finite-volume difference scheme. This approach is suitable for a structured and unstructured grid with arbitrary interblock grid connectivity and any polygon block boundary. Flow through fractured media may be represented by the dual continuum model or using an equivalent continuum medium where the dual continuum is represented by an equivalent single continuum (Pruess and Narasimhan, 1985; Klavetter and Peters, 1986).

Three primary variables are required to describe a two-phase nonisothermal system consisting of two species, water and air. The chosen primary variables are listed in Table 3.2-1, where  $P_l$  is the liquid pressure for a pure liquid system and  $P_g$  the total gas pressure for a two-phase or pure gas-phase system.  $X_a$  denotes the mole fraction of air with partial pressure  $P_a$ ,  $s_g$  denotes gas saturation, and  $T$  denotes temperature. Note that gas saturation is related to liquid saturation by  $s_g + s_l = 1$ .

Three primary equations are solved by METRA: (i) total mass balance, (ii) air mass balance, and (iii) energy balance. The three equations are simultaneously solved for each grid block by the tridiagonal Thomas algorithm for one-dimensional systems and by the WATSOLV package (van der Kwaak, et al., 1995) for both two-dimensional and three-dimensional systems. The WATSOLV package is based on incomplete factorization accelerated by employing generalized minimum residual or biconjugate gradient stabilized procedures (van der Kwaak, et al., 1995).

Table 3.2-1. Choice of Primary Variable for Different Fluid States

Fluid State	Primary Variables
Single-phase liquid	$P_l, X_a, T$
Two phase	$P_g, P_a, s_g$
Single-phase gas	$P_g, P_a, T$

### 3.2.4 Drift Scale Test model

As shown schematically in Figure 3.2-1, the DST block is defined in plan by the Observation Drift (OD), the Connecting Drift (CD), and the Heated Drift (HD). The 5-m diameter, 47.5-m long HD is closed at the east end by a thermal bulkhead. Approximately 12.5 m of the west end of the heated drift is lined with cast-in-place concrete ground support. The HD was excavated as 5.6-m diameter along last 12.5-m length to allow for the concrete ground support. Concrete inverts with a thickness of 1.2 m at the HD center line were placed along the entire floor of the heated drift to provide a flat surface. Heat sources in the DST consist of 9 canister heaters, placed end to end on the floor of the HD, and 50 wing heaters (25 on either side), emplaced in horizontal boreholes drilled into the sidewalls of the HD approximately 0.25 m below the springline. The wing heaters are spaced 1.83 m apart. Each wing heater has 2 segments, both 5-m long, with a larger power output from the outer segment. The inner wing heater segment is separated from the HD wall by a space of 1.5 m.

#### 3.2.4.1 Drift Scale Test model domain

The DST was numerically simulated with a three-dimensional model. The three-dimensional model was assembled with a series of fourteen vertical two-dimensional transverse cross sections: seven intersect the drift, and seven are located beyond the terminus of the drift. Two planes of vertical symmetry were assumed: one aligning with the axis of the HD, and one intersecting the axis of the HD mid-distance between the bulkhead and the terminus of the HD. Therefore, essentially one-fourth of the Drift-Scale Heater Test was included in the numerical model. The modeled area extends 200 m vertically with the center of the heated drift placed at the center of the numerical model and 100 m horizontally from the drift center. The boundaries for this model were extended from distances reasonably needed for thermohydrological simulations to for allow temperature predictions needed at greater distances required by thermal-mechanical simulations.

The two-dimensional slice of the grid with 1,123 nodes in the planes intersecting the drift is illustrated in Figure 3.2-2. A closeup of the two-dimensional slice of the grid in the vicinity of the heated drift is shown in Figure 3.2-3, which illustrates the finer mesh resolution in areas expected to experience large temperature, saturation, and pressure gradients. Planes beyond the terminus of the drift had an additional 52 nodes to fill in the drift cavity for a total of 1,175 nodes (not shown). The full three-dimensional model, therefore, has 16,068 nodes in each continuum for a total of 32,136 nodes. The model domain is modeled as three hydrostratigraphic units, the Topopah Spring upper lithophysal (tsw33), Topopah Spring middle nonlithophysal (tsw34), and Topopah Spring lower lithophysal (tsw35) of the Topopah Spring welded unit.

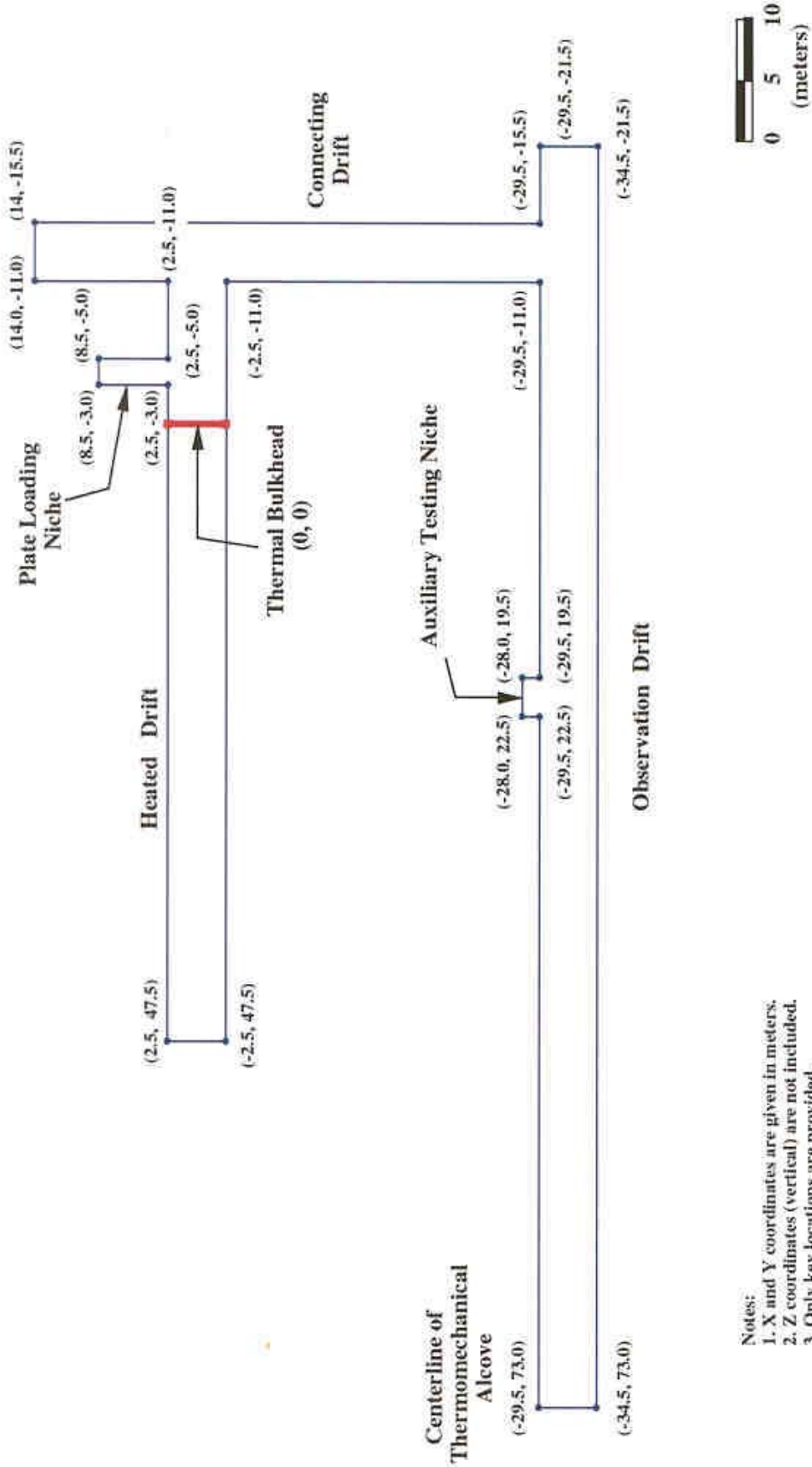
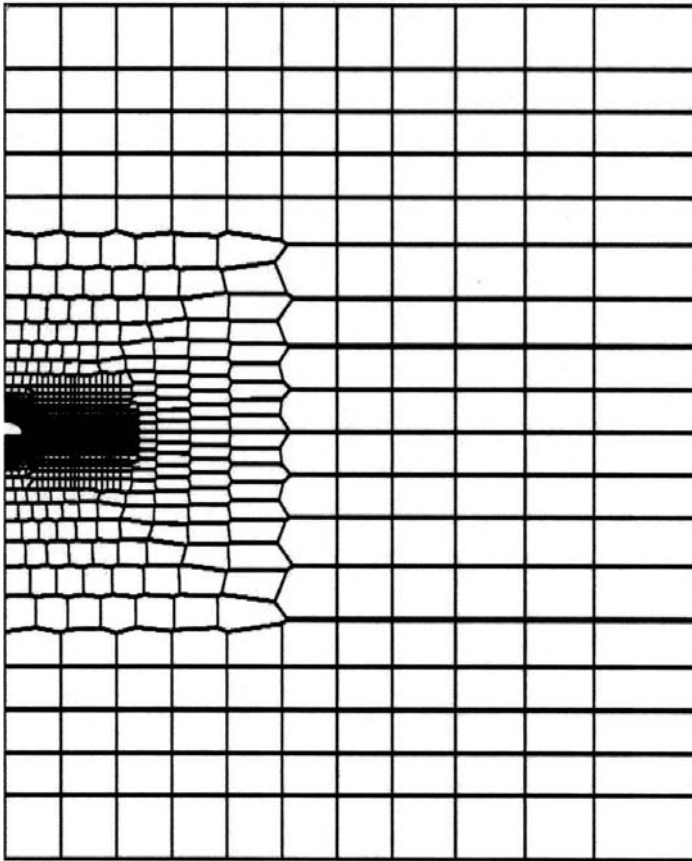
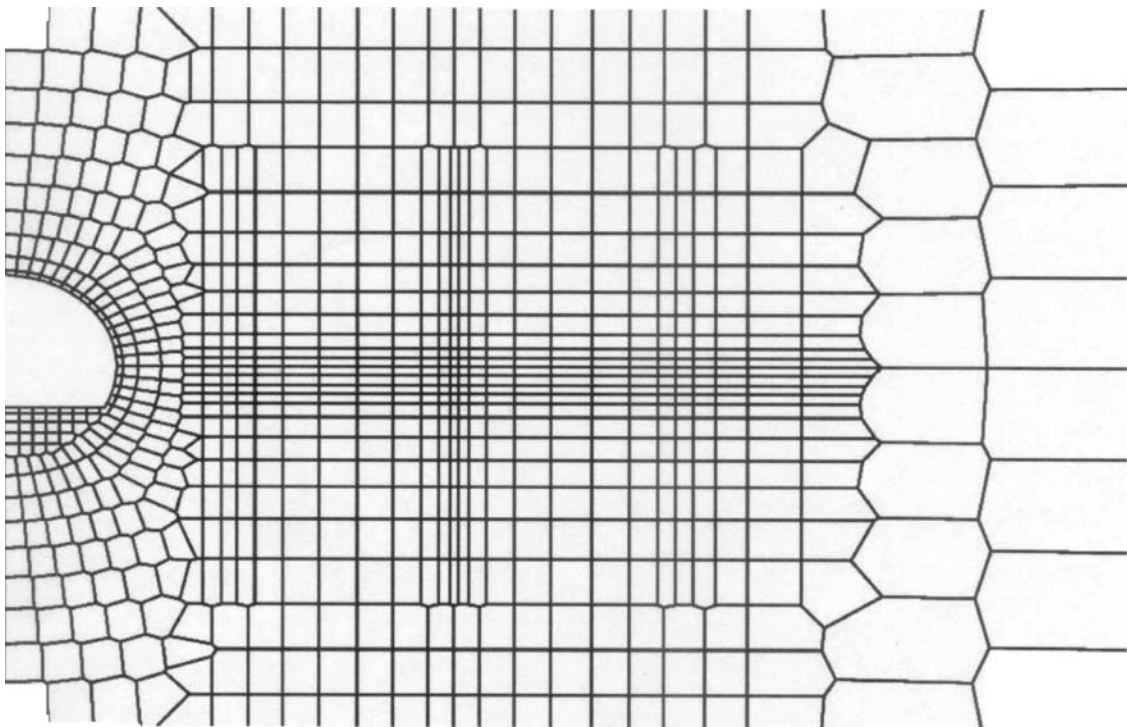


Figure 3.2-1. Plan View Schematic of the Drifts Defining the Drift Scale Test Block



*Figure 3.2-2. Vertically Oriented Grid Discretization of the Drift Scale Test. The Illustrated Section is for the Modeled Block with the Drift*



*Figure 3.2-3. Close-up of the Grid Discretization Proximal to the Heated Drift and Wing Heaters. NOTE: The Illustrated Section is for the Modeled Block with the Drift.*

### 3.2.4.2 Model property assignment

Base case property values for tsw33, tsw34, and tsw35 were taken from CRWMS M&O (2001). These values are summarized in Tables 3.2-2 through 3.2-4. Fracture permeability is expressed in terms of intrinsic values. Bulk fracture permeability can be calculated by dividing the intrinsic values by the fracture porosity. A block size of 0.40 m was uniformly assigned to the entire model domain for the base case. The wing heaters had the same hydraulic properties as the adjoining rock (tsw34) in the base case but had modified hydraulic properties in two simulations to simulate the effect of the wing heater borehole.

Table 3.2-2. Matrix Hydraulic Properties

Unit	Porosity	Permeability (m <sup>2</sup> )	s <sub>r</sub>	α (Pa <sup>-1</sup> )	m
tsw33 (Ttpul)	0.154	3.08 x 10 <sup>-17</sup>	0.12	2.13 x 10 <sup>-5</sup>	0.298
tsw34 (Ttpmn)	0.110	4.07 x 10 <sup>-18</sup>	0.19	3.86 x 10 <sup>-6</sup>	0.291
tsw35 (Ttpll)	0.131	3.04 x 10 <sup>-17</sup>	0.12	6.44 x 10 <sup>-6</sup>	0.236

Table 3.2-3. Fracture Hydraulic Properties

Unit	Porosity	Permeability Vertical (m <sup>2</sup> )	Permeability Horizontal (m <sup>2</sup> )	s <sub>r</sub>	α (Pa <sup>-1</sup> )	m
tsw33 (Ttpul)	0.0066	5.50 x 10 <sup>-13</sup>	5.50 x 10 <sup>-13</sup>	0.01	1.46 x 10 <sup>-3</sup>	0.608
tsw34 (Ttpmn)	0.010	2.76 x 10 <sup>-13</sup>	2.76 x 10 <sup>-13</sup>	0.01	5.16 x 10 <sup>-4</sup>	0.608
tsw35 (Ttpll)	0.011	1.29 x 10 <sup>-12</sup>	1.29 x 10 <sup>-12</sup>	0.01	7.39 x 10 <sup>-3</sup>	0.611

Table 3.2-4. Thermal and Physical Properties

Unit	Thermal Conductivity BDry (W/m-K)	Thermal Conductivity BWet (W/m-K)	Rock-Specific Heat (J/kg-K)	Rock Density (kg/m <sup>3</sup> )	F <sub>ma</sub> (m <sup>2</sup> /m <sup>3</sup> )
tsw33 (Ttpul)	0.79	1.68	882	2510	5 x 10 <sup>-4</sup>
tsw34 (Ttpmn) <sup>1</sup>	1.56	2.33	948	2530	1.23 x 10 <sup>-3</sup>
tsw35 (Ttpll)	1.20	2.02	900	2540	5 x 10 <sup>-4</sup>

### 3.2.4.3 Boundary and initial conditions

The vertical boundaries of the model were specified as adiabatic with no fluid flow. The top boundary for the basecase was prescribed as a specified flux. The bottom boundary was prescribed as a drainage boundary with specified pressure, temperature, and saturation. The mixed boundary condition at the top allows gas and heat transport in or out of the model while maintaining pressure and temperature as specified. Water flux at the top boundary was introduced into the fracture continuum. The heated drift was not explicitly included in the model; instead, the heated drift wall was modeled as a Dirichlet boundary (constant pressure), and heat from the floor canisters was applied directly to the heated drift walls. The effect of the pressure Dirichlet boundary at the heater drift wall allows the removal of sensible heat transported by water vapor. Heat removal from the drift wall by either conduction or radiation is not explicitly included in the simulation. Heat loss through the drift wall by these two mechanisms was implicitly incorporated by reducing the heat load imposed at the drift wall by variable amounts (i.e., 20 percent) to evaluate this source of heat loss.

The temperature was specified as 22°C and 24°C at the top and bottom boundaries for a geothermal gradient of 0.01°C/m. A static gas pressure difference of 1,920 Pa between the top and bottom boundaries was specified to impose a gas gradient consistent with ambient conditions. This pressure is equivalent to a 200-m tall column of air at standard pressure and temperature. Gas pressures of 88,920 Pa at the bottom and 87,000 Pa at the top establish a gas pressure at the Drift-Scale Heater Test horizon of slightly less than 88,000 Pa, consistent with observed gas pressures and gas pressure gradients (Bodvarsson and Bandurraga, 1997).

Sensitivity analyses conducted in a previous study evaluated how different property assignments and boundary and initial conditions affect the ambient matrix saturation before the Drift-Scale Heater Test (Green, et al., 2000, and 2001). Ambient saturation was determined by simulating flow in the absence of heat at the Drift-Scale Heater Test for sufficiently long periods of time that steady-state flow conditions were approximated. The steady-state simulations were run without the presence of the drift to avoid the shadow effects of the drift opening on ambient saturation. Steady-state flow conditions were usually approximated in about  $10^7$  years.

Ambient matrix saturation was selected as the key state variable to evaluate the appropriateness of the pretest (i.e., steady-state or ambient) conditions for the conceptual and numerical models used to simulate the Drift-Scale Heater Test. This selection was made because of the sensitivity of saturation to changes in model design and the ability to directly measure matrix saturation on core and grab samples collected at the site. A matrix saturation of 0.92 in the tsw34 (Topopah Spring middle nonlithophysal) was designated the target saturation. This target saturation is close to the value of 0.924 measured on samples collected at the Drift-Scale Heater Test (CRWMS M&O, 1997).

Simulations run to determine the steady-state conditions encountered a potential conflict when the most current property values were used in the simulation. In particular, simulations that included a block size of 0.40 m, infiltration rate of 3.0 mm/year, and the media property values documented in CRWMS M&O (2001) predicted steady-state saturations greater than 0.99, much greater than the documented ambient matrix saturations (i.e., 0.92). Sensitivity analysis results indicated that lower saturations can be achieved by either significantly decreasing infiltration {from 3.0 mm/year to approximately 0.07 mm/year or increasing the block size from 0.4 m to approximately 5.0 m. Although fracture mapping indicates a block size of 0.4 m, not all fractures are necessarily hydraulically active. It is not clear how to accurately

incorporate into models the difference between mapped fractures and hydraulically active fractures. Increasing block size and incorporating an active fracture conceptualization into the model are two possible approaches. The ramifications of increased block size are not fully understood and are being evaluated.

#### 3.2.4.4 Previous Drift Scale Test modeling results

Analyses reported in this document have built on previous studies performed at the Center for Nuclear Waste Regulatory Analyses. Summaries of these studies are included here.

Model parameters evaluated in a previous study (Green, et al., 2000) were infiltration rate, block size, liquid flow from matrix to fracture interaction area, the upper boundary condition, and fracture permeability. These parameters were selected for investigation because sensitivity analysis results indicated that changes in these property values have a significant effect on predicted matrix saturation. Specific changes to model parameters evaluated were

- Surface boundary changed from Neumann to mixed with specified flux and constant temperature and pressure
- Block size varied from 0.25 m to 20 m; infiltration flux at the surface varied from 0.00036 mm/year to 3.6 mm/year
- Anisotropic fracture permeability decreased by three orders of magnitude in the x-, y-, and z-directions from the basecase values

As demonstrated in the investigation by Green, et al. (2000), changes in values assigned to fracture permeability had negligible effects on ambient matrix saturation but did affect temperatures and saturations predicted for the heating phase of the Drift-Scale Heater Test. Changes in block size and infiltration rate proved to have a significant effect on ambient matrix saturation, as illustrated in Figure 3.2-4 (a through d). An increase in block size decreased the ambient steady-state saturation. This effect was more pronounced for a smaller value of the fracture-matrix area modification factor of  $1.23 \times 10^{-4}$  in Figure 3.2-4 (a and b)] than for a larger value of  $A_{\text{mod}}^*$  of 1.0 in Figure 3.2-4 (c and d) for both high (3.6 mm/year) and low (0.072 mm/year) infiltrations. (The  $A_{\text{mod}}^*$  nomenclature is not used in MULTIFLO code Version 1.5.1.) In fact, it is possible to have a reasonable ambient steady-state saturation of 0.92 with an infiltration rate of 3.6 mm/year if block size is increased to approximately 6 m to 7 m (Figure 3.2-4a).

Additional numerical simulations were performed (Green, et al., 2001) to evaluate the effects of changes to fracture permeability, thermal conductivity, the active fracture model, and the matrix/fracture area modification factor had on predicted temperatures and saturations. The analyses evaluated the following effects:

- Intrinsic fracture permeability was reduced by factors of 10, 100, and 1,000.
- Thermal conductivity was increased and decreased by 20 percent.
- Steady-state and heated simulations were performed to evaluate the effects of the active fracture model (Liu, et al., 1998).
- The matrix/fracture area modification factor,  $A_{\text{mod}}^*$ , was varied from 1.0 to  $1.0 \times 10^{-4}$ .

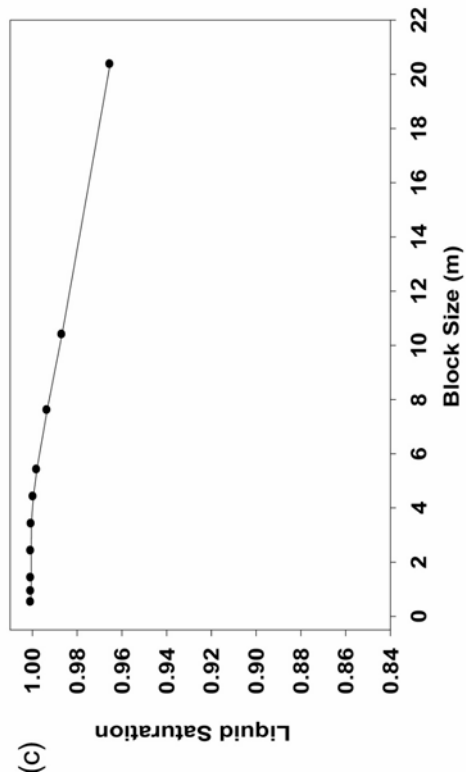
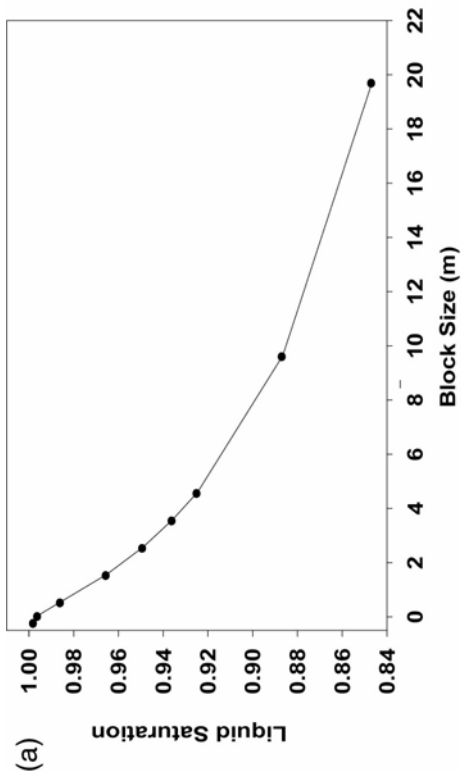
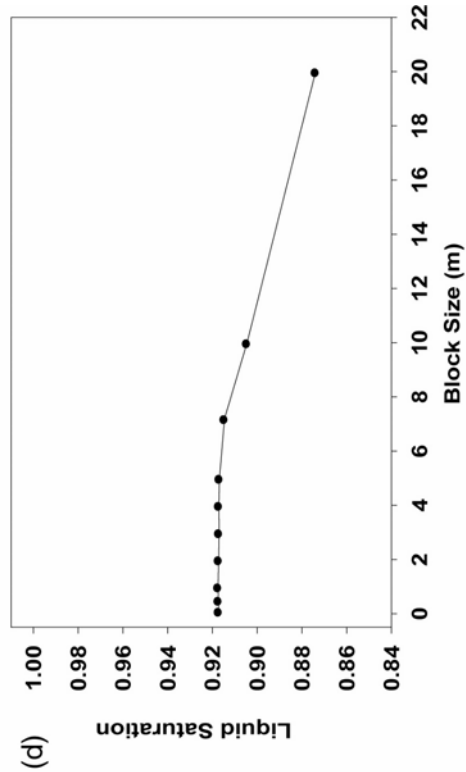
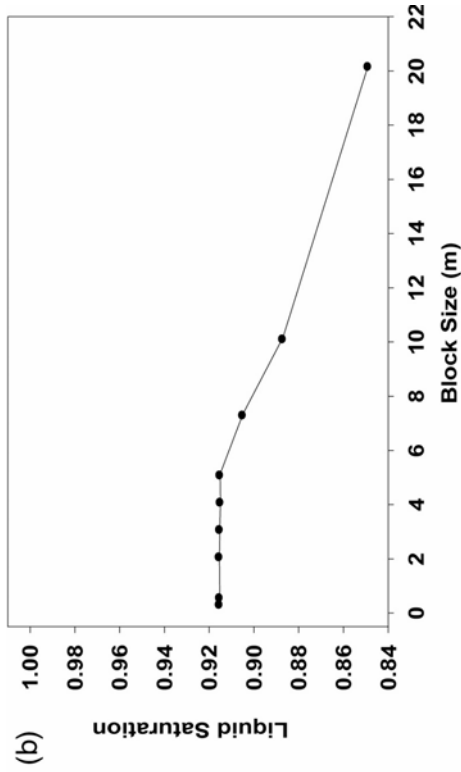


Figure 3.2-4. Ambient Matrix Saturation Predicted for  $T_{tpmn}$  at 8.9 m Above the Center of the Heated Drift Versus Model Block Size with a Value of  $1.23 \times 10^{-3}$  assigned to  $A_{mod}$  in  $T_{tpmn}$  for Infiltration Rates of 3.6mm/year in(a) and 0.072 mm/year in (b). Plots (c) and (d) are for  $A_{mod}$  1.0 and Infiltrations of 3.6mm/year and 0.072mm/year Respectively.

The analyses by Green, et al. (2001) indicated reductions in the intrinsic fracture permeability had a significant effect on the evolution of temperature and formation of heat pipes. In particular, a thousand-fold reduction in intrinsic fracture permeability effectively removed most evidence of a heat pipe in the numerical predictions. A reduction in thermal conductivity had a slightly less significant effect on the evolution of temperature. Changes in  $A_{\text{mod}}^*$  and inclusion of the active fracture model had an effect on the preheating ambient saturation but no effect on temperature or saturation in the thermohydrological simulations. MULTIFLO code Version 1.5.1 no longer uses the matrix/fracture area modifier  $A_{\text{mod}}^*$ . The active fracture model incorporated in these earlier analyses assigned the same reduction in permeability to fracture to matrix flux and fracture flow.

### 3.2.5 New simulations

#### 3.2.5.1 *Model heat source*

As in previous Drift Scale Test simulations (Green, et al., 2000, and 2001), heat was introduced into the current numerical model at the drift wall and at the inner and outer wing heaters. The drift cavity was not explicitly included in the model to avoid difficulties associated with representing the air space within the drift, radiative and convective heat transfer between the heater canisters and the drift wall, and the physics of heat and mass transfer at the drift-cavity/drift-wall boundary. The heat-source levels were applied uniformly according to surface area to each of the 20 drift boundary elements at the 5m diameter drift wall and to the 7 elements at the top of the invert. The 50 cylindrical wing heaters were not individually represented in the numerical model, but both the inner and outer wing heaters were represented as individual rectangular slabs, thereby smearing the heat deposition in the y-direction of the model. The 4.49m long inner wing heater was set 1.67m from the drift wall. The 4.5m long outer heater was separated from the inner heater by 0.66m. Both wing heaters were assigned a vertical thickness of 0.25m. These dimensions are consistent with those provided in the as-built report (CRWMS M&O 1998), with the exception of the wing heater thickness. The wing heaters were modeled as 0.25m thick, rather than the reported diameter of 24 mm, because of constraints on mesh resolution. The increased thickness of the wing heaters will distort the resulting thermohydrological regime in the region close to the heat source; however, the effect should be negligible beyond a few tens of centimeters.

The design heat output of the nine canister heaters at 68.0 kW total and that of the fifty wing heaters at 143.0 kW total (85.8 kW at the outer wing heaters and 57.2 kW for the inner wing heaters) add for a total design capacity of 211 kW. At the start of the heating phase on December, 1997 (Day 1), only 75% of the canister heat (approximately 52.8 kW) was applied, and the cumulative wing heater heat output was approximately 137 kW (CRWMS M&O 1998). The heat outputs from both the canister and wing heaters fluctuated by a small fraction throughout the heating phase for various reasons as shown by the data points in Figures 3.2-5 and 3.2-6. Also, the total heat outputs declined steadily but slowly over time. After 800 days of heating, both the canister and wing heater power outputs were intentionally decreased on 5 occasions to ensure that drift wall temperatures did not exceed 200°C. The solid lines in Figures 3.2-5 and 3.2-6 represent the amount of heat applied in the numerical modeling at various times in the heating phase.

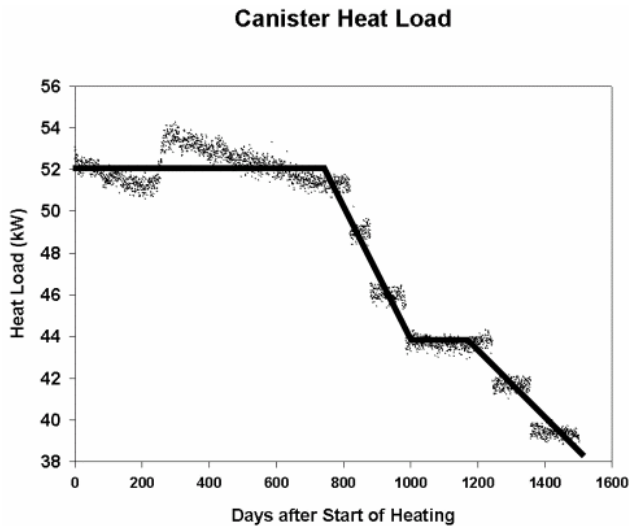


Figure 3.2-5. Measured heat output (kW) from the canister heaters during the four-year heating phase. Modeled heat indicated by solid line

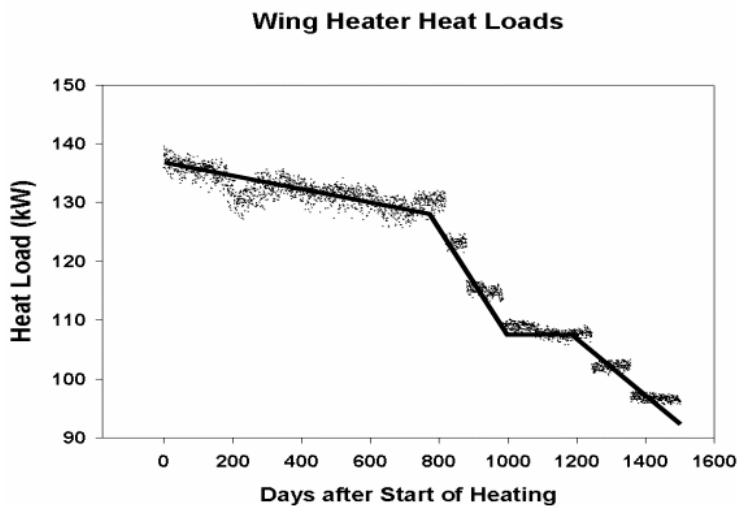


Figure 3.2-6. Measured heat output (kW) from the wing heaters during the four year heating phase. Modeled heat shown by solid line

### 3.2.5.2 Model features

Six different simulations were done with various combinations of model block size, heat load applied to the drift wall, and ambient matrix saturations as well as utilization of active fracture model and explicit representation of the wing heater boreholes. Model block sizes of small (0.4m) and large (5.0m), drift wall heat loads of full (100%) and reduced (80%), and saturations of high (0.99), moderately high (0.98), and moderate (0.90) were considered. Explicit representation of the hydraulic effects of the wing heater boreholes were accomplished by increasing the matrix and fracture permeabilities by factors of 10,000 and 1,000 respectively at the locations of the holes. Relative permeability properties for the matrix were also modified to be similar, although not identical to those of the fractures (i.e., residual saturation of 0.08,  $m$  of 0.5, and  $\alpha$  of  $1.0 \times 10^{-4}$ ). Thus, the six simulations involved:

- Simulation I: small block, full drift wall heat load, and high saturation
- Simulation II: small block, 80% drift wall heat load, and high saturation

- Simulation III: large block, full drift wall heat load, moderate saturation, and wing heater boreholes explicitly represented
- Simulation IV: large block, 80% drift wall heat load, moderate saturation, and wing heater boreholes explicitly represented
- Simulation V: small block, full drift wall heat load, moderately high saturation, and active fracture model
- Simulation VI: small block, 80% drift wall heat load, moderately high saturation, and active fracture model

### 3.2.5.3 Model results

Comparison of predicted temperatures to temperatures measured at Boreholes 158, 160, and 162, locations of which are shown in Figure 3.2-7, provides the best quantitative measure of the success of the model to replicate heat and mass transfer at the Drift-Scale Test. A feature of particular interest in temperature plots is the formation of a heat pipe. A lull in the rise of temperatures at the boiling point for some period of time is taken as evidence of a heat pipe. The presence of a heat pipe is of interest because a heat pipe acts as a particularly efficient heat transfer mechanism. A heat pipe may be an indication of a reflux halo, which, when located above the heaters, could be a source for water flowing downward toward the heaters.

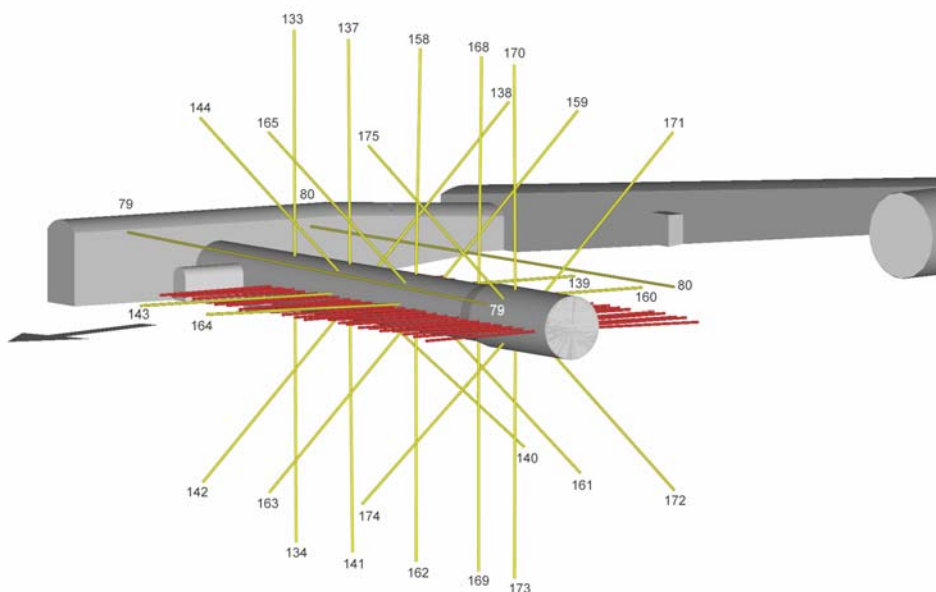


*Figure 3.2-7. Three Dimensional Perspective Showing Temperature Boreholes and Wing heater Holes*

The Task 2A of DECOVALEX III project requires predictions of temperature histories in boreholes 158, 160, and 162. Results from Simulation VI (small block with an active fracture model and a 20-percent reduction in drift wall heat load) was selected for the DECOVALEX project. This selection was based on examination of the temperature predictions at boreholes 158, 160, and 162. Simulation VI predicted temperatures that were, by inspection, closer to the observed temperatures in these boreholes than did the other simulations.

Predicted temperature at times of three months, one year, and four years after the start of heating in boreholes 158, 160, and 162 are shown plotted in Figure 3.2-8. Temperature histories at five sensor locations, # 3, 9, 23, 44, and 55 in these boreholes are shown in Figure 3.2-9. The temperature contour maps are omitted here.

Although not illustrated in these figures, matrix saturations predicted by the small block model differed significantly from that by the large block model. The dry-out zone was much larger for the small block model than that in the large block model especially at 4 years of heating. This suggests that movement of vaporized water from the matrix to the fracture medium is inhibited in the large block model.

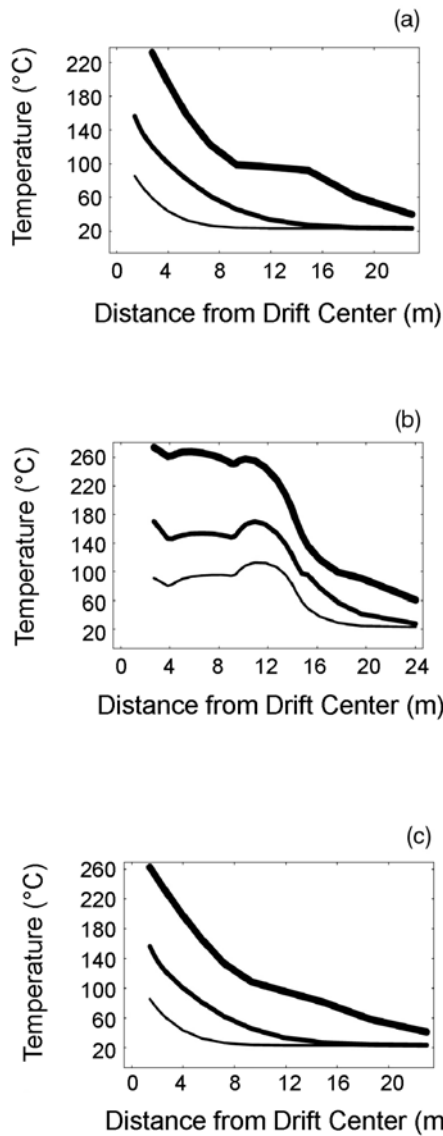


Figure 3.2-8. Plots of Predicted Temperatures in Boreholes (a) 158, (b) 160 and (c) 162 at Times of 3 Months (light line), 1 year (medium line) and 4 Years (heavy line)

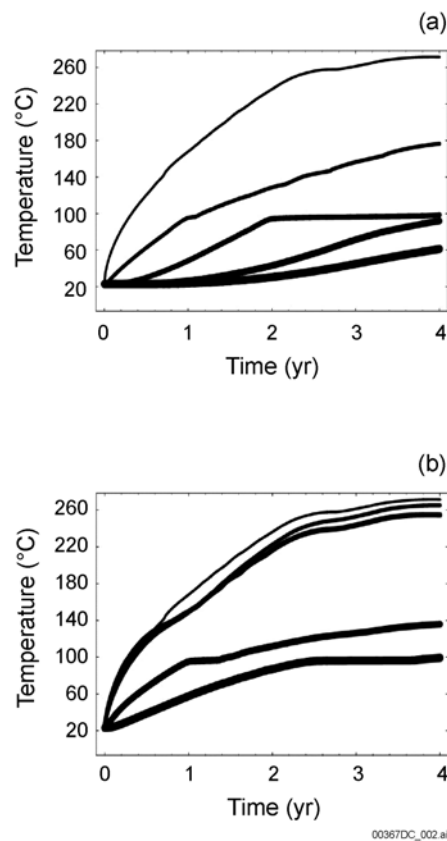


Figure 3.2-9. Plots of Temperature Histories in Boreholes (a) 158 and (b) 169 at Five Sensor Locations # 3, 9, 23, 44, and 55. Lightest Line is for Sensor # 3 and Heaviest Line is for Sensor #55

### 3.2.6 Summary of NRC team's modeling

The Drift Scale Test provides a basis to assess the capability of numerical codes to simulate complex thermal-hydrological processes in the rock mass surrounding nuclear waste repositories caused by the decay heat. In the most recent simulations the NRC research team improved upon the previous MULTIFLOW models (Green et al., 2000 and 2001) by changing from 2D to 3D model and by incorporating more realistic boundary conditions at the drift wall. The enhanced 3D model used an unstructured grid with two vertical planes of symmetry enabling simulation of only one-quarter of the model domain. The fractured rock was represented by two co-located media – one for the matrix and the other for the fractures to generate a dual continuum conceptual model similar to the double structure model of the ENRESA research team in Section 3.1 and the dual permeability model (DKM) of the DOE research team in Section 3.3. The effects of block size 0.4 m versus 5.0 m, reduction in the heat load applied to the drift wall, inclusion of an active fracture model, and explicit representation of the hydraulic conditions in the wing heater boreholes were the other changes from the previous models. Model predictions of temperatures were compared with temperatures measured in the Drift Scale Test at 3 months, 1 year, and 4 years after the start of heating to evaluate the performance of the modeling.

Combinations of property values and boundary conditions other than those used in these analyses can also predict reasonable ambient matrix saturations. Predicting an appropriate ambient saturation using a particular model does not in itself ensure that either the conceptual model or the assigned model input values are appropriate, or even acceptable, representations of the Drift Scale Test.

An increase in the model block size from 0.4 m to 5.0 m allowed relatively large infiltration rates of 3.0 mm/yr while maintaining a moderate ambient matrix saturation of approximately 0.90. Conversely, a relatively low infiltration rate of 0.07 mm/yr was required to attain a 0.90 matrix saturation for the small block in the standard case. In this case, an infiltration rate of 3.0 mm/yr resulted in an ambient matrix saturation in excess of 0.99. Modifying the standard model {i.e., small block model and infiltration of 3.0 mm/yr by invoking an active fracture model resulted in an ambient matrix saturation of approximately 0.98. The active fracture model therefore reduced the ambient saturation of the matrix for the small block simulations with relatively large infiltration (3.0 mm/yr). This apparent enigma among block size, infiltration, and saturation was also observed in previous two-dimensional simulations (Green, et al., 2000, 2001). These results indicate that model dimensionality (i.e., either two or three dimensions) is not a source of this enigma. Additional evaluations of the active fracture model may help resolve this enigma. However, at this time, model results from these simulations do not significantly reduce uncertainty in the values assigned to boundary conditions at Yucca Mountain (i.e., surface infiltration rates).

Based on visual comparative evaluation of the simulated and measured temperatures in boreholes 158, 160, and 162 the NRC team selected Simulation VI as the most appropriate model for the DECOVALEX exercise. Contour plots of temperatures and matrix and fracture saturations in Figures 3.2-10 through 3.2-18 are results from this simulation. As mentioned before, during initialization the small block active fracture model lowered the ambient saturation from 0.99 to 0.98 which is higher than the measured ambient saturation of 0.92. There was significant difference in the predicted matrix saturations between the small block model and the large block model as indicated by the larger dry-out zone in the small block model especially at four years after the start of heating.

### 3.3 DOE research team's TH modeling by using code TOUGH

As mentioned before, prior to the start of heating in the DST in December, 1997 DOE's research teams at LBNL and LLNL performed predictive TH modeling analyses of the test. While LLNL employed the NUFT code, LBNL used the TOUGH code. The pre-test TH modeling of the DST by LBNL is documented in the report, "Pretest Analysis of Thermal-Hydrological Conditions of the Drift Scale Test at Yucca Mountain", June 1997 authored by J.T. Birkholzer and Y.T. Tsang.

#### 3.3.1 Introduction

In their pre-test TH modeling of the DST in 1997 LBNL analyzed the temporal evolution and spatial variation of the thermal-hydrological conditions in the rock mass in the DST block. They also evaluated the impact of various input parameters such as heating rates and schedules, and of different percolation fluxes at the test horizon. In addition, conceptual model uncertainties are assessed by examining alternative conceptualizations of the matrix-fracture interaction such as the effective continuum model (ECM) and the dual permeability formulation (DKM) and the effect of radiative heat exchange in the Heated Drift (HD).

The TH modeling of the DST was performed in three dimensions by the multi-component, multi-phase flow-simulator TOUGH2 (Pruess, 1987 and 1991; Pruess et al., 1996). The configuration, parameters, and initial and boundary conditions of LBNL's model are designed to resemble the DST as closely as possible. Also, thermal and hydrologic properties measured in the laboratory on cores from the DST block, in-situ air permeability characterization, and information from borehole video logs have been incorporated into the DST model. Even so, due to the complexity of the many physical processes, the uncertainty in key input parameters such as fracture properties, and the fact that as-built information on borehole and sensor locations are unknown, the pre-test predictions in LBNL's report are expected to deviate from actual data. Nonetheless, the model provides an excellent *a priori* insight into the performance of the DST and serves as a baseline for future refinement and calibration against measured data.

#### 3.3.2 Test configuration

The DST facility and its configuration are described in Section 1.2 and illustrated in Figures 1-1, 1-2, and 1-3. The Heated Drift extends approximately in an east-west direction, parallel to the Observation Drift which connects the DST area with the ESF main drift. The end of the Heated Drift is 47.5 meter to the west of the bulkhead.

A local Cartesian coordinate system is employed to designate all spatial locations related to the DST. The origin (0,0,0) of the system is at the trace of the center line of the Heated Drift as excavated, on the hot side of the bulkhead. At the time of its excavation the Heated Drift was circular in cross-section and 5.0 m in diameter. Facing the DST bulkhead from the Connecting Drift, positive X is to the right, positive Y is toward the far (west) end of the Heated Drift, and positive Z is vertically upward.

As shown in Figures 1-1, 1-2, and 1-3, a large number of holes are drilled from the Heated Drift, the Observation Drift, and the Connecting Drift in the DST block to house numerous sensors of various kinds.

### 3.3.3 Conceptual model for pre-test predictions

The rationale behind the choice of model domain, properties of the various strata, percolation flux(es) at the DST horizon, and the different conceptualizations of fracture-matrix interactions such as the effective continuum model (ECM) and the dual permeability model (DKM) are discussed in this section.

The DST block is located in the Topopah Spring Middle Non-lithophysal (Tptpmn) stratigraphic unit at Yucca Mountain which is approximately 40 m thick in the DST area. Preliminary calculations indicate that the spatial extent of thermal-hydrological perturbation due to the application of the design heat load for four years will be well beyond the limits of Tptpmn. Therefore, stratigraphic units adjoining Tptpmn need to be included in the DST model. Matrix and fracture properties for the different stratigraphic units used in the DST model correspond to parameters derived from calibration against various measured data in Borehole SD-9 which is the closest to the DST block.

The thermal-hydrological response of the rock to the applied heat depends on the percolation flux at the DST horizon, a higher percolation flux can lead to lower temperatures and a larger extent of the condensation zone. The TH response of the DST is modeled for two values of the percolation flux, 3.6 mm/year and 0.36 mm/year.

The other parameter having substantial effect on the thermal-hydrological response of the rock is the fracture permeability which influences temperatures by heat convection, and impacts temporal evolution and spatial redistribution of moisture via the transport of water in both liquid and vapor phases. It is the gas phase permeability which is of particular importance, since the liquid phase permeability is typically very low in the welded tuffs at ambient temperatures. During the construction of the Heated Drift, field measurements of the gas-phase permeability were carried out in the DST block by air-injection tests in fourteen of the instrument holes drilled from the Observation Drift (Tsang and Cook, 1997). Based on these measurements the DST block is characterized as a fractured continuum with an average permeability of  $1 \times 10^{-13} \text{ m}^2$ .

Besides the permeability of the fracture and matrix continua, it is important to account for the interactions between the matrix and fractures. Previously, in modeling the Single Heater Test, Birkholzer and Tsang, 1996 showed that the dual permeability model (DKM) of matrix-fracture interaction give rise to higher liquid saturation in the fractures than the effective continuum model (ECM), resulting in larger gravity-driven downward flow. The difference in the modeled behavior resulting from the ECM and the DKM is in the dynamics, and can not be captured readily by passive monitoring data such as temperature and relative humidity. However, higher liquid saturations and perhaps, larger condensation zones below the heater horizon may give rise to distinguishable air permeability signatures to be recognized in air injection tests during the heating and cooling phases of the DST. In modeling the TH response of the DST, the ECM is applied to account for the combined effect of the matrix and fracture continua, while the dual permeability model (DKM) is applied to examine the sensitivity of the model results to this modeling concept.

### 3.3.4 Model implementation

Thermal-hydrological simulations of the DST in three dimensions and two dimensions are performed with the Integrated Finite Difference Code TOUGH2 (Pruess, 1987 and 1991). TOUGH2 is a numerical simulation program for non-isothermal flows of multi-component, multi-phase fluids in porous and fractured media. The TOUGH2-

EOS4 module is used which accounts for the non-isothermal two phase flow of water and air, including vapor-pressure lowering effects. The effective continuum approach is applied to account for the net effect of the matrix and fracture continua. A dual permeability formulation is used for certain realisations to study the sensitivity of the results to this modeling concept.

### 3.3.5 Model domain

The model domain for thermal-hydrological simulation of the DST include the DST block and a substantial volume of rock surrounding it in all directions to ensure proper definition of boundary conditions. Besides covering the entire thickness of the Topopah Spring Middle Non-lithophysal unit (Tptpmn) in which the Heated Drift is situated, the vertical extent of the model includes the overlying Topopah Spring Upper Lithophysal unit (Tptpul) and the underlying Topopah Spring Lower Lithophysal unit (Tptpll).

The thicknesses of the three geologic units and their locations (Z coordinate) are tabulated below:

<b>Geologic Unit</b>	<b>Thickness (m)</b>	<b>Bottom Elevation (m)</b>	<b>Top Elevation (m)</b>
Topopah Spring Upper Lithophysal (Tptpul)	85.39	14.00	99.39
Topopah Spring Middle Non-lithophysal (Tptpmn)	40.68	-26.68	14.00
Topopah Spring Lower Lithophysal (Tptpll)	130.08	-156.76	-26.68

The northern and southern lateral boundaries of the model are 90.0 m north and 90.0 m south respectively, of the centerline of the Heated Drift. The eastern and western lateral boundaries are 90.0 m east and 137.5 m west respectively, of the hot side of the bulkhead. The western lateral boundary is thus 90.0 m west of the western end of the Heated Drift. Figure 3.3-1 shows an XZ cross-section of the whole model domain.

### 3.3.6 Model parameters

As mentioned in section 3.3.3, matrix and fracture properties of the various stratigraphic units used in modeling the DST are obtained by calibration by inversion to measured data associated with the borehole SD-9. The calibration is performed by the inverse modeling code ITOUGH2 (Finsterle, 1993; Finsterle et al., 1996), applied to a one-dimensional vertical column from the ground surface, which is couple of hundred meters above the upper model boundary, to the water table which is several hundred meters below the lower model boundary. Steady state conditions and constant infiltration rates are assumed and fracture-matrix interaction is modeled by the ECM concept. Separate calibrations are performed for the two infiltration rate scenarios of 3.6 mm/year and 0.36 mm/year.

The rock properties are calibrated against measure saturation and water potential data at the borehole SD-9. Calibration provides permeability and van Genuchten  $\alpha$  and  $m$  for both fracture and matrix. The parameters to which the thermal-hydrological response of the DST are most sensitive are thermal conductivity, fracture gas-phase permeability, and initial liquid saturation of the Tptpmn unit in which the DST block is located. Ambient (pre-heat) characterization data on these parameters specific to the DST area are available (CRWMS M&O, 1997). These *a-priori* known data are treated as “fixed” in the calibration i.e they are not changed in the calibration procedure. In particular, the fracture permeability of Tptpmn is set at  $\times 10^{-13} \text{ m}^2$  based on the pre-test air permeability field measurements (Tsang and Cook, 1997). The matrix saturation of Tptpmn is set at 92% or 0.92 based on a large number of measurements in the laboratory on samples of this rock from the DST area and the hole SD-9.

The values of various parameters used as input in the TH modeling of the DST are given in Table 3.3-1.

### 3.3.7 Boundary and initial conditions

Results from the calibrated 1-D vertical column model are used to interpolate appropriate boundary conditions at the top and bottom of the 3-D DST model domain. Therefore, additional 1-D vertical column runs are performed with the adjusted vertical stratigraphic data corresponding to the conditions at the DST area. Vertical profiles of initial saturation, pressure, and temperature are then interpolated on the 3-D DST grid, depending on the Z coordinate (elevation) of the respective grid blocks. At the bottom, the boundary elements have constant pressure, saturation, and temperature throughout the simulation period. At the top a constant temperature, and a constant infiltration flux such as 3.6 mm/year or 0.36 mm/year as the case may be, apply. To avoid unwanted perturbations, initialization runs with the 3-D DST model are performed for a period of 10,000 years before applying the heat to ensure that an initial steady state is achieved. All lateral boundaries of the model are no-flow boundaries for heat, liquid, and gas.

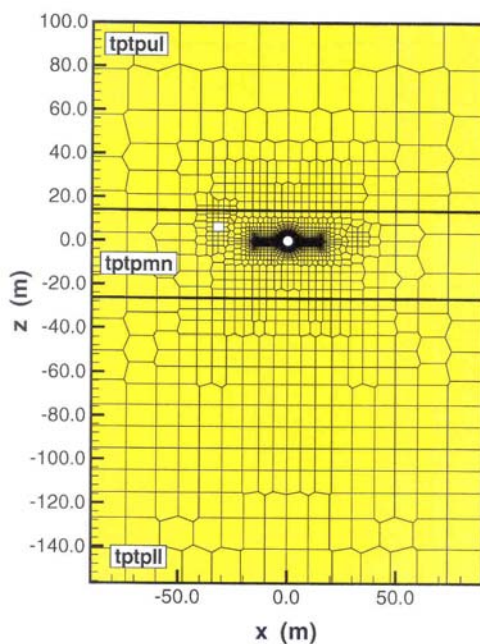


Figure 3.3-1. Cross-Section (XZ) of Model Domain Showing Stratigraphic Units

Table 3.3-1. Parameter values for various model layers

Parameter	Ttpul	Ttpmn	Ttpll
Matrix Porosity	0.154	0.11	0.13
Matrix Residual Liquid Saturation	0.06	0.18	0.08
Rock Particle Density in kg/m <sup>3</sup>	2510.0	2530.0	2540.0
Fracture Porosity	0.000171	0.000263	0.000329
Fracture Residual Liquid Saturation	0.01	0.01	0.01
Rock Thermal Conductivity in W/(m <sup>o</sup> K) (wet)	1.7	2.0	2.29
Rock Thermal Conductivity in W/(m <sup>o</sup> K) (dry)	1.15	1.67	1.59
Rock Mass Heat Capacity in J/(kg <sup>o</sup> K)	916.7	952.9	952.9
Fracture Permeability (m <sup>2</sup> ) for Infiltration of 3.6 mm/year	0.202 x 10 <sup>-11</sup>	0.100 x 10 <sup>-12</sup>	0.155 x 10 <sup>-11</sup>
Fracture Permeability (m <sup>2</sup> ) for Infiltration of 0.36 mm/year	0.635 x 10 <sup>-12</sup>	0.100 x 10 <sup>-12</sup>	0.187 x 10 <sup>-11</sup>
Matrix Permeability (m <sup>2</sup> ) for Infiltration of 3.6 mm/year	0.200 x 10 <sup>-16</sup>	0.914 x 10 <sup>-17</sup>	0.233 x 10 <sup>-16</sup>
Matrix Permeability (m <sup>2</sup> ) for Infiltration of 0.36 mm/year	0.525 x 10 <sup>-17</sup>	0.124 x 10 <sup>-16</sup>	0.247 x 10 <sup>-15</sup>
Fracture van Genuchten $\alpha$ for Infiltration of 3.6 mm/year	0.314 x 10 <sup>-4</sup>	0.217 x 10 <sup>-4</sup>	0.234 x 10 <sup>-4</sup>
Fracture van Genuchten $\alpha$ for Infiltration of 0.36 mm/year	0.157 x 10 <sup>-3</sup>	0.973 x 10 <sup>-4</sup>	0.166 x 10 <sup>-4</sup>
Matrix van Genuchten $\alpha$ for Infiltration of 3.6 mm/year	0.611 x 10 <sup>-5</sup>	0.171 x 10 <sup>-5</sup>	0.335 x 10 <sup>-5</sup>
Matrix van Genuchten $\alpha$ for Infiltration of 0.36 mm/year	0.106 x 10 <sup>-4</sup>	0.225 x 10 <sup>-5</sup>	0.282 x 10 <sup>-5</sup>
Fracture van Genuchten m for Infiltration of 3.6 mm/year	0.492	0.483	0.492
Fracture van Genuchten m for Infiltration of 0.36 mm/year	0.492	0.492	0.492
Matrix van Genuchten m for Infiltration of 3.6 mm/year	0.252	0.320	0.229
Matrix van Genuchten m for Infiltration of 0.36 mm/year	0.243	0.247	0.207

Except for the heated section of the Heated Drift and the bulkhead, the drifts are modeled by constant pressure, temperature, and saturation conditions, as they are ventilated and the heating of the rock does not affect the parameters in the open drift. The non-heated length of the Heated Drift and the walls of the Connecting Drift and the Observation Drift nearer the heaters are to be insulated by a low thermal conductivity material. This insulation is explicitly modeled as 15.2 cm thick, having a density of 32 kg/m<sup>3</sup>, a thermal conductivity of 0.0447 W/(m<sup>o</sup>K), and a heat capacity of 835 J/(kg<sup>o</sup>K). The heat load generated inside the Heated Drift is applied directly onto the elements adjacent to the drift wall. Radiative heat exchange within the Heated Drift is not explicitly modeled. Since it is not known if radiation in the drift is effective enough to completely equilibrate the temperature along the drift wall, two extreme cases of drift

wall boundary conditions are examined: 1) In the first case, a *uniform areal heat load* is introduced at the rock surfaces along the drift wall, which will eventually give rise to cooler temperatures at the two ends of the Heated Drift. 2) In the second case, a *uniform temperature* is assumed at the rock surfaces along the entire length of the Heated Drift. The first case represents a less effective radiative heat exchange within the drift, and the second case represents 100% effective black body radiation within the drift. The real system behavior is expected to be somewhere between the two cases.

The wing heaters are modeled as two horizontal planar smeared-out heat sources on either side of the Heated Drift at an elevation of  $Z = -0.25$  m. Since the inner and outer wing heater segments are each 4.75 m long having a power output of 1145 watts and 1728 watts each respectively and assuming the heat output is uniformly distributed along the 47.5 m length of the Heated Drift, the areal heat load amounts to a maximum of  $126.9 \text{ W/m}^2$  for the inner wing heaters and  $190.1 \text{ W/m}^2$  for the outer wing heaters.

### 3.3.8 Pre-test predictive modeling results

The thermal-hydrological conditions of the DST are modeled for infiltration rates of 3.6 mm/year and 0.36 mm/year each for a specific heating schedule which is 100% (full capacity) power output from both the in-drift heaters and the wing heaters for the first one year, followed by a drop in power to 50% for the next three years. After the four year heating period the heaters are turned off, and the rock mass is allowed to cool. For this heating rate two modes of heat transfer inside the Heated Drift are studied: a) a uniform heat load applied along the drift wall; and b) a uniform temperature is assumed at the rock surfaces along the drift wall.

Before the three-dimensional simulations, sensitivity studies are performed by 2-D analyses to search for a heating rate that will keep the wall temperatures in the Heated Drift below  $200^{\circ}\text{C}$  throughout the heating period. The heating rate described above meets this  $200^{\circ}\text{C}$  criterion for both the 3.6 mm/year and 0.36 mm/year infiltration rate cases.

Predicted temperature histories at the crown (top), springline, and bottom of the drift at  $Y = 30.18$  m are shown in Figures 3.3-2 and 3.3-3 for the 3.6mm/year and 0.36mm/year infiltration cases respectively. These simulated temperature history plots are similar to each other reflecting the heating schedule of 50% drop in heater power at one year and termination of heating at four years. As expected, the temperatures are higher for the case of 0.36 mm/year infiltration case.

Simulated matrix and fracture liquid saturations at the XZ cross section at  $Y = 30.18$  after one year of heating are shown in Figures 3.3-4, 3.3-5 for the 3.6 mm/year infiltration case and in Figures 3.3-6, and 3.3-7 for the 0.36 mm/year infiltration case respectively. There is little difference between the simulated saturations between the high and low infiltration cases.

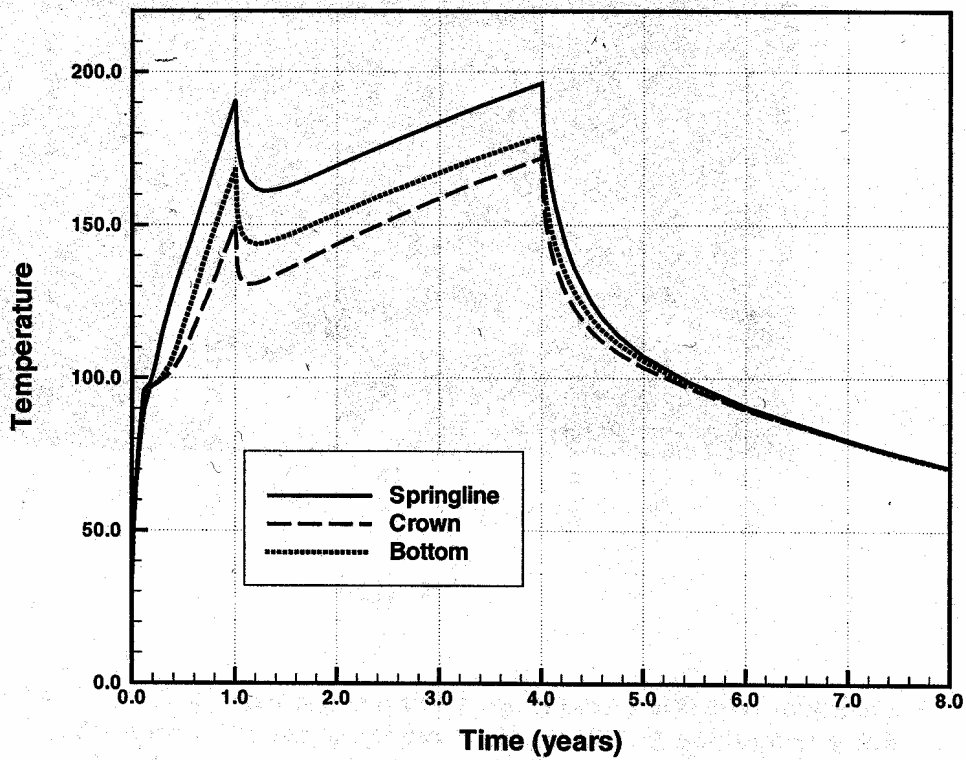


Figure 3.3-2. Temperature History on the Heated Drift Wall at Y=30.18m During Four Years Each of Heating and Cooling for 3.6 mm/year Infiltration Rate

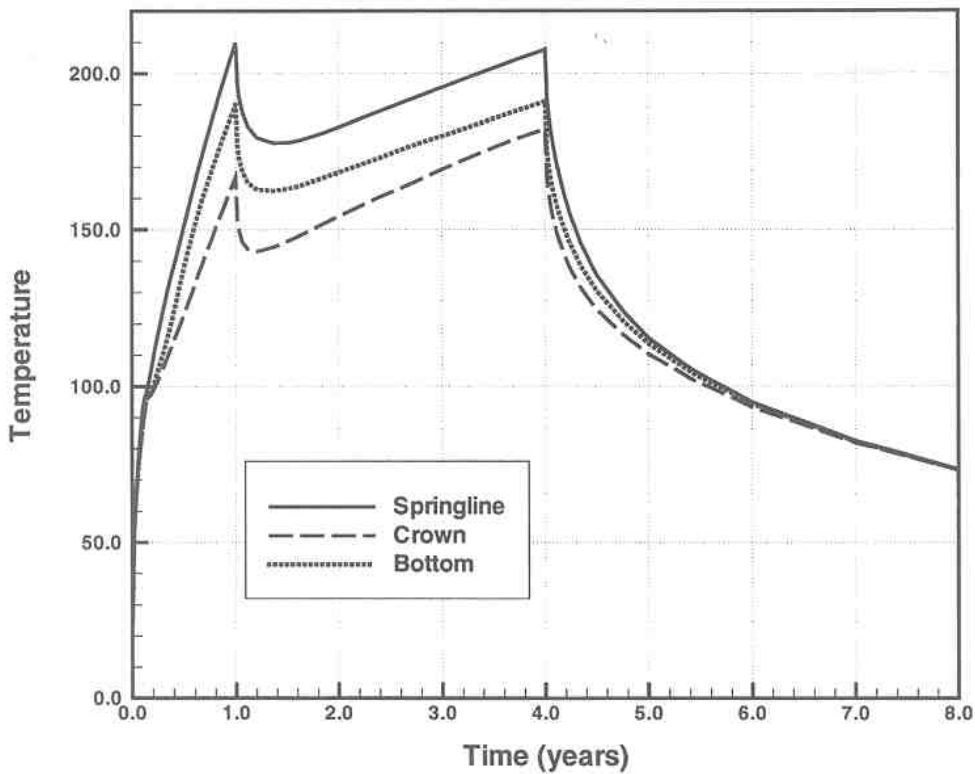


Figure 3.3-3. Predicted Temperature History at Y=30.18 m for 0.36 mm/year Infiltration Case

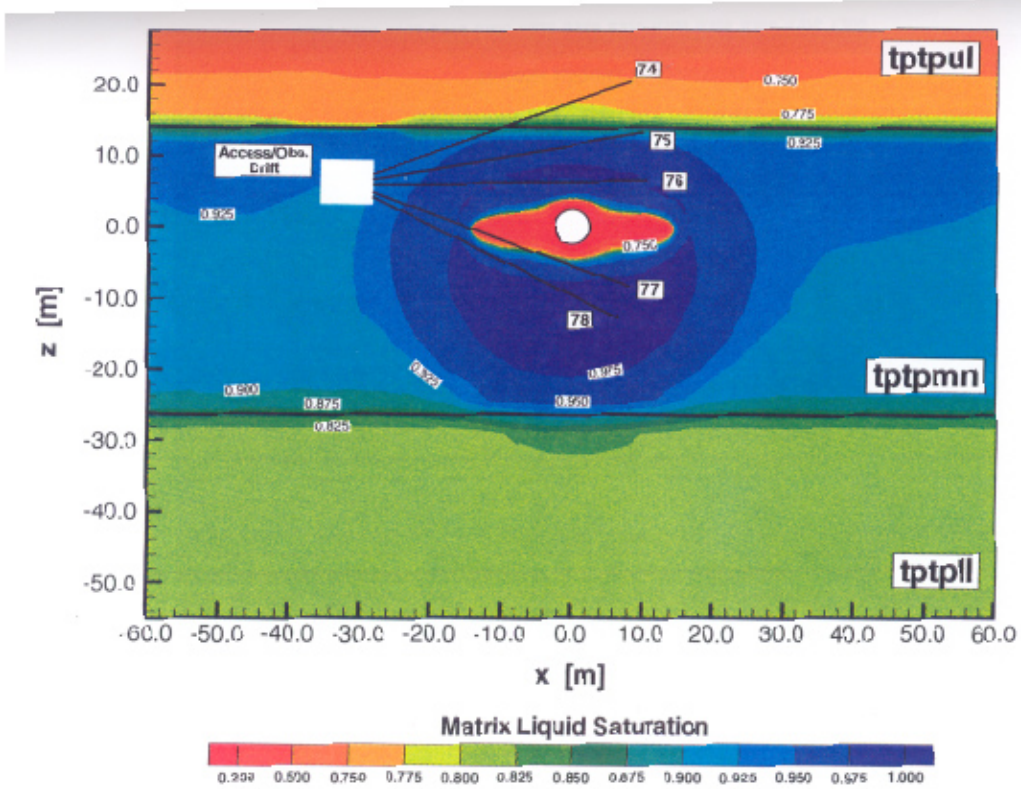


Figure 3.3-4. Matrix Liquid Saturation at One Year of Heating at the XZ Section at  $Y=30.18$  m for 3.6 mm/year Infiltration Rate

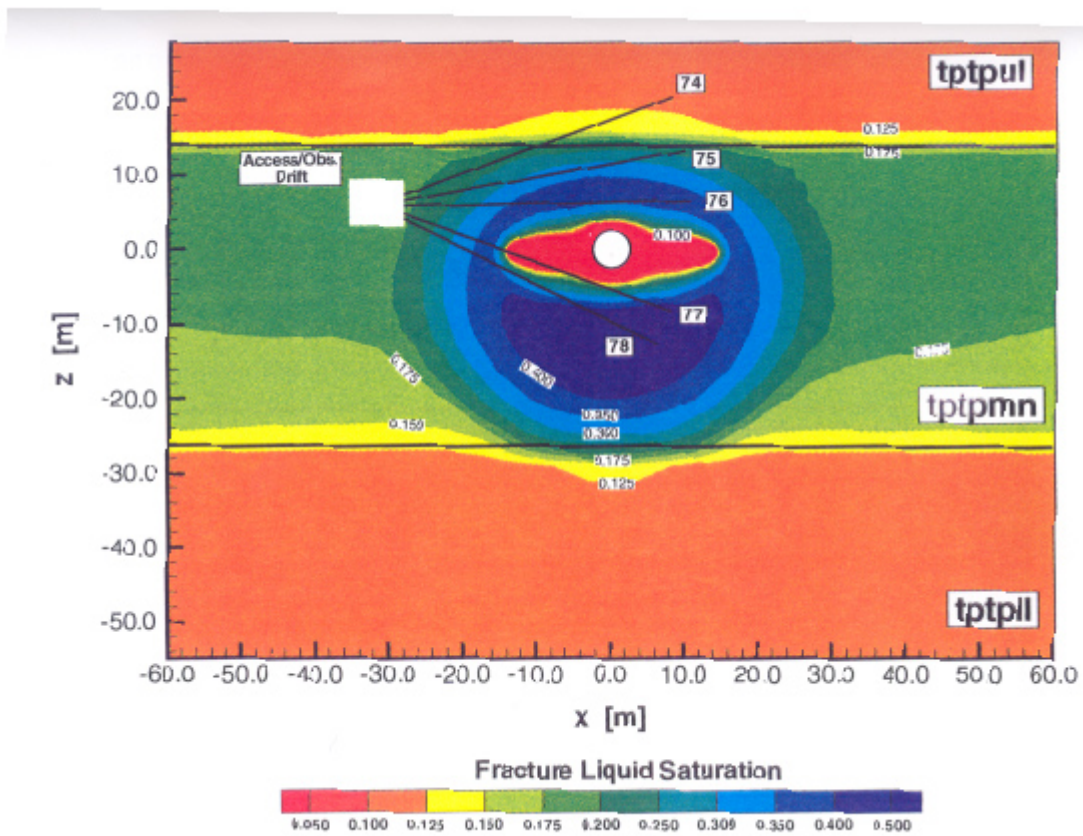


Figure 3.3-5 Fracture Liquid Saturation at One Year of Heating at the XZ Section at  $Y=30.18$  m for 3.6 mm/year Infiltration Rate

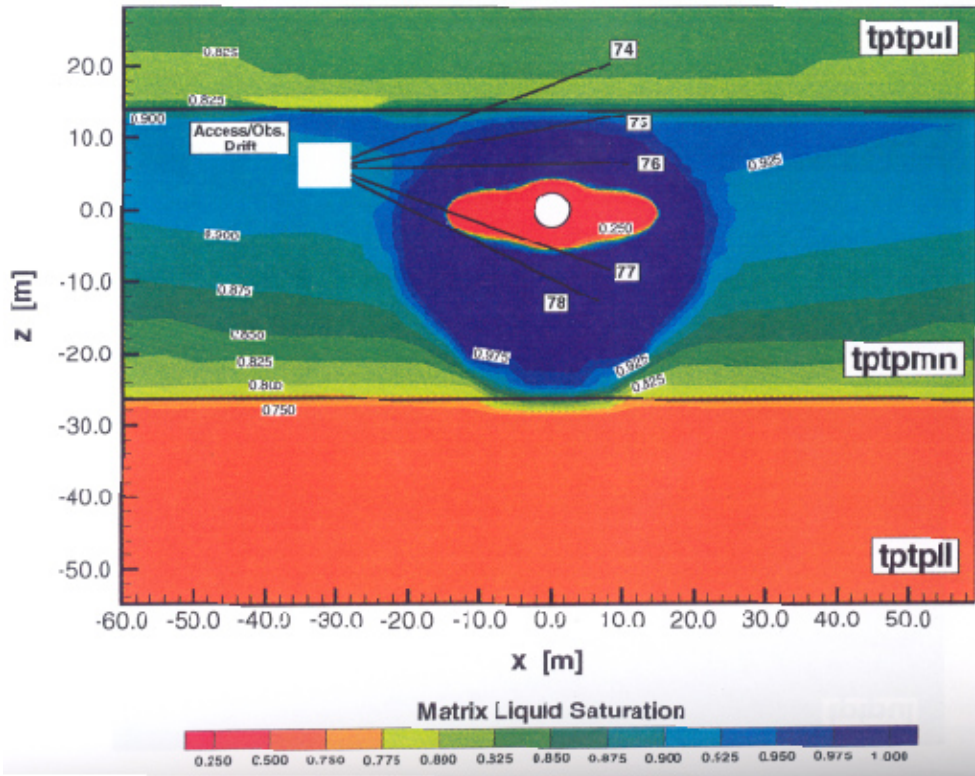


Figure 3.3-6. Matrix Liquid Saturation at XZ Section at Y=30.18 m after One Year of Heating for 0.36mm/year Infiltration

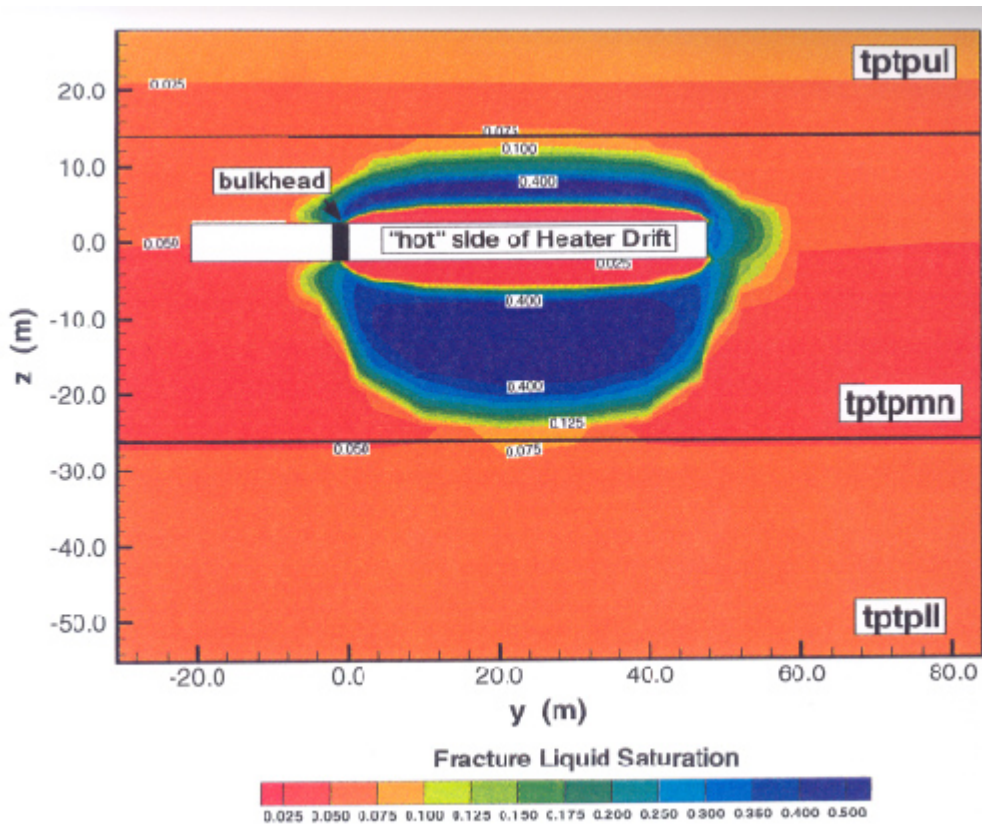


Figure 3.3-7. Fracture Liquid Saturation at One Year of Heating at the XZ Section at Y=30.18 m for 0.36 mm/year Infiltration Rate

### **3.3.9 Evolution of TH simulation of DST by using code TOUGH**

The predictive TH modeling of the DST by TOUGH summarized in the preceding sub-sections of Section 3.3 and described in detail in Birkholzer and Tsang (1997) had been carried out prior to the initiation of heating in December 1997. The outcome of this pre-heating modeling was the basis of detailed planning and design for the test as well as that for forecasting the TH response during the planned eight year heating and cooling.

Once the heaters had been activated and measurements of temperature, gas pressure, and water saturation became available, early test results from the first six months of heating were used to discriminate between alternative modeling concepts applied in pre-test simulations. It became clear, for example, that the dual-permeability method describes fracture-matrix interaction much better than the effective-continuum model. Temperature data also showed that heat radiation within the Heated Drift is effective, indicating that a uniform temperature distribution at the drift wall can be assumed. In addition to model conceptualization, several model modifications were made to account for test conditions that were different from the assumed conditions of the pre-test simulations. These modifications were:

1. adjusting the input heater power to account for the measured heat load of the DST
2. changing the boundary conditions at the bulkhead to allow convective flow between the hot and the cool side
3. adding the concrete invert in the Heated Drift
4. including the effects of ventilation and minor temperature buildup close to the drift walls prior to heater activation.

Other than adjusting the conceptual model as above to better represent the actual test conditions, the pre-test predictive model was not changed. In particular, the site-specific rock properties were not adjusted.

At six months of heating, the refined DST TH Model was frozen. The frozen model was used to predict the remaining heating and the cooling phase of the DST. With the test ongoing and more and more data becoming available, a continued comparative analysis of predictive simulations and measured data was performed. Based on the generally good agreement between measured and simulated data, only one more model modification became necessary. At 30 months of heating (September 2000), gridblocks representing wing heaters were assigned a permeability value three orders of magnitude higher than that of the surrounding rock mass, to account for the fact that wing heaters are installed in boreholes that are open conduits for gas flow.

All modeling results presented hereafter in Section 3.3.9 are based on the conceptual model that includes the above adjustments and modifications.

#### ***3.3.9.1 Conceptual model for ongoing TH simulation of DST***

The conceptual model for continued TH simulation of the DST, similar to that of the pre-test predictive models, is briefly summarized below.

##### **a) Continuum representation**

Fractures are modeled as an effective continuum using averaged parameters for simulating the unsaturated flow and heat transport processes. A continuum

representation of unsaturated fracture flow is appropriate when fracture density is high and a well-connected fracture network can form at the scale of interest. Such representation for the flow conditions in the UZ at Yucca Mountain is supported by the dispersive nature of fracture water flow in the densely fractured, welded tuff units at the proposed repository site. Based on this assessment, continuum approaches are the main modeling method for the UZ at Yucca Mountain, applied in simulations for water flow, heat transfer, and contaminant transport.

#### b) Dual-Permeability method

A key issue for simulating fluid and heat flow in the fractured-porous rock of Yucca Mountain is how to handle fracture and matrix flow and interactions under multiphase, multicomponent, nonisothermal conditions. For simulating the DST the dual-permeability method (DKM) is applied to evaluate fluid and heat flow in the fracture rock. This methodology is based on the modeling framework of so-called dual-continuum models. Such models are often applied to fractured porous rock, where one component (the fractures) typically has a large permeability, but small porosity, while the other component (the rock matrix) has a larger porosity, but small permeability. The dual-permeability method accounts for these differences by assuming two separate, but interacting continua that overlap each other in space, one describing flow and transport in the fractures, the other describing flow and transport in the matrix. Each continuum is simulated with a separate numerical grid, separate TH properties, and separate variables (pressure, saturation, and temperature). Thus at each location in space, there is a fracture gridblock and an overlapping matrix gridblock. The two gridblocks at each location are connected to model the interaction between the two continua. Global flow occurs within the fracture continuum and the matrix continuum, while local interflow occurs between the two continua as a result of the local pressure and temperature difference. The interflow between fractures and matrix is handled using a quasi-steady transfer, estimating the exchange of fluid, gas, and heat between the two components by a linear gradient approximation. Details have been well documented in Doughty (1999).

#### c) Active Fracture model

The DKM, as introduced above, typically considers flow to occur through all the connected fractures and to be uniformly distributed over the entire fracture area. In this case, the entire fracture-matrix interface area is available for coupling of flow between the matrix and fractures, implying relatively large fracture-matrix interactions. In natural systems, however, unsaturated fracture flow is not uniformly distributed because (a) flow channels may form within a fracture, and (b) only a subset of all fractures may be actively contributing to the flow processes. To account for this reduced coupling between the fracture and the matrix continua, the active fracture model (AFM) was developed to modify fracture-matrix interface areas for flow between fracture and matrix systems (Liu et al. 1998). The AFM proposes to use a fracture-matrix reduction factor proportional to a power function of liquid saturation, with the power function coefficient calibrated from measured data. The AFM was chosen as the primary conceptual model for simulation of the TH processes in the DST.

The mathematical description of the coupled transport of water, water vapor, air, and heat is identical. The resulting mass-and energy-balance equations are solved with the integral finite-difference simulator TOUGH2V1.3MEOS4.

### 3.3.9.2 Model domain and numerical grid

The numerical grid for the DST test was designed to represent the test geometry and dimensions, including the drifts, alcoves, the decline of the observation drift, and the location of boreholes, as realistically as possible. (Note that the nominal design dimensions were used to generate the grid. The differences between nominal and as-built dimensions are small, and do not affect the modeling results.) This required development of a three-dimensional model. Significant rock volumes in all directions beyond the immediate DST block are included in the modeled domain to guarantee a proper definition of boundary conditions (that is, to insure that boundaries remain in their ambient, preheat conditions for the duration of the DST).

Figure 3.3-1 shows the model domain and discretization of a typical x-z cross section in the 3-D model for the DST. The origin of the 3-D coordinate system is located on the hot side of the bulkhead, in the center of the drift. The positive x-axis points horizontally, approximately towards the north (transverse to the Heated Drift away from the Observation Drift); the positive y-axis points horizontally along the Heated Drift, approximately towards the west; and the positive z-direction points vertically upward from the origin. Thus, the Heated Drift originates at  $y = 0$  and terminates at  $y = 47.5$  m. Note that the vertical extent of the model region includes the stratigraphic units both above and below that of the middle nonlithophysal unit (Ttpmn) of the test block. (The stratigraphy is extracted from the nearby borehole USW SD-9.) They are respectively the upper (Ttpul) and lower (Ttpll) lithophysal units of the Topopah Spring welded tuff. The grid was designed such that the assumed interfaces between layers are represented by gridblock interfaces (i.e., interfaces are maintained at  $z = +14.0$  m and  $z = -26.68$  m).

Figure 3.3-8 shows the same cross section in a detailed view of the rock areas adjacent to the Heated Drift and the wing heaters. The figure also depicts the configuration of boreholes 158 through 165, which form a cluster oriented radially outward from the Heated Drift. This vertical plane containing these eight boreholes intersects the long axis of the drift at  $y = \sim 23$  m. Temperature sensors are grouted in each of these boreholes at approximately 0.3 m spacing.

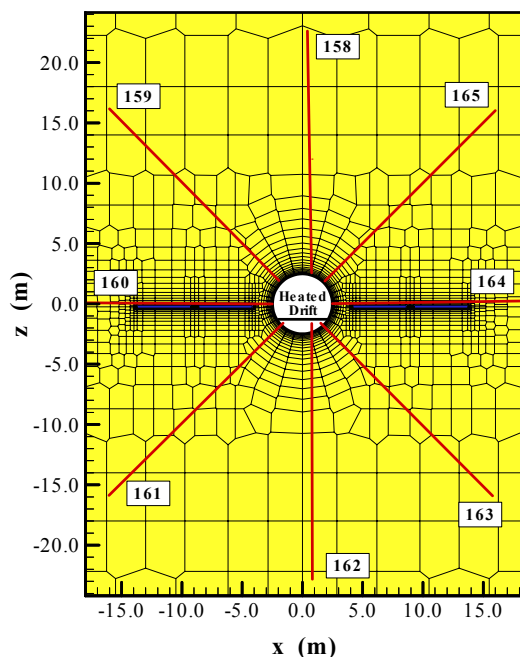


*Figure 3.3-8. Detailed View of Vertical Cross Section of DST Numerical Grid through Plane Containing Temperature boreholes 158 through 165*

### 3.3.9.3 Model boundary conditions

The top and bottom boundaries of the DST domain ( $z = +99.39$  m and  $-156.76$  m, respectively) are given constant boundary conditions of pressure, saturation, and temperature. The side boundaries of the domain are located outside of the test influence area and are considered no-flow boundaries. The Observation Drift, the Connecting Drift, and the cool section of the Heated Drift are given constant pressure, temperature, and saturation boundary conditions. The non-heated section of the Heated Drift and the walls of the Connecting Drift and Observation Drift near the Heated Drift are insulated, but allow for moisture to escape from the test block in the form of both liquid water and vapor. The Heated Drift is open to advection and conduction of heat and mass as well as vapor diffusion. A constant percolation flux is imposed at the top boundary of the model domain, representing an estimate of the present-day percolation at the location of the DST.

#### a) Thermal bulkhead

Early pressure measurements from the hot and cool sides of the Heated Drift indicated that the insulated bulkhead was acting as an open boundary for gas flow, allowing vapor to escape from the Heated Drift. As a result, the predictive numerical model for the DST was changed in 1998, utilizing a bulkhead boundary condition that conforms to the actual test conditions. A high-permeability connection for gas flow was introduced between the gridblocks, representing the hot side and the cool side of the Heating Drift, so that the simulated bulkhead acts as an open boundary. Model results using this boundary condition show significant amount of vapor escaping from the Heated Drift. On the other hand, the bulkhead is given small thermal conductivity, preventing heat transfer at the bulkhead by conduction.

The issue of heat and mass loss through the bulkhead has been discussed and evaluated in several thermal workshops. In short, there was concern that the amount of vapor escaping through the bulkhead is not appropriately monitored, and that the thermal response of a closed system might be different from the thermal response of an open system, where the volume of condensed water remaining in the rock is smaller. A detailed evaluation of this issue is presented in Mukhopadhyay and Tsang (2003). The revised model with the open-bulkhead boundary condition was considered appropriate for representing heat losses through the bulkhead, based on a reasonably small difference between measured and simulated temperature.

#### b) Thermal load

The total heating power applied to the DST TH Model reflects average values of the actual heating power. Average values were calculated for each time period that had a different heater output as designed by the Thermal Test Team. This means that the few planned power reductions or increases during the test period are accounted for explicitly, while short-term heater output variations—e.g., as a result of short-term power outages—are averaged out. The periods of identical average heater power output, as applied to the model, are given in Table 3.3-2 separately for the floor heaters and the wing heaters. The heaters were turned off on January 14, 2002, after about 49.5 months of heating.

*Table 3.3-2. Total Average Heater Power at Various Times of Heating in the DST*

<b>Time</b>	<b>Floor Heaters (kW)</b>	<b>Wing Heaters (kW)</b>
12/03/1997-05/31/1999	52.1	132.1
06/01/1999-03/02/2000	50.0	125.1
03/02/2000-05/02/2000	47.9	120.4
05/02/2000-08/15/2000	45.8	114.6
08/15/2000-03/31/2001	43.3	106.4
04/01/2001-05/02/2001	43.4	106.7
05/02/2001-08/22/2001	41.4	101.6
08/22/2001-09/30/2001	39.4	96.3
10/01/2001-01/14/2002	39.4	96.8

In the DST model, the heat generated from in-drift heaters is applied directly to the drift wall, which is assigned a large thermal conductivity that would equilibrate its temperature. Spatial variation of drift-wall temperature data for the DST is small. Because the main objective of this Model Report is the quantification of TH processes in the rock mass outside the drift, it is not necessary to capture the rapid radiative heat transfer within the drift in detail. Also, to limit the complexity of the 3-D numerical grid, the wing heaters are represented as smeared-out, spatially uniform heat sources. Only the rock temperatures within one heater spacing of the wing heaters will be misrepresented in the simulation because of this simplified representation, and few temperature sensors are located there.

c)Initial conditions

The initial values of pressure, temperature, and saturation in the DST model are developed from initialization runs with the 3-D grid, using the selected top and bottom boundary conditions. The initialization runs are performed for a long time before turning on the heat, ensuring that an equilibrium condition is achieved. In addition, the impact of elevated temperatures in the drifts (from installation activities in the summer months prior to starting the test), and of rock mass drying within a few meters of drift walls from ventilation of the drifts are accounted for in the numerical model.

**3.3.9.4 Model parameters and rock properties**

Two different sets of rock properties are used in ongoing modeling of the TH response in the DST. The first set, DKM-TT99, is based largely on site-specific data for the DST block derived from the results of ambient characterization of the test block before the start of heating in December, 1997. The other set, DS/AFM-UZ02, is derived from mountain scale or repository scale calibration runs under ambient conditions and is expected to better represent the average properties of the various stratigraphic layers.

Table 3.3-3 Summary of Hydrological and Thermal Properties of Geologic Units Tptpul, Tptpmn, and Tptpll

Geol. Unit >		DS/AFM-UZ02			DKM-TT99		
		Tptpul (tsw33)	Tptpmn (tsw34)	Tptpll (tsw35)	Tptpul (tsw33)	Tptpmn (tsw34)	Tptpll (tsw35)
MATRIX DATA							
Permeability	$k_m$ (m <sup>2</sup> )	6.57E-18	1.77E-19	4.48E-18	5.25E-18	1.24E-17	2.47E-16
Porosity	$f_m$ (-)	0.1425	0.1287	0.1486	0.154	0.11	0.13
van Genuchten $\alpha$	$\alpha_m$ (1/Pa)	6.17E-6	8.35E-6	1.08E-5	1.06E-5	2.25E-6	2.82E-6
van Genuchten m (or $\lambda$ )	$m_m$ (-)	0.283	0.317	0.216	0.243	0.247	0.207
Residual saturation	$S_{irm}$ (-)	0.12	0.19	0.12	0.06	0.18	0.13
Rock grain density	$\rho$ (kg/m <sup>3</sup> )	2358	2466	2325	2510	2530	2540
Rock grain specific heat capacity	$C_p$ (J/kg K)	985	985	985	917	953	953
Bulk dry thermal conductivity	$\lambda_{dry}$ (W/m K)	1.164	1.419	1.278	1.15	1.67	1.59
Bulk wet thermal conductivity	$\lambda_{wet}$ (W/m K)	1.675	2.074	1.890	1.7	2.0	2.29
Tortuosity	$t$ (-)	0.20	0.20	0.20	0.20	0.20	0.20
Geol. Unit >		Tptpul (tsw33)	Tptpmn (tsw34)	Tptpll (tsw35)	Tptpul (tsw33)	Tptpmn (tsw34)	Tptpll (tsw35)
FRACTURE DATA <sup>1</sup>							
Permeability	$k_f$ (m <sup>2</sup> )	7.80E-13	3.30E-13	9.10E-13	6.353E-13	1.00E-13	1.87E-12
Porosity	$f_f$ (-)	5.8E-3	8.5E-3	9.6E-3	0.171E-3	0.263E-3	0.329E-3
van Genuchten $\alpha$	$\alpha_f$ (1/Pa)	1.59E-3	1.04E-4	1.02E-4	1.57E-4	9.73E-5	1.66E-5
van Genuchten m (or $\lambda$ )	$m_f$ (-)	0.633	0.633	0.633	0.492	0.492	0.492
Residual saturation	$S_{lrf}$ (-)	0.01	0.01	0.01	0.01	0.01	0.01
Effective Tortuosity	$t$ (-)	0.0041 <sup>2</sup>	0.0060 <sup>2</sup>	0.0067 <sup>2</sup>	0.20 <sup>3</sup>	0.20 <sup>3</sup>	0.20 <sup>3</sup>
AFM coefficient	$\gamma$ (-)	0.60	0.57	0.57	N/A	N/A	N/A

### 3.3.9.5 Modeling results

Measurement of temperatures in the rock is the most reliable and extensive measurement in the DST. There are some 1750 sensors in 26 boreholes monitoring the temperatures and the readings are scanned and recorded once per hour. Temperature profiles along a borehole and temperature histories at a sensor are two typical ways of comparing predicted and measured temperatures to gain understanding of the heat-driven processes. Besides such qualitative assessment, a quantitative evaluation can be performed using statistical measures like the “root mean square difference” and the “mean difference” between modeled and measured values, as described in section 3.3.9.6 below.

Figure 3.3-9 shows the measured and simulated temperature profiles in boreholes 158, 159, and 160 at one year and four years after the start of heating. Measured and modeled temperature histories at sensors # 9, 17, 33, 44, and 55 are plotted in Figure 3.3-10.

The sensors in borehole 160 show a wide variety of temperature responses, depending on their location with respect to the heat sources (Figure 3.3-10). The three

sensors 160-9, 160-17 and 160-33 are all located directly above wing heater segments, and thus exhibit strong thermal perturbation. Both measured and simulated curves have short heat-pipe signals, indicating that rock water is boiled off within a short time period. At later heating stages, the measured temperatures run slightly higher than the simulated ones. Sensor 160-44 measures rock temperature close to the tip of the wing heater, a few meters further into the rock. The temperature increase is slower and a heat

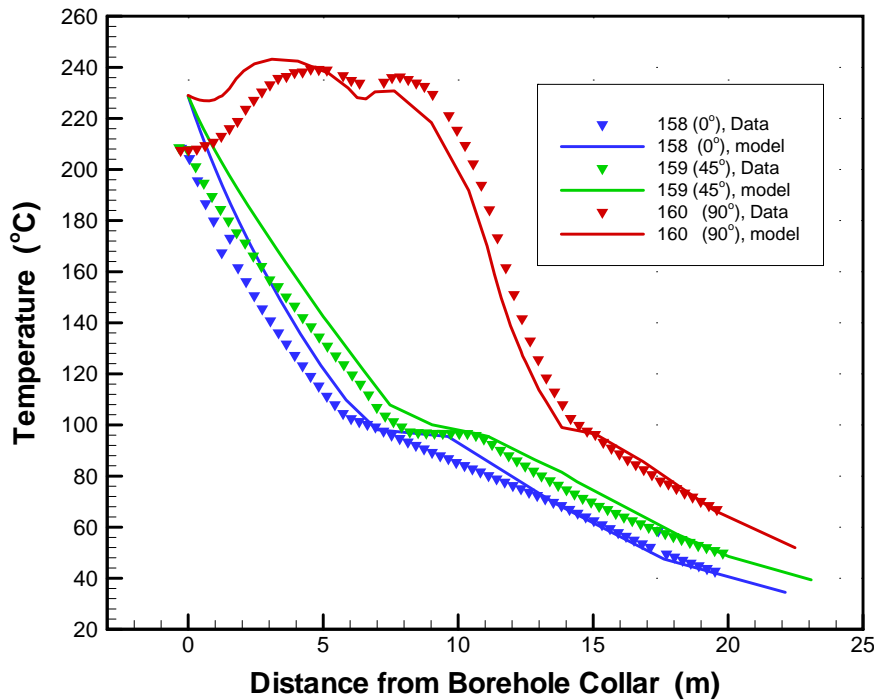
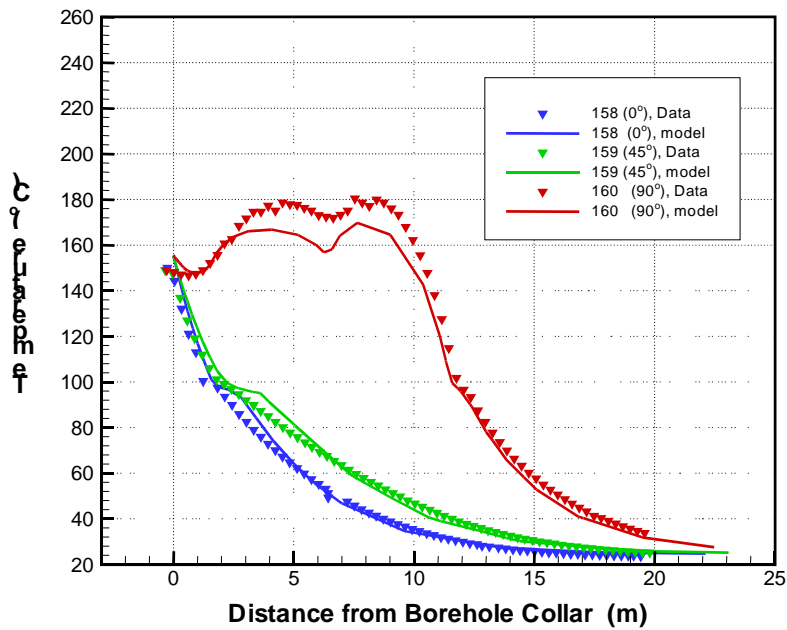


Figure 3.3-9. Measured and Simulated Temperature Profiles in Boreholes 158, 159, and 160 at (above) one year and (below) four years after the start of heating

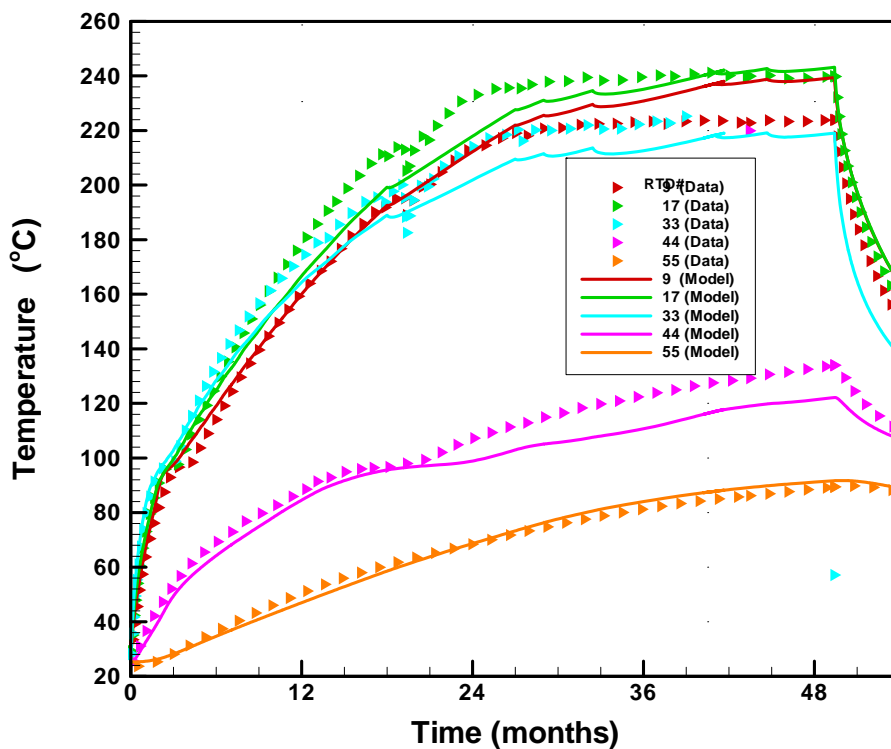


Figure 3.3-10. Temperature Histories at Selected Sensors in Borehole 160

pipe of significant duration evolves, beginning at about 15 months and lasting for 6 to 9 months. This indicates that the fractured rock at the location of this sensor remained in the two-phase boiling zone during this entire time period, and became dry afterwards as the boiling front eventually moved further away from the heater. While both curves exhibit the same starting point, the simulated temperature results show a slightly longer duration of the heat-pipe signal compared to the measured data. Finally, Sensor 160-55, with the largest distance into the rock, remains below boiling temperature for the entire heating phase. The measured and the simulated results match well for this sensor.

Figure 3.3-11 shows the simulated matrix saturations at one year and four years after the start of heating at a transverse section at  $Y = 6.4$  m containing the boreholes 47 through 51. The red, yellow, and greenish colors in Figures 3.3-11 and 3.3-12 indicate decrease of saturation or drying, with red representing a near-complete dry-out zone. The various shades of blue in these figures represent wetting or increase in saturation with deep blue representing substantial wetting. As can be seen in Figure 3.3-11, after one year the dry-out zone around the drift is substantial with more drying above the drift than below. The change in matrix saturation is a good indicator of drying as the pore water vaporizes and escapes into the fractures. Wetting on the other hand is not extensive yet, with little wetting above the drift. After four years of heating the dry-out zone around the drift expanded considerably with drying above and below the drift more or less similar. Wetting, however, is more pronounced below the drift than above. Figure 3.3-12 shows the simulated fracture saturations after one year and four years of heating at a transversal section at  $Y = 10.0$  m containing the boreholes 57 through 61. Vaporized water escaping into the fractures travels in all directions until it condenses and travel downward by gravity as indicated large increase in the fracture saturation below the drift at one year of drying. At four years of heating, the expanding dry-out zone has pushed the wetted area further down beyond the lower boundary of the figure.

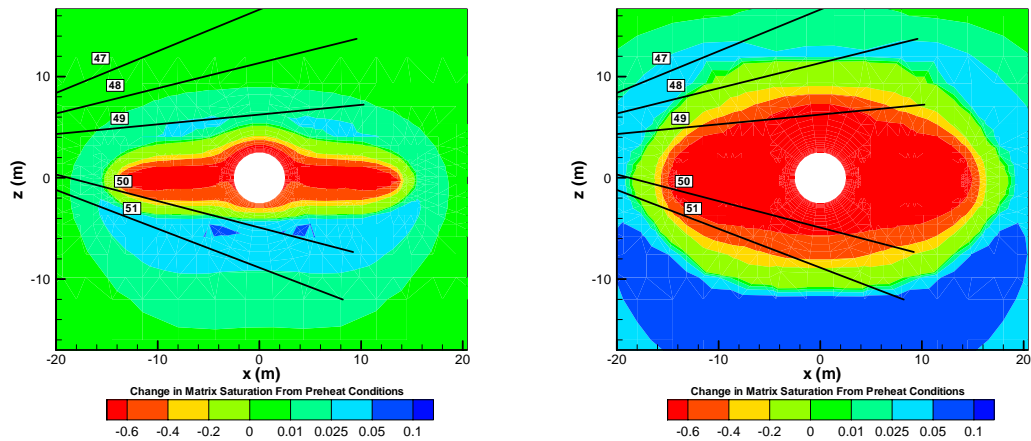


Figure 3.3-11. Simulated Matrix Saturation at XZ Section at  $Y = 6.4$  m after (left) One Year and (right) Four Years of Heating

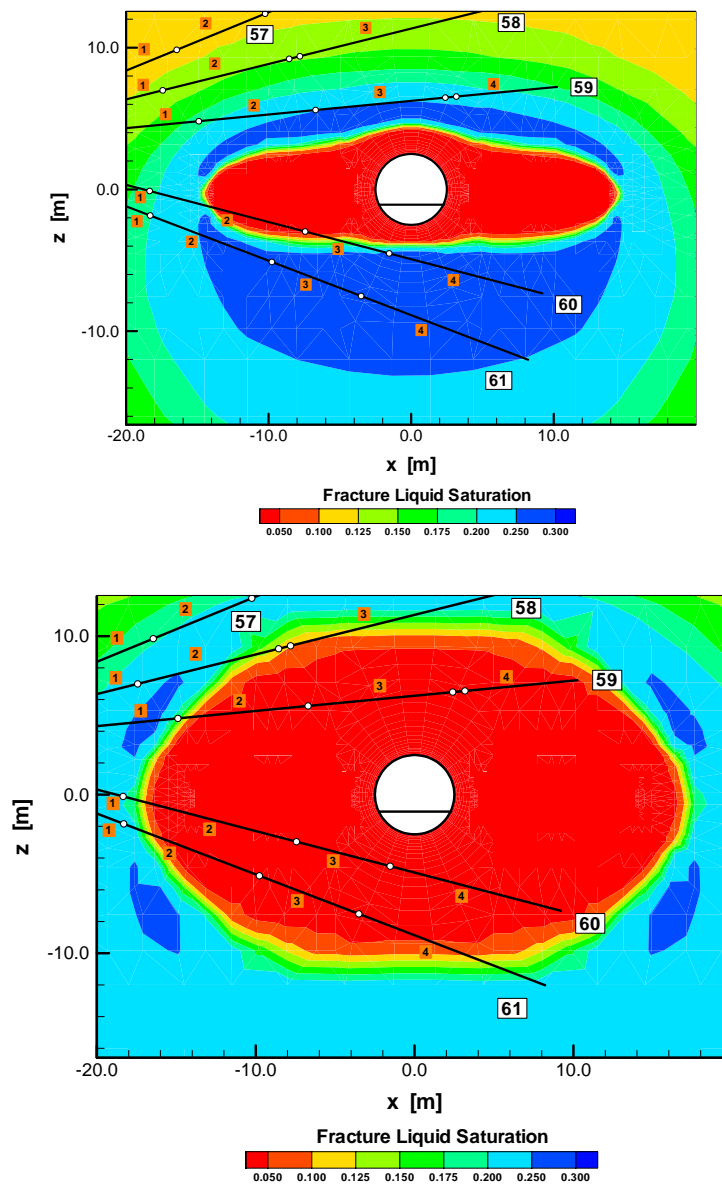


Figure 3.3-12. Simulated Fracture Saturation at XZ Section at  $Y = 10.0$  meters after (above) One Year and (below) Four Years of Heating

### 3.3.9.6 Statistical measures of temperature evaluation

In order to derive a “single number quantitative measure” to evaluate the goodness of fit between the simulated and measured temperatures standard statistical tools are modified to better adapt to the analyses of the DST data. The methodology and equations are as follows:

The two statistical measures employed are the mean difference and the root mean square difference. They are a function of simulated ( $T_{sim,i}$ ) and measured ( $T_{meas,i}$ ) temperatures. Simulated temperatures are spatially and temporally interpolated, as needed, to ensure proper correlation to the measured variables. Measured variables are directly taken from sensor readings. The statistical evaluation is conducted for specific times during the DST heating and cooling phase. Usually, all sensors are included in the evaluation; however, investigators can also decide to evaluate subsets of data, e.g., all sensors with temperatures above boiling (greater than 97°C), and all thermal sensors below boiling (less than 97°C).

For a given number of sensors  $N$ , the mean difference at a specified time is given as:

$$MD = \frac{\sum_{i=1}^N w_i (T_{sim,i} - T_{meas,i})}{\sum_{i=1}^N w_i} \quad (3.3-1)$$

A positive mean difference indicates an overestimate of the measured variable; that is, the simulation predicts more heat in the test block than measured. The opposite applies for a negative mean difference.

The root mean square difference for a specific time is described as:

$$RMSD = \left[ \frac{\sum_{i=1}^N w_i (T_{sim,i} - T_{meas,i})^2}{\sum_{i=1}^N w_i} \right]^{1/2} \quad (3.3-2)$$

The smaller the root mean square difference, the better the agreement between simulated and measured data. Thus, the root mean square difference reveals the accuracy of the simulation.

The weighting factors  $w_i$  in the above equations are introduced to give equal importance to all temperature subranges in the total range of temperatures observed. Weighting factors are based on a frequency analysis of the temperature measurements, acknowledging that the sensors are not uniformly distributed throughout the test block. The total range of temperature measurements is divided into 20 equally sized temperature subranges, and the number of measurements falling into each subrange was calculated. Then  $w_i$  is defined as the inverse of the number of data in each subrange  $i$  (exception: if this number is zero,  $w_i$  is zero). Basically, this weighing scheme gives equal weighting to (i.e., uses a mean temperature for) each temperature subrange.

Results of statistical analyses of measured and modeled temperatures in the DST are given in Table 3.3-4 for a number time points including the early part of the cooling phase.

Table 3.3-4. Statistical Comparison of Measured and Simulated Temperatures

Time (months)	Statistical Measure	
	Mean Difference (MD) (°C)	Root Mean Square Difference (RMSD) (°C)
6	0.01	5.63
12	-0.15	7.21
18	0.90	8.72
24	1.06	9.79
30	1.27	10.49
33	1.65	10.61
36	2.01	11.27
42	2.95	12.60
48	3.59	12.80
5 months cooling	4.34	8.12

## 4. Discussion and conclusions

The DECOVALEX III project was started in October 1999 when the heating phase of the DST was underway for nearly two years, having been initiated in December 1997. Before the start of heating, the DOE's research teams at the Lawrence Livermore National Laboratory (LLNL) and the Lawrence Berkeley National Laboratory (LBNL) performed pre-test predictive modeling of the thermal-hydrologic response of the DST using the NUFT and TOUGH codes respectively. These pre-test predictive modeling, and the ENRESA and NRC teams' modeling as DECOVALEX participants were documented in the DECOVALEX III Task 2A Interim Report (Revised) of February 2000.

The ongoing modeling and analyses of the DOE research team as the heating phase of the test progressed were limited to modeling by the TOUGH code only and involved a number of modifications and refinements to the TH model to study the DST. The ENRESA and NRC teams also refined and further developed their models and performed comparative analyses of their modeling results and actual measurements in the DST. This Task 2A Final report describes in a summary fashion the TH modeling of the DST performed by the research teams of ENRESA, NRC, and the DOE as part of the DECOVALEX III, Task 2A.

One of the three TH modeling of the DST in this report – that by the ENRESA research team described in Section 3.1 – is different from the other two in that the numerical code, CODE\_BRIGHT uses the finite element method while the other two codes, MULTIFLO and TOUGH are based on the finite difference method. This application of the finite element method by the ENRESA research team to simulate flow in unsaturated fractured rock represented by two co-located continua, one for the matrix and the other for the fractures, may be a first.

Based on the results of the modeling illustrated by the plots of temperature and moisture distributions and temperature histories in Sections 3.1, 3.2, and 3.3, it can be concluded that in general, the three models capture the TH response of the DST fairly well, although there are some differences between them. Conduction is the dominant heat-transfer mechanism in the fractured unsaturated rock in the DST, especially in the sub-boiling regime. However, the pore water plays an important role near the boiling point as it goes through cycles of vaporization and condensation causing the so called heat-pipe effect. A characteristic signature of heat-pipes – a short lull in the rise of temperature in the temperature plot – is captured by all three models as can be seen in Figure 3.1-22, 3.2-8, and 3.3-9.

The 2D modeling of the DST carried out by the ENRESA team initially was characterized by very little diffusion of vapor because the tortuosity factor was set at a low value of 0.05 and is referred to as the ND (No Diffusion) case. The recent 3D model with a tortuosity factor set at 1 and a vapor diffusion enhancement coefficient allows maximum vapor diffusion and is referred to as the MD (maximum diffusion) case. Comparative analyses of the modeling results for ND and MD cases lead to the conclusion that diffusion of vapor play an important role in flow and transport in the dry-out zone, since vapor mass fraction reaches its maximum in that region. Vapor flows by advection and by vapor diffusion/dispersion. Advection is very efficient in the high permeability fractured rock; however, diffusion is also a very efficient transport mechanism due to the high diffusivity of vapor in air.

The NRC research team examined two grid block size of 04 m and 5.0 m as well as two infiltration rates and the dual permeability model (DKM) with and without the active fracture model (AFM). An increase in model block size allowed relatively large

infiltration rates (3.0 mm/yr) while maintaining a moderate ambient matrix saturation of 0.90. There was significant difference in the predicted matrix saturations between the small block model and the large block model as indicated by the larger dry-out zone in the small block model especially at four years after the start of heating.

The sensors in borehole 160, located between two wing heaters, display a wide variety of responses depending on their location with respect to the heaters. The ones located directly above the wing heaters exhibit strong thermal perturbation. Both measured and simulated temperature plots have relatively short heat-pipe signals suggesting that pore water is boiled off in a relatively short time period because of close proximity to the heaters.

[www.ski.se](http://www.ski.se)

**STATENS KÄRNKRAFTINSPEKTION**  
Swedish Nuclear Power Inspectorate

**POST/POSTAL ADDRESS** SE-106 58 Stockholm

**BESÖK/OFFICE** Klarabergsviadukten 90

**TELEFON/TELEPHONE** +46 (0)8 698 84 00

**TELEFAX** +46 (0)8 661 90 86

**E-POST/E-MAIL** [ski@ski.se](mailto:ski@ski.se)

**WEBBPLATS/WEB SITE** [www.ski.se](http://www.ski.se)